University of South Carolina
Scholar Commons

Theses and Dissertations

8-9-2014

APPLICATIONS OF ELECTROMAGNETIC PRINCIPLES IN THE DESIGN AND DEVELOPMENT OF PROXIMITY WIRELESS SENSORS

Md Nazmul Alam
University of South Carolina - Columbia

Follow this and additional works at: http://scholarcommons.sc.edu/etd

Recommended Citation
Alam, M.(2014). *APPLICATIONS OF ELECTROMAGNETIC PRINCIPLES IN THE DESIGN AND DEVELOPMENT OF PROXIMITY WIRELESS SENSORS.* (Doctoral dissertation). Retrieved from http://scholarcommons.sc.edu/etd/2784

This Open Access Dissertation is brought to you for free and open access by Scholar Commons. It has been accepted for inclusion in Theses and Dissertations by an authorized administrator of Scholar Commons. For more information, please contact SCHOLARC@mailbox.sc.edu.

APPLICATIONS OF ELECTROMAGNETIC PRINCIPLES IN THE DESIGN AND DEVELOPMENT OF PROXIMITY WIRELESS SENSORS

by

Md Nazmul Alam

Bachelor of Science
Bangladesh University of Engineering and Technology, 2006

Master of Science
Bangladesh University of Engineering and Technology, 2008

Submitted in Partial Fulfillment of the Requirements

For the Degree of Doctor of Philosophy in

Electrical Engineering

College of Engineering and Computing

University of South Carolina

2014

Accepted by:

Mohammod Ali, Major Professor

Roger A. Dougal, Committee Member

Yong-June Shin, Committee Member

Bin Zhang, Committee Member

Jamil Khan, Committee Member

Lacy Ford, Vice Provost and Dean of Graduate Studies

© Copyright by Md. Nazmul Alam, 2014
All Rights Reserved.

DEDICATION

To my endless source of inspiration

My parents Nur-Jahan Alam & Md Shamsul Alam

&

My wife Fahmida Islam Tamanna

ACKNOWLEDGEMENTS

In the name of Allah, most gracious, most merciful. First and foremost, I would like to express my sincere gratitude towards Almighty Allah (swt) for nourishing me up to this level, guiding me through inevitably difficult times, and helping me to pursue my dream of completing my PhD.

Next, I want to thank my advisor, supervisor and mentor Dr. Mohammod Ali for expertly navigating me in the process of my PhD literature review, research, experiments, proposal and dissertation, without whom all things would have descended into chaos. His incredible ability to foresee future areas of difficulty in potential research, his persistent guidance, and his endless patience, resulted in my PhD dissertation and the finished dissertations of many other students as well. His thorough attention to my academic and personal requests has been highly appreciated. I thank him again for his tireless guidance and support all these years.

I would like to thank Dr. Roger Dougal, Dr. Yong-June Shin, Dr. Bin Zhang and Dr. Jamil Khan for serving on my proposal and PhD committees. Their suggestions, comments, and valuable time are highly appreciated. In particular, I would like to acknowledge the brilliant mind of Dr. Dougal for his expansive scientific expertise and invaluable feedback in the development of my research.

I would like to offer special thank Dr. Rashed Bhuiyan and David Coats for their diligence in setting up tests, taking measurements, providing a lot of technical feedback

and especially bringing the joy of conducting research together. I am also very thankful to my colleagues in the Microwave Engineering Lab particularly Dr. Md Rashidul Islam and Nowrin Hasan Chamok. I would like to thank David Metts and other members of Department of Electrical Engineering for their helping attitude. Also, I would like to acknowledge my fellow friends in Columbia, South Carolina for their countless favors.

Last, but not least, my deepest gratitude is extended to my loving and loyal family, particularly my parents, my brothers and my extraordinary wife. My parents are my inside source of my inspiration. Their love, sacrifice, patience and teaching helped me to shape my moral and education background into what they are today. I am also deeply grateful to my wife; her unwavering commitment, continuous encouragement and moral support for all these days and many days to come.

Nazmul Alam

The University of South Carolina

May 2014

ABSTRACT

Sensors and sensing system are playing dominant roles in monitoring the health of infrastructure, such as bridges, power lines, gas pipelines, rail roads etc. Sensing modalities employing Surface Acoustic Waves (SAW), Electromagnetic (EM) and optical have been investigated and reported. Sensors that utilize the perturbation of EM fields as function of the change in the physical structural or material phenomenon are of particular interest because of their inherent synergy with electronic system and diagnostic techniques, e.g. Time Domain Reflectometry (TDR), Joint-Time-Frequency-Domain-Reflectometry (JTFDR). The focus of this work is to study and develop new sensing and monitoring concepts that are based on EM principles.

First, the analyses, design and development of a static electric field type sensor are presented for application in embedded concrete moisture content measurement. The analytical formulation and results based on conformal mapping method for an interdigitated sensor clearly show the dependency of the field penetration depth and the inter-electrode capacitance on the electrode sizes and their spacings. It is observed that larger electrode size and small separation are needed in order to achieve substantially higher capacitance or large field penetration depth. A meander and a circular sensor are fabricated and tested to demonstrate concrete moisture content measurements that show that moisture content is a linear function of sensor interelectrode capacitance. Second, sub-wavelength dimension non-intrusive wave launchers are designed and tested that can

launch TDR or JTFDR type broadband surface wave waveforms in the VHF-UHF bands in order to detect cable faults. Greater than 3:1 transmission bandwidth (100-300 MHz) is obtained with a cylindrical launcher on square orthogonal ground plane while with a CSW launcher more than an octave (100-240 MHz) bandwidth is achieved. Open circuit faults are detected using surface waves and TDR on two XLPE cables. Third, a new mathematical method is developed that can be used to determine the changes in the dielectric constant of a cable insulating material. By comparing the experimental JTFDR waveform signatures from a new and an aged cable, it is demonstrated that the change in the average dielectric constant of the insulation material can be estimated from the phase transfer functions obtained from the FFT of measured magnitude and phase responses. The experimental data obtained for two types of cables, XLPE and EPR show that the dielectric constant decreases with accelerated aging. Finally, JTFDR surface wave sensing method is developed and applied to determine the locations of aging related insulation damage in power cables. The comparative power spectral responses of conducted and non-intrusive surface wave JTFDR waveforms clearly show the resulting bandwidth reduction in the latter primarily because of the reflective nature of the coupling. It is demonstrated that with the help of a non-intrusive wave launcher and a 120 MHz Gaussian chirp waveform the location of aging related insulation damages can be detected. Experiments conducted show the cross-correlation peaks at subsequent aging intervals as the cable is aged inside a heat chamber.

TABLE OF CONTENTS

DEDICATION iii

ACKNOWLEDGEMENTS iv

ABSTRACT vi

LIST OF TABLES xi

LIST OF FIGURES xii

LIST OF ABBREVIATIONS xvii

CHAPTER 1 INTRODUCTION 1

1.1 Motivation and Objectives 1

1.2 Organization 6

CHAPTER 2 STATIC FIELD SENSING-INTERDIGITATED CAPACITOR FUNDAMENTALS 8

2.1 Proximity Interdigitated Capacitor 9

2.2 Analytical Solution of a Unit Interdigitated Cell 10

CHAPTER 3 STATIC FIELD SENSING- MOISTURE SENSING IN CONCRETE USING INTERDIGITATED SENSORS 26

3.1 Sensor Geometry and Design Details 27

3.2 Experimental Setup 28

3.3 Results 32

CHAPTER 4 PROPAGATING WAVE SENSING- THE THEORY OF SURFACE WAVE PROPAGATION 37

4.1 Sommerfeld's work 38

4.2 Georg Goubau's Work 40

4.3 Elmore's Work 42

CHAPTER 5 DESIGN AND APPLICATION OF SURFACE WAVE LAUNCHERS FOR NON-INTRUSIVE POWER LINE FAULT SENSING.....45

5.1 Surface Wave Launchers and Their Transmission Properties.....48

5.2 TDR Experiments Using CSW Launcher and VNA 60

5.3 Circuit Experiment CSW Launchers.....63

5.4 Surface Wave Propagation Velocity Measurements in Unshielded XLPE Power Cables.....67

CHAPTER 6 A NEW METHOD TO ESTIMATE THE AVERAGE DIELECTRIC CONSTANTS OF AGED POWER CABLES.....72

6.1 Mathematical Formulation to Estimate the Dielectric Constant of an Aged Cable 75

6.2 Experimental Methodology.....82

6.3 Proposed Analysis and Results 84

CHAPTER 7 NON-INTRUSIVE ACCELERATED AGING EXPERIMENTS WITH SURFACE WAVE LAUNCHERS.....92

7.1 Experimental Setup for JTFDR with Wide Monopole Launchers.....93

7.2 Reflectometry Comparison: Direct and Non-intrusive Measurements.....96

7.3 Accelerated Aging Tests Results.....99

CHAPTER 8 CONCLUSION AND FUTURE WORKS.....106

8.1 Contributions.....106

8.2 Future Works.....109

BIBLIOGRAPHY 112

LIST OF TABLES

Table 2.1. Comparison between analytical solution and simulation results from Ansys Maxwell 2D for different w/a 24

Table 5.1. Location of open circuit measured using VNA and CSW launcher 62

Table 5.2. Location of open circuit measured using circuit and CSW launcher 66

Table 5.3. Measured velocity of surface wave 70

Table 6.1. Comparison of relative permittivity.....88

LIST OF FIGURES

Figure 1.1. Some sensor use in civil infrastructure health monitoring. 1

Figure 1.2. Sensors and sensing system (bridge image from google images); a sensor node [4]. 2

Figure 1.3. Rogowski coil sensor used for unshielded cable partial discharge detection [19] 5

Figure 1.4. Direct contact accelerated aging related fault detection system using JTFDR 5

Figure 1.5. Broadband antenna used for high frequency PD detection. 6

Figure 2.1. Sensor system a system level diagram. 8

Figure 2.2. (a) Conventional parallel plate capacitor (b) proximity interdigitated capacitor [44]. 10

Figure 2.3. The electric flux distribution for a unit interdigitated cell. 11

Figure 2.4. Plot of the general inverse-cosine transformation $u' + jv' = \cos - 1(x' + jy')$ [43]. 12

Figure 2.5. Fields between co-planar metal planes with a finite gap [43]. 14

Figure 2.6. Field penetration depth, T mm versus electrode width w mm and the distance between the two electrodes, a mm. 17

Figure 2.7. Field penetration depth, T mm versus electrode width w mm for a=0.05 mm, 0.1 mm, 0.2 mm, 0.5mm, 1mm and 5 mm. 18

Figure 2.8. Electrode width, w mm versus field penetration depth T mm for, a=0.05 mm, a=0.1 mm, a=0.2 mm, a=0.5 mm, a=1 mm and a=5 mm. 19

Figure 2.9. $\frac{C\epsilon_r\epsilon_0}{l}$ versus the electrode width w and the distance between two electrodes a. 21

Figure 2.10. $\frac{C\epsilon_r\epsilon_0}{l}$ versus the electrode width w and the distance between two electrodes a. 22

Figure 2.11. Plot of vector electric field in Ansys Maxwell 2D for W=10 mm and a=10mm. 22

Figure 3.1. The typical geometry of an interdigitated sensor. 28

Figure 3.2. (a) Block diagram of sensor circuit and its (b) equivalent circuit. 28

Figure 3.3. (a) Experimental setup to measure $C_{DS}$for concrete samples, (b) placement of the sensor in the samples....31

Figure 3.4. Ansoft Maxwell 3D model of full circular sensor. 32

Figure 3.5. Measured capacitance, C_{DS} versus moisture content, M_V for (a) the meander sensor and (b) the full circular sensor. 34

Figure 3.6. Comparison between the measured, analytical and simulated data for the meander sensor. 35

Figure 3.7. Comparison of measured and simulated capacitance for the full circular sensor. 35

Figure 4.1. Graphical representation of Sommerfeld's wire/line with finite conductivity 39

Figure 4.2. Graphical representation of a Goubau wire/line....41

Figure 4.3. Launching surface waves on a direct connected wire and receiving them using horn antennas [41]. 41

Figure 4.4. Glenn Elmore TM wave surface wave simulation model [65]....42

Figure 4.5. Elmore designed slotted horn antenna directly connected with a bare aluminum power line cable reported in [65] 43

Figure 4.6. Elmore measurement results of GAmax and transmission performance S_{21} on a 18 m long and 4 mm diameter copper power line conductor [65]. 44

Figure 5.1. Examples of unshielded cables. Proposed non-intrusive wireless sensor block diagram. Schematic representation of sensor placement on cables 46

Figure 5.2. Experimental setup of monopole surface wave launchers on XLPE cable; cable length=2.14m. 49

Figure 5.3. Measured S_{11} vs frequency of wire and wide monopole launchers in the presence and absence of a 2.14 m long XLPE unshielded power cable 50

Figure 5.4. Measured transmission between monopoles with and without cable. 51

Figure 5.5. Transmission response of the wide monopoles. 52

Figure 5.6. HFSS model to simulate electric and magnetic fields. 53

Figure 5.7. Comparison of simulated surface currents between the wire and wide monopoles in the presence of the XLPE cable. 53

Figure 5.8. Computed H-field distribution along the cable (a) XZ plane and (b) YZ plane. 54

Figure 5.9. Electric field (E) distribution in (a) XZ, and (b) YZ plane 55

Figure 5.10. Proposed conformal surface wave launcher; (a) 3D view and bottom view, (b) installed on an unshielded power cable. The total ground plane dimension is 300 mm by 150 mm 56

Figure 5.11. Transmission performance comparison for a pair of CSW launchers, wire monopole launchers and wide monopole launchers when placed on an XLPE cable of length 2.14 m. 56

Figure 5.12. Transmission between a pair CSW launchers when placed against an XLPE power cable. 59

Figure 5.13. Effect of ground height on the transmission between a pair of CSW launchers [79]. 60

Figure 5.14. Effect of ground plane size on transmission for CSW launchers [79]. 61

Figure 5.15. Results of TDR experiments using a single CSW launcher against four XLPE cables open circuited at the end [79]. 62

Figure 5.16. The comparison of the generated pulse with a Gaussian pulse. 64

Figure 5.17. Schematic diagram of the experimental set-up to perform TDR open circuit fault detection in XLPE cables using the pulse generator circuit and the CSW launcher. 64

Figure 5.18. Normalized amplitude of the return signal for XLPE cable lengths

of (a) 4.26 m (b) 9.45 m. Experimental results corresponding to the setup shown in Fig. 5.18. 66

Figure 5.19. Experimental setup to determine the surface wave propagation velocity in an unshielded XLPE cable. 69

Figure 5.20. Return signal observed in the oscilloscope for different XLPE able. lengths and different pulse widths 69

Figure 6.1. Experimental setup and definitions of terms. 75

Figure 6.2. The experimental setup used in the accelerated aging tests reported in [10]. 82

Figure 6.3 (a). Total signal (V_{RT}) observed at oscilloscope. 6.3(b) Truncated signal corresponding to injected signal (V_3^+) using rectangular time window at t_1. 6.3(c) Truncated signal corresponding to reflected signal from the end (V_3^-) using rectangular time window at t_2. 85

Figure 6.4. Experimental phase plot with least square error fitted phase plot. 86

Figure 6.5. Average dielectric constant, ε_{r1} determined using the proposed method for XLPE insulated aged cable section. XLPE insulation with aged section length = 1 m. 87

Figure 6.6. Average dielectric constant, ε_{r1} determined using the proposed method for EPR insulated cable section. EPR insulation with aged section = 1 m. 87

Figure 6.7. The experimental setup used for artificial water intrusion in XLPE cable. The wedged section is 2.5 cm long. 88

Figure 6.8 (a). Total waveform (V_{RT}) of the cable under test before water is introduced in the wedge (b) Total waveform (V_{RT}) of the cable under test after water is introduced in the wedge. 89

Figure 7.1. Non-intrusive accelerated aging test system functional diagram. 94

Figure 7.2. Photograph of non-intrusive accelerated aging test. 94

Figure 7.3. Direct contact method of JTFDR fault detection. Coaxial 10 m long shielded XLPE power cable; 100 MHz center frequency of input waveform a) Input signal b) Output signal c) corresponding time-frequency cross-correlated signal. 96

Figure 7.4. Power spectra comparison between input and reflected signal of Fig. 7.3. 97

Figure 7.5. Non-Intrusive JTFDR waveforms for a 22.4 ft (6.83 m) unshielded XLPE insulated power cable along with 3.5ft coaxial instrumental cable using120 MHz JTFDR signal a) Input signal, b) reflected signal, and c) corresponding time-frequency cross-correlated signal.....98

Figure 7.6. Power spectra comparison between the input and reflected signals of Fig. 7.5. 98

Figure 7.7. a) The first reference input signal generated from AWG ($f_r = 120\ MHz, BW = 100MHz, t_D = 30\ ns$). b) Return reflected signals for the unshielded cable at different aging periods.....100

Figure 7.8. Cross correlations at different aging periods for the first reference signal ($f_r = 120\ MHz, BW = 100MHz, t_D = 30\ ns$). 101

Figure 7.9. a) The second reference input signal generated from AWG ($f_r = 150\ MHz, BW = 100MHz, t_D = 30\ ns$). b) Return reflected signals for the unshielded cable at different aging periods. 102

Figure 7.10. Cross correlations at different aging periods for second reference signal ($f_r = 150\ MHz, BW = 100MHz, t_D = 30\ ns$). 104

LIST OF ABBREVIATIONS

BTS .....Bureau of Transportation Statistics

CSW.....Conformal Surface Wave

DOE .....Department of Energy

FDR.....Frequency Domain Reflectometry

GPR.....Ground Penetrating Radar

JTFDR.....Joint Time Frequency Domain Reflectometry

SAIDI.....System Average Interruption Duration Index

SAIFI..... System Average Interruption Frequency Index

TDR..... Time Domain Reflectometry

CHAPTER 1

INTRODUCTION

1.1 MOTIVATION AND OBJECTIVES

Sensors and sensing system are playing a dominant role in monitoring the health of infrastructure, such as bridges, pipelines, rail roads, and power lines. Wireless embedded sensors and sensing system present a unique opportunity because by embedding such sensors at critical locations of an infrastructure vital information can be obtained in real-time allowing rapid low cost monitoring and diagnostics. In recent years, researchers have studied various different kinds of sensors e.g. crack, moisture, strain, pH, accelerometer etc. for structural health monitoring [1-13]. Various structural health monitoring sensors are shown in Fig. 1.1.

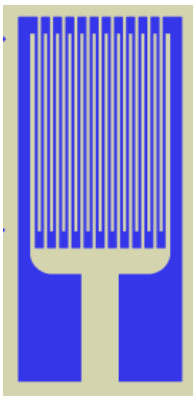

(a) Strain sensor [1]

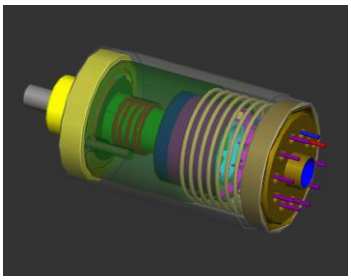

(b) Acceleration sensor [2]

(c) Moisture sensor [3]

Figure 1.1.Typical sensors used in civil infrastructure health monitoring.

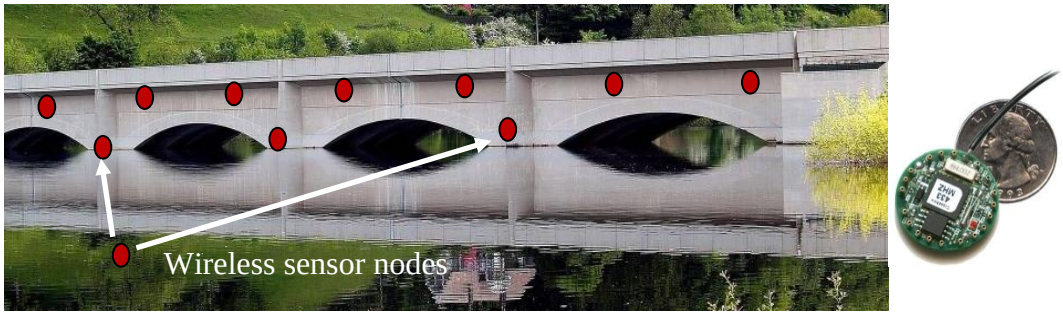

Figure 1.2. Sensors and sensing system (bridge image from google images); a sensor node [4].

Another critical infrastructure, where wireless sensors can play a vital role, is the electrical power grid. In many cases, power cables suffer premature failures due to various kinds of local stresses, including electrical, thermal, mechanical, chemical etc. Researchers are working on wireless sensors to monitor faults and continuous condition assessment of cables at different states, such as, open circuit, short circuit, partial discharge (PD), insulation damage, water and electrical tree formation in the insulation and high impedance fault [14-21].

Sensing modalities employing Surface Acoustic Waves (SAW), Electromagnetic (EM) and optical have been investigated and reported [22-23].

Sensors that utilize the perturbation of EM fields as function of the change in the physical structural or material phenomenon are of particular interest because of their inherent synergy with electronic system and diagnostic techniques, e.g. Time Domain Reflectometry (TDR), Joint-Time-Frequency-Domain-Reflectometry (JTFDR).

One particular application area that can benefit tremendously from an innovative EM sensor is an embeddable wireless moisture sensor for structural health monitoring. Since dielectric permittivity of a material is a strong function of moisture (water has a

relative permittivity of 80 compared to dry concrete which is 4 at 100 kHz) it can be measured using a capacitive sensor. Increasing moisture will increase the sensor capacitance and hence the sensor output voltage. Moisture is unavoidable in structures yet they pose a serious problem resulting in crack in the concrete and corrosion in steel reinforcement. Since visual inspection is not possible embedded wireless moisture sensors will be greatly preferred. A simple two electrode capacitive sensor (typically used for soil moisture measurement in agricultural land) is too invasive and large [24]. Instead, a planar conformal sensor that is constructed of interdigitated electrodes will be a preferred choice because of its ease of integration with other electronics on a miniature circuit board. Various interdigitated sensors have been proposed for gas detection, resin curing, air humidity sensing and food moisture measurement [25-29]. However, the fundamental knowledge base that is required to design a miniature, conformal interdigitated sensor for embedded concrete moisture sensing is lacking. This includes an in-depth understanding of the design space that defines electric field penetration depth and its equivalent interelectrode capacitance as function of sensor geometrical parameters. 2D FEM simulation of such sensors to validate findings from static analytical solutions are also needed. Finally, sensors need to be designed, built and tested to validate that they meet those characteristics predicted by the analyses and modeling. **Thus, the first major focus of this dissertation is the development of the foundations for static EM field sensing for moisture content measurement in materials.**

Another specific application that will greatly benefit from innovative EM sensors is power system fault or incipient fault monitoring e.g. open circuit, short circuit, insulation damage etc. For example, consider the Rogowski coil sensor shown in Fig. 1.3.

on a power line to detect the emitted pulses from partial discharge [19]. One has to have some knowledge of where such PD will occur otherwise the coil will not be useful because of its location specific detection capacity. Moreover, because of its very low frequency operation high frequency emissions will not be detected. Researchers have used TDR, FDR and JTFDR for cable health monitoring including open circuit, short circuit, PD and insulation damage detection [30-37]. In a vast majority of the cases, the focus has been on conducted direct-contact measurements (see Fig. 1.4). Other researchers have used broadband antennas to detect PD pulses from cables and substations (see Fig. 1.5) [14, 38]. In this work, we consider EM antennas in conjunction with TDR and JTFDR methods to detect cable faults and insulation damage. While ordinarily an antenna is used in free space for communication applications the focus of this work is on using antennas as transducers that can inject a propagating surface wave at the conductor dielectric interface of a cable. Unlike earlier works of surface waves for communication and radar [39-42] our proposed approach considers non-intrusive subwavelength launchers and use the reflected wave signature to detect the location of the fault. Similarly as before, the fundamental know-how of propagating surface wave sensing for cable health monitoring needs to be developed. This includes investigating the feasibility of such an approach e.g. sensor size, type, signal frequency, bandwidth, transmission loss, range and the basic capacity to detect fault. This also includes the feasibility of non-intrusive cable insulation damage detection and estimating the changes in the average dielectric constant of the insulation material as function of cable aging. **Thus, the second major thrust of this dissertation is the development of the methodology for propagating EM wave sensing for cable health monitoring.**

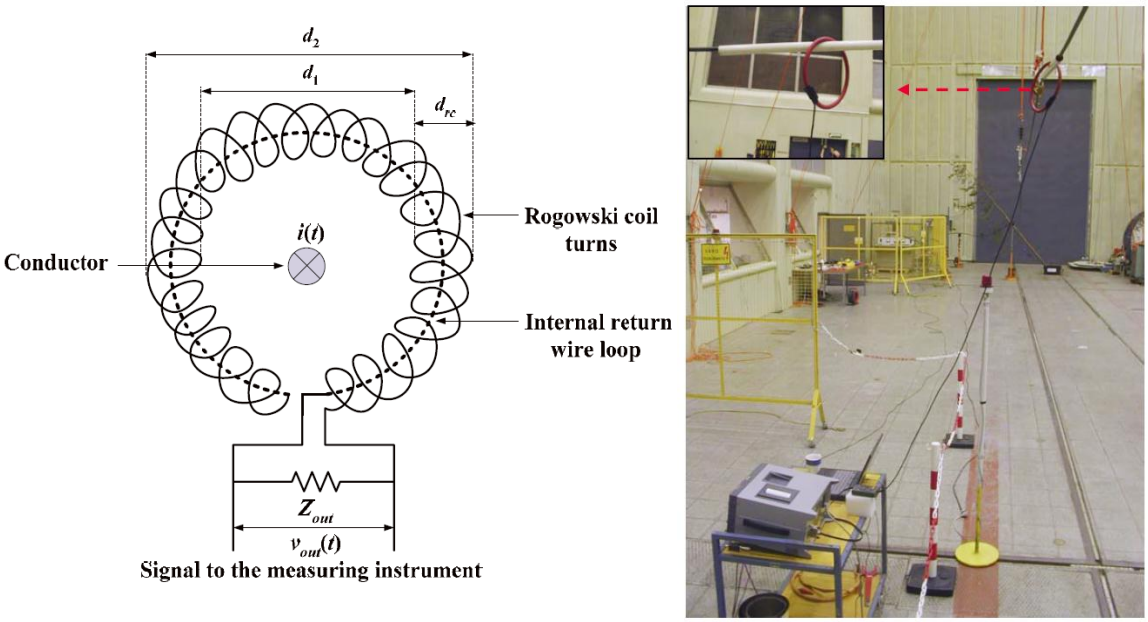

Figure 1.3. Rogowski coil sensor used for unshielded cable partial discharge detection [19].

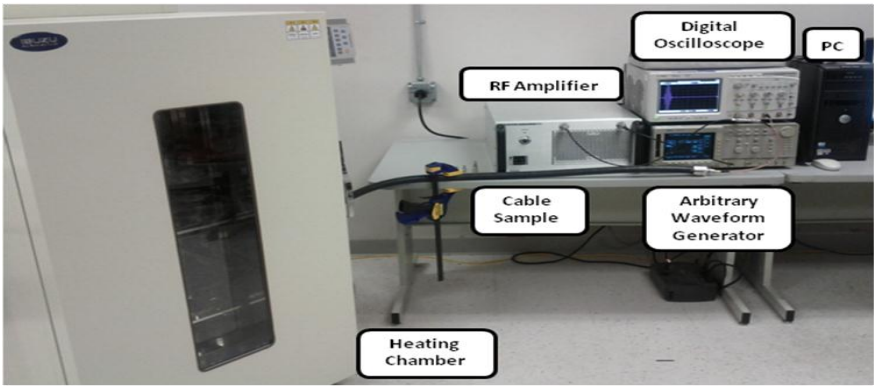

Figure 1.4. Direct contact accelerated aging related fault detection system using JTFDR [36].

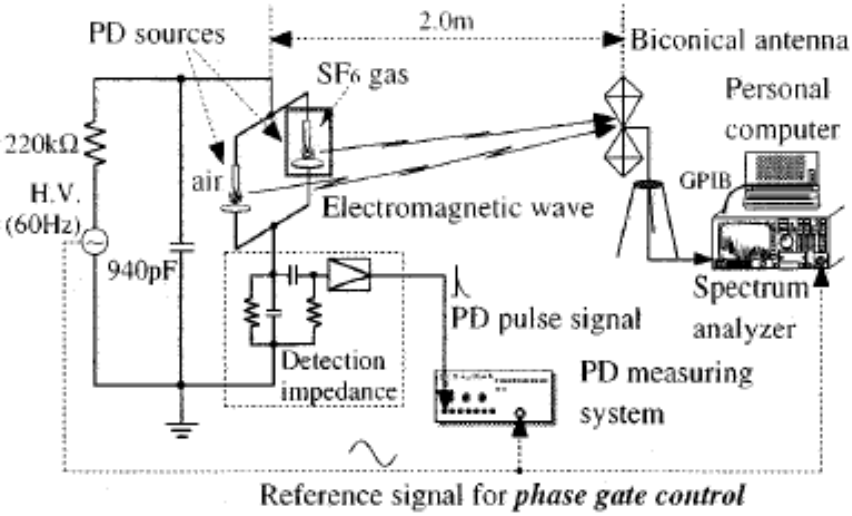

Figure 1.5. Broadband antenna used for high frequency PD detection [14].

1.2 ORGANIZATION

In Chapter 2 the fundaments of static field sensing is formulated and then a unit interdigitated cell is characterized analytically using conformal mapping method. Analytical results of interelectrode capacitance are compared with results obtained from Ansys Maxwell 2D simulation for different sensor parameters.

In Chapter 3 to investigate the efficacy of the static electric field type sensing using interdigitated sensors the design, fabrication and experimental testing methods and the experimental results of a meander and a circular sensor are presented. Measurement results are compared with results obtained from Ansys Maxwell 3D static field simulator.

In Chapter 4 a concise review of surface wave propagation principles is presented followed by a brief literature review of surface wave launcher design and application.

In Chapter 5 the concept of surface wave launch and propagation as a non-contact sensing tool is demonstrated for open circuit fault detection in unshielded cables. Different laboratory prototypes are fabricated and measured to understand their frequency dependent return loss and transmission performance characteristics. Finally, a pulse generator circuit is designed and built to excite a nano-second TDR pulse using a Conformal Surface Wave (CSW) exciter to detect open circuit fault in cables.

In Chapter 6 a new mathematical method is presented to estimate the change in the average dielectric constant of aged power cables from JTFDR measurements from accelerated aging test based on the modified Arrhenius equation.

In Chapter 7 the application of surface wave sensing with JTFDR is demonstrated for accelerated thermal aging related insulation damage detection for unshielded XLPE cables.

Chapter 8 summarizes the contributions of this dissertation and suggests some possible future works.

CHAPTER 2

STATIC FIELD SENSING-INTERDIGITATED CAPACITOR FUNDAMENTALS

Measuring the moisture content in a material such as concrete using capacitive sensors is a very attractive solution. Interdigitated sensors are particularly interesting because of their planar conformal geometry, ease of fabrication and integration with circuit components. A system level diagram is shown in Fig. 2.1 which shows that measured output voltage being proportional to moisture in the Material Under Test (MUT) reflects the variation in the moisture. A microcontroller controls the measurement frequency and the measured output is wirelessly sent to a host station.

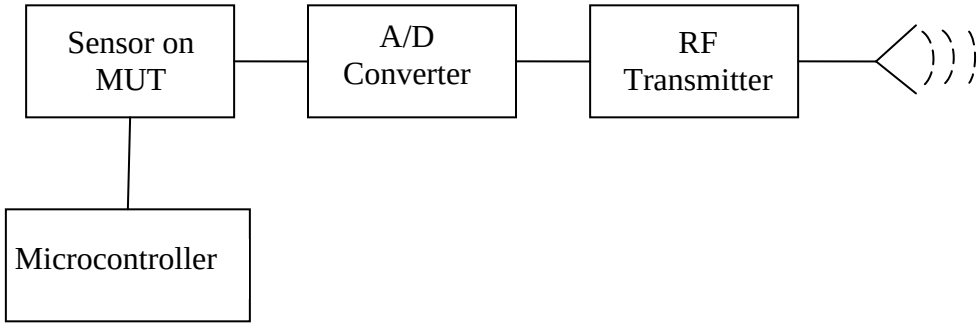

Figure 2.1. Sensor system a system level diagram.

In order to design proximity interdigitated sensors, their fundamental characteristics such as field penetration depth and capacitance are studied using conformal mapping method. For comparison, 2-D FEM (Finite Element Method) simulations of a simple geometry are also performed.

2.1 PROXIMITY INTERDIGITATED CAPACITOR

A regular capacitor consists of two electrical parallel plates separated by a dielectric material (solid, liquid or gas) (Fig. 2.2 (a)). The capacitance (C) is described as the relation between the charge distribution (Q) and the difference in the voltage (V); that is

$$C = \frac{Q}{V} \tag{2.1}$$

The capacitance also depends on the geometrical shape of the conductor-dielectric arrangement and position. From Fig. 2.2 (a), the measured capacitance related to the dielectric constant of the material is

$$C = \frac{\epsilon_o \epsilon_r A}{d} \tag{2.2}$$

where A is area of the plate and d is the separation between the two electrodes. Capacitive sensors can be of different shapes. One of the popular shapes is a co-planar structure which is also known as an interdigitated structure. Fig. 2.2 (b) illustrates the physical structure and field lines of an interdigitated capacitive sensor. Because of its planar structure, it is suitable for mounting on most dielectric surfaces. The fringing electric fields of the planar electrodes bend and penetrate into the material which is attached to the sensor. Thus, the variation of the dielectric property of the attached material affects the interelectrode capacitance.

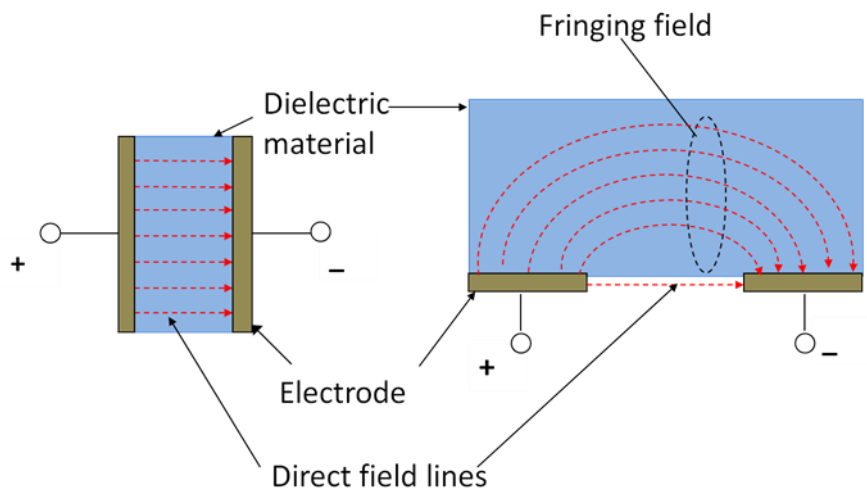

Figure 2.2. (a) Conventional parallel plate capacitor (b) proximity interdigitated capacitor [44].

2.2 ANALYTICAL SOLUTION OF A UNIT INTERDIGITATED CELL

The geometry of the unit cell of an interdigitated sensor is shown in Fig. 2.3. The unit cell consists of a dielectric substrate with thickness h_s and dielectric constant ε_{r1}. There are two conducting electrodes named the driving electrode and the sensing electrode each at a potential of V_0 and 0 volt, respectively. The width of each electrode is w and their separation distance is a. The conducting electrodes are each h_e thick. In general this thickness is very small and thus $h_e << h_s$. The sensor unit cell is immersed in a dielectric medium where it creates electric flux lines as illustrated in Fig. 2.3.

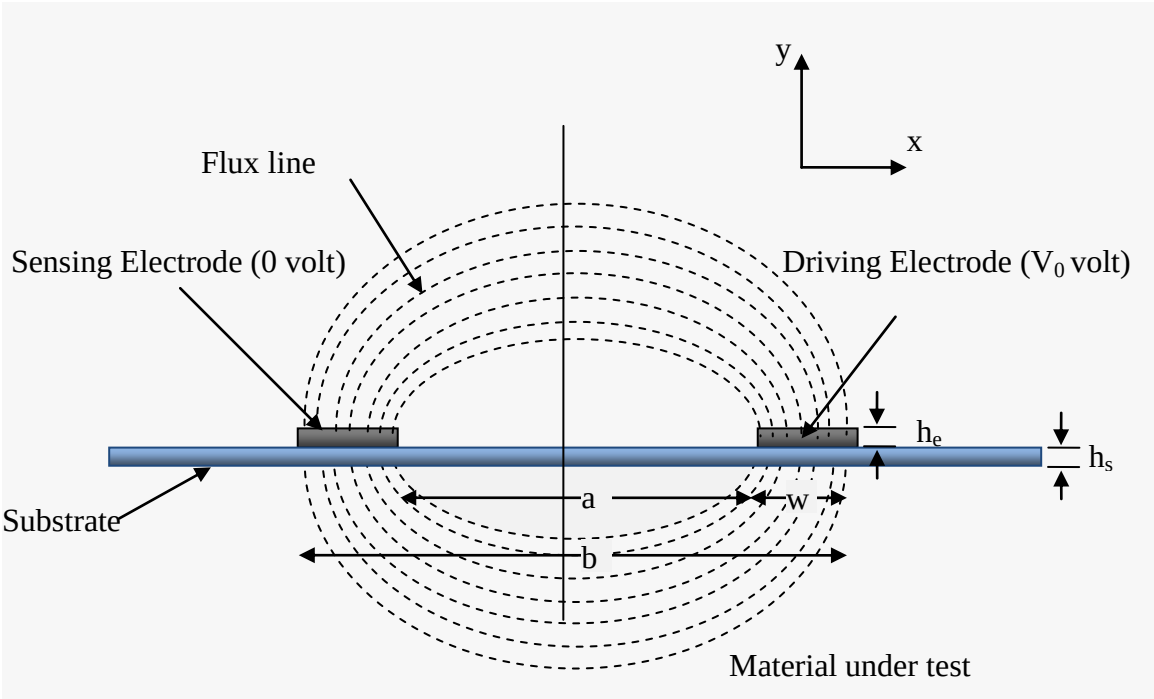

Figure 2.3. The electric flux distribution for a unit interdigitated cell.

For simplicity of analysis, we did not consider the presence of a guard electrode. However, a guard electrode can be added and would be at ground potential. The guard electrode does not contribute in sensing but it provides immunity to the sensor from undesired Electromagnetic Interference (EMI). Also note that in the unit cell configuration a ground plane is not present.

The two-dimensional electric field distribution for the proposed scheme can be solved using conformal mapping techniques [43]. As the flux lines are elliptical and the equipotential lines are hyperbolic, the best way to attack this problem is to use inverse cosine transforms. Similar types of approaches were adopted in [43, 44]. As it is a solution of the two-dimensional electric field, the lengths of the electrodes are taken as

infinitely long. The electric fluxes start at the driving electrode, penetrate the material under test (MUT) and then end at the sensing electrode. We made the following assumptions for this analysis,

1. The thickness of the MUT on either side of the sensor surface h_m, must be greater than the field penetration depth T, corresponding to the maximum vertical displacement of field lines in the y direction, *i.e.*,$h_m > T$.
2. The substrate thickness is negligible compared to the height of the MUT *i.e.*,$h_s \ll h_m$, so that the flux distribution is not perturbed by the substrate material.
3. The electrode height $h_e$is negligible compared to the height of the MUT *i.e.*,$h_e \ll h_m$. As a result, the direct fluxes between the two electrodes are also negligible.

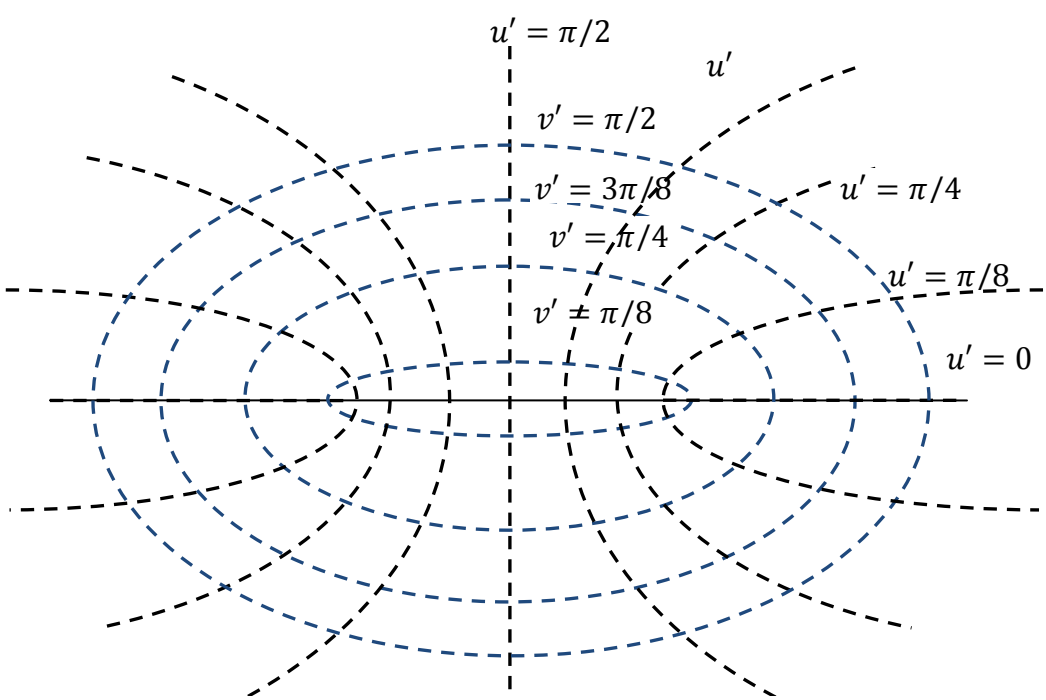

Figure 2.4. Plot of the general inverse-cosine transformation $u' + jv' = \cos^{-1}(x' + jy')$ [43].

Referring to Fig. 2.4 suppose that we want to convert the rectangular plane $x' - y'$plane to the inverse cosine plane $u' - v'$ plane.

Then, the general solution of the inverse-cosine transform is

$$W' = \cos^{-1} Z' \tag{2.3}$$

which means each assigned value of $Z' = x' + jy'$ position vector in the $x' - y'$ plane has a specific corresponding value in the $W = u' + jv'$ position in the $u' - v'$ plane. Therefore,

$$Z' = \cos W' \tag{2.4}$$

$$x' + jy' = \cos(u' + jv') = \cos u' \cosh v' - j \sin u' \sinh v' \tag{2.5}$$

$$x = \cos u' \cosh v' \tag{2.6}$$

$$y = -\sin u' \sinh v' \tag{2.7}$$

Then we can write,

$$\frac{x'^2}{\cosh^2 v} + \frac{y'^2}{\sinh^2 v} = 1 \tag{2.8}$$

$$\frac{x'^2}{\cos^2 u} - \frac{y'^2}{\sin^2 u} = 1 \tag{2.9}$$

However, for this particular problem, a single pair of co-planar conducting plates of infinite length are surrounded by a homogeneous dielectric medium with permittivity of ϵ_r. The fixed potential of the right conducting plate (the driving electrode) is V_0 and the fixed potential of the left conducting plate(the sensing electrode) is 0. Therefore, the specific transformation will be

$$W = \mathrm{C}_1 \cos^{-1} kZ + C_2 \tag{2.10}$$

Where,

$$Z' = kZ \tag{2.11}$$
$$W = C_1 W' + C_2 \tag{2.12}$$

The constant C_1 and C_2 are to be taken as real for this problem. Therefore,

$$u = C_1 u' + C_2 \tag{2.13}$$

Here, for our specific problem, the rectangular plane is the $x - y$ plane (see Fig. 2.3) and the transformed plane is $u - v$ plane (see Fig. 2.5).

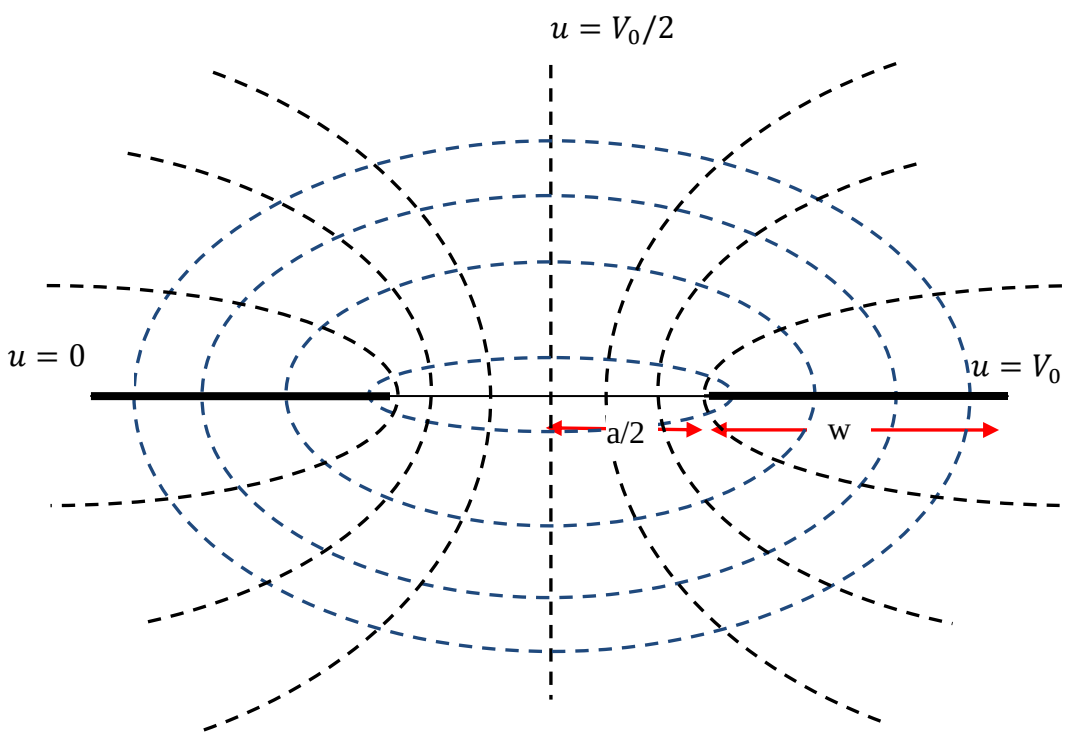

Figure 2.5. Fields between co-planar metal planes with a finite gap [43].

Comparing Figs. 2.4 and 2.5, we want Z to be $a/2$ when Z' to be unity, thus $k = 2/a$. Then, when $u' = 0$, we want $u = V_0$ and when $u' = \pi/2$, $u = V_0/2$. Substituting these values in equation (2.13), we can come up with

$$C_1 = -\frac{V_0}{\pi}, C_2 = V_0 \tag{2.14}$$

Hence the exact inverse-cosine transformation function with proper scale factor is

$$W = u + jv = V_0\left[1 - \frac{1}{\pi}\cos^{-1}\left(\frac{2Z}{a}\right)\right] \tag{2.15}$$

Where $u(x, y)$ is the electrical potential function and $v(x, y)$ is proportional to the electrical flux function.

From (2.15)

$$Z = x + jy = \frac{a}{2}\cos\left[\frac{\pi}{V_0}(V_0 - u) - \frac{j\pi v}{V_0}\right] \tag{2.16}$$

Therefore we can rewrite x and y in terms of u and v

$$x = \frac{a}{2}\cos\left[\frac{\pi}{V_0}(V_0 - u)\right]\cosh\left[\frac{\pi v}{V_0}\right] \tag{2.17}$$

$$y = \frac{a}{2}\sin\left[\frac{\pi}{V_0}(V_0 - u)\right]\sinh\left[\frac{\pi v}{V_0}\right] \tag{2.18}$$

From the above equations, we can easily separate u and v

$$\frac{x^2}{\cosh^2\left(\frac{\pi v}{V_0}\right)} + \frac{y^2}{\sinh^2\left(\frac{\pi v}{V_0}\right)} = \frac{a^2}{4} \tag{2.19}$$

$$\frac{x^2}{\cos^2\left(\frac{\pi}{V_0}(V_0 - u)\right)} - \frac{y^2}{\sin^2\left(\frac{\pi}{V_0}(V_0 - u)\right)} = \frac{a^2}{4} \tag{2.20}$$

We can find the penetration depth, T, at $x = 0$. Observing (2.23) penetration depth T will be,

$$T = \frac{a}{2}\sinh\left(\frac{\pi v}{V_0}\right) \tag{2.21}$$

Maximum penetration would occur at the right most side of the electrode where $x = \frac{a}{2} + w$and $= +V_0$. From (2.18) we can write,

$$\frac{a}{2} + w = a/2\cosh\left(\frac{\pi v}{V_0}\right).$$

Or,

$$\frac{\pi v}{V_0} = \cosh^{-1}\left(1 + \frac{2w}{a}\right) \tag{2.22}$$

So penetration depth, T,

$$T = a/2\sinh\left[\cosh^{-1}\left(1 + \frac{2w}{a}\right)\right] \tag{2.23}$$

Using hyperbolic trigonometry we can write,

$$T = \frac{a}{2}\sqrt{\left(1 + \frac{2w}{a}\right)^2 - 1} \tag{2.24}$$

According to Fig. 2.3, $b - a = 2w$we can write

$$T = \frac{a}{2}\sqrt{\left(1 + \frac{b-a}{a}\right)^2 - 1}$$

$$T = \frac{a}{2}\sqrt{\left(\frac{b}{a}\right)^2 - 1} \tag{2.25}$$

From (2.24) and (2.25), we can estimate the penetration depth (T) with respect to the width of the electrode and the gap between the two electrodes for a unit cell.

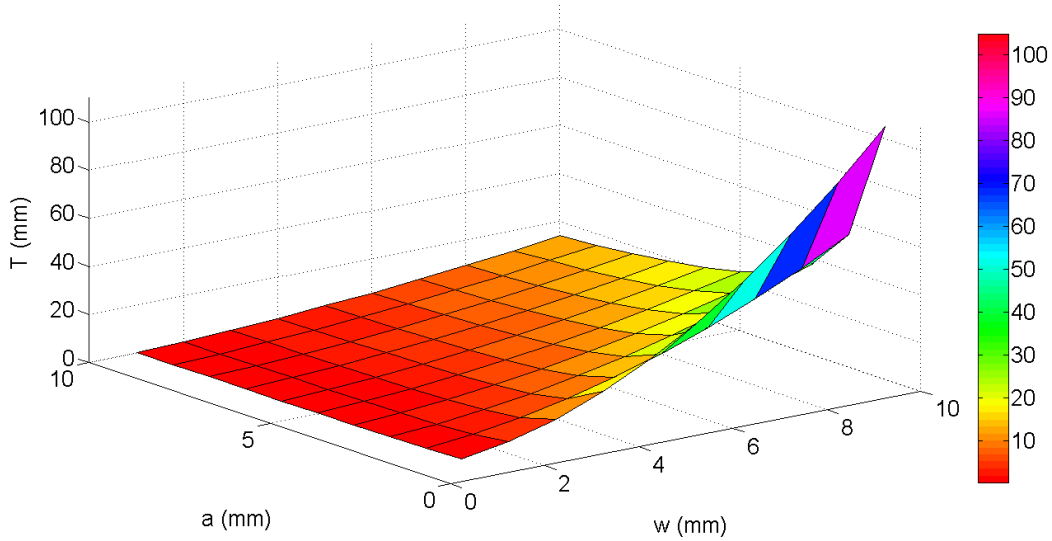

Figure 2.6. Field penetration depth, T mm versus electrode width w mm and the distance between the two electrodes, a mm

The variation of the field penetration depth T, with respect to w from 1 mm to 10 mm and a from 1 mm to 10 mm is plotted in Fig. 2.6. From this graph and also from (2.24), it is evident that the field penetration depth increases with the increase in w/a.Next figures, Fig 2.7 and Fig 2.8 also help us more to understand the relationship between T, a, and w.

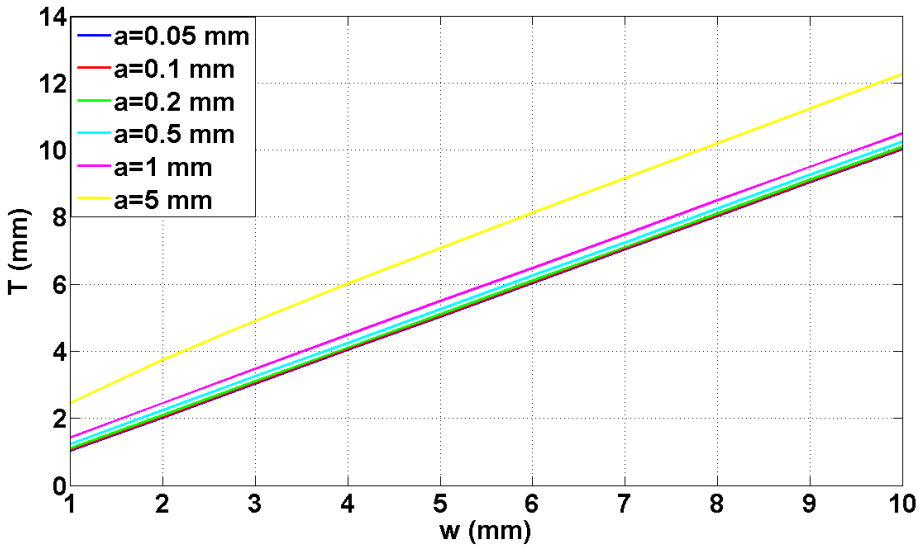

Figure 2.7. Field penetration depth, T mm versus electrode width w mm for a=0.05 mm, 0.1 mm, 0.2 mm, 0.5mm, 1mm and 5 mm.

In Fig. 2.7, we plot T versus w for the distance between the two electrodes varying from 0.05 mm to 5mm. The width of each electrode, w affects the penetration depth T more than the interelectrode separation a does. From the figure, for w=2 mm penetration depth increases from 2.5 to 3.7 mm while a increases from 1 mm to 5 mm. In contrast, the penetration depth doubles as w doubles.

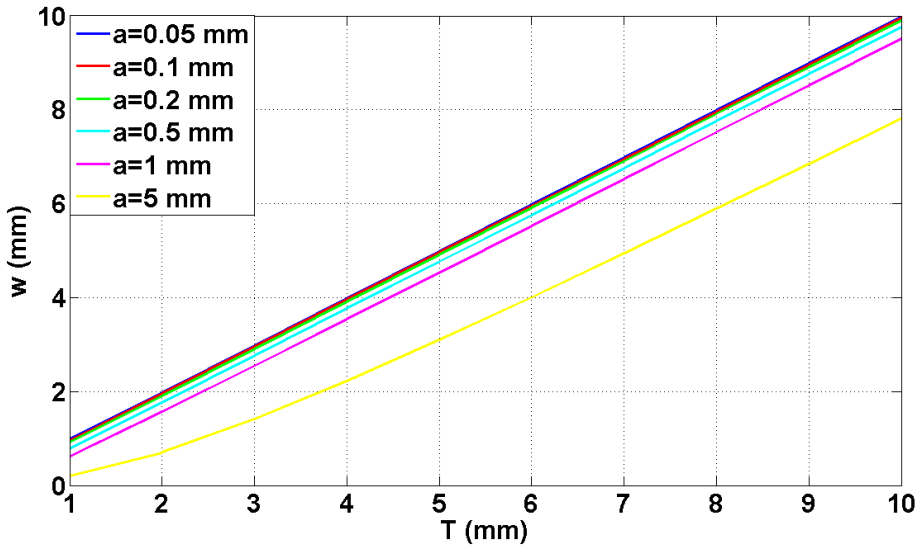

Figure 2.8. Electrode width w mm, versus field penetration depth, T mm for, a=0.05 mm, a=0.1 mm, a=0.2 mm, a=0.5 mm, a=1 mm and a=5 mm.

We can make similar observations from Fig. 2.8. These curves represent the design parameters for a certain penetration depth. For 'a' less than 0.5, the slope of the curves is nearly 1 and thus w=T. However, as 'a' increases 'w' diverges from the w=T relationship. For example, for a= 5mm and penetration depth 5 mm we need w=4 mm. For T less than 2 mm and a =5 mm, the w versus T curve is nonlinear. This can be explained from (2.27). When$\frac{w}{a} > 1$, (2.24) becomes $T \approx \frac{a}{2} + w$ which is a straight line and again if $\frac{w}{a} \gg 1$, we can simply write $T = w$.

We can also calculate the capacitance for this specific analytical model. The displacement vector is [23]

$$D = -\epsilon_0 \epsilon_m \frac{\partial u}{\partial y} \tag{2.26}$$

The total charge on the positive conductor Q can be approximated by integrating the electric displacement vector along the plane $= 0$. However, along the plane $y = 0$ on the surface of the positive electrode$\left(\frac{a}{2} \leq x \leq \frac{a}{2} + w\right)$, the potential equals to $V_0 i.e., u = V_0$. Therefore, there is no derivative of electric flux$\left(\frac{\partial v}{\partial y}\right)_{y=0}$ on this plane. Using Gausses Law, we can derive the total electric charge present on the electrode

$$Q = \oint \boldsymbol{D}\,(y = 0)\ \cdot d\boldsymbol{A} = 2l \int_{a/2}^{\frac{a}{2}+w} |\boldsymbol{D}(y = 0)|\, dx \tag{2.27}$$

Solving (2.20) with respect to the boundary condition$i.e., y = 0$ and $u = V_0$, we can write

$$x = \frac{a}{2} \cosh\left(\frac{\pi v}{V_0}\right) \tag{2.28}$$

Differentiating (2.18) with respect to y and using the boundary condition $i.e., y = 0$ and $u = V_0$ we can write,

$$\left(\frac{\partial u}{\partial y}\right)_{y=0} = \frac{2\,V_0}{\pi a \sinh\left(\frac{\pi v}{V_0}\right)_{y=0}} \tag{2.29}$$

Therefore (2.27) becomes

$$\begin{aligned}
Q &= \frac{4V_o \epsilon_r \epsilon_0 l}{\pi a} \int_{a/2}^{\frac{a}{2}+w} \frac{dx}{\sinh\left(\frac{\pi v}{V_0}\right)_{y=0}} \\
&= \frac{4V_o \epsilon_r \epsilon_0 l}{\pi a} \int_{a/2}^{\frac{a}{2}+w} \frac{dx}{\sqrt{\left(\frac{2\mathrm{x}}{\mathrm{a}}\right)^2 - 1}} \\
&= \frac{4V_o \epsilon_r \epsilon_0 l}{\pi a} \int_{1}^{1+\frac{2w}{a}} \frac{\frac{a}{2} dX}{\sqrt{(\mathrm{X})^2 - 1}}\ ; (Let\ X = \frac{2x}{a}) \\
&= \frac{2V_o \epsilon_r \epsilon_0 l}{\pi} \int_{1}^{1+\frac{2w}{a}} \frac{dX}{\sqrt{(\mathrm{X})^2 - 1}} \\
&= \frac{2V_o \epsilon_r \epsilon_0 l}{\pi} \ln\left[\left(1 + \frac{2w}{a}\right) + \sqrt{\left(1 + \frac{2w}{a}\right)^2 - 1}\right]
\end{aligned} \tag{2.30}$$

Then, the total capacitance can easily be calculated using the potential difference between the electrodes which is V_0 for this specific case. Therefore,

$$C = \frac{Q}{V_0}$$
$$C = \frac{2\epsilon_r \epsilon_0 l}{\pi} \ln\left[\left(1 + \frac{2w}{a}\right) + \sqrt{\left(1 + \frac{2w}{a}\right)^2 - 1}\right] \tag{2.31}$$

According to Fig. 2.3, $b - a = 2w$, so we can rewrite the above equation

$$C = \frac{2\epsilon_r \epsilon_0 l}{\pi} \ln\left[\frac{b}{a} + \sqrt{\left(\frac{b}{a}\right)^2 - 1}\right] \tag{2.32}$$

From (2.31) and (2.32), we can calculate the variation of the total capacitance with respect to the variation of w and a for a unit cell, if the other parameters remain constant. The variation of the total capacitance C with respect to w from 1 mm to 100 mm and a is from 1 mm to 10 mm is plotted in Fig. 2.9 according to (2.31).

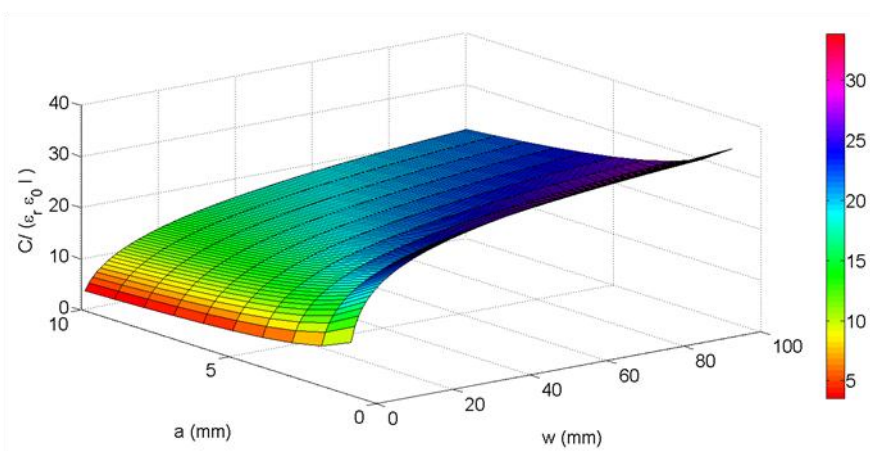

Figure 2.9. $\frac{C}{\epsilon_r \epsilon_0 l}$versus the electrode width w and the distance between two electrodes a.

Figure 2.9 describes the surface plot of per unit length capacitance without considering the dielectric constant of the material (or considering only air) $\frac{C}{\epsilon_r \epsilon_0 l}$ with respect to

electrode width ‘w’ and the distance between the two electrodes ‘a’. We can observe that capacitance decreases with increasing electrode separation ‘a’ and increases with increasing electrode width ‘w’. Fig. 2.10 further clarifies Fig. 2.9.

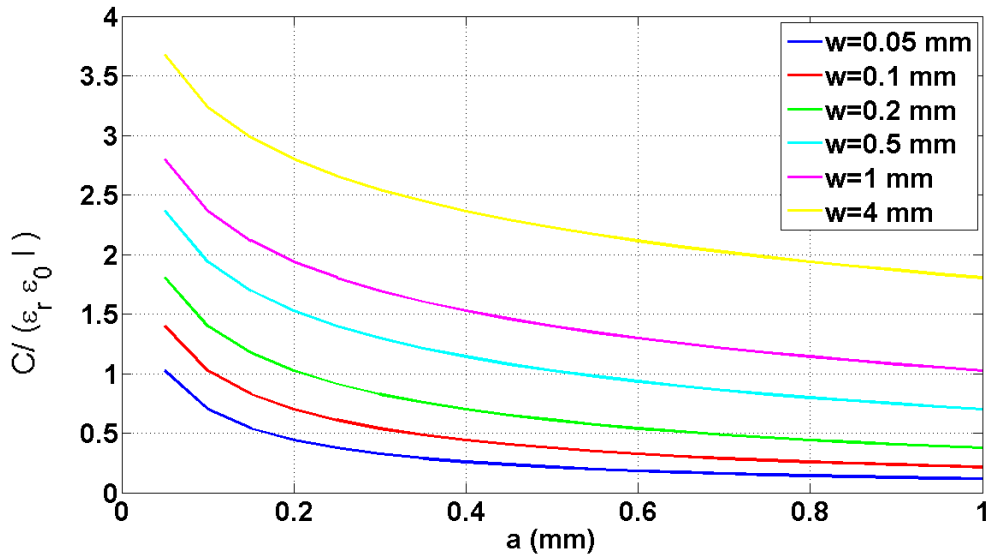

Figure 2.10. $\frac{C}{\epsilon_r \epsilon_0 l}$versus the electrode width w and the distance between two electrodes a.

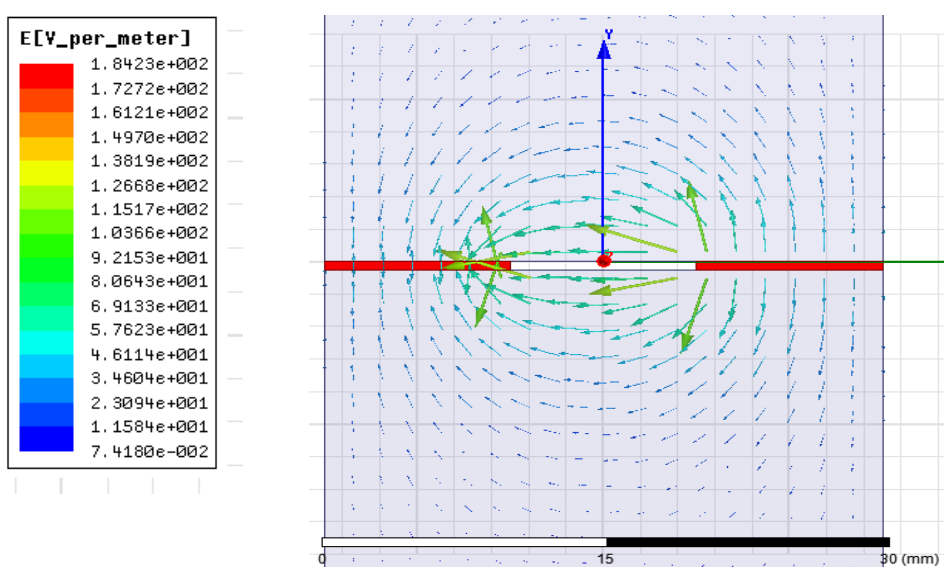

Figure 2.11. Plot of vector electric field in Ansys Maxwell 2D for W=10 mm and a=10mm.

For comparison, we simulated a unit cell interdigitated capacitor using Ansys Maxwell 2D as shown in Fig. 2.11. The two red rectangular boxes represent the driving and the sensing electrodes. The driving electrode was set to $10\,V$ and the sensing electrode was set to $0\,V$. The heights of the electrodes were set to 0.5mm. We assigned copper as their material property. The relative permittivity, ϵ_r of the material considered for the simulations was 2.2 (Duroid 5880). The two large light blue shaded boxes on the top and on the bottom represent the material under consideration. The heights of the boxes are 50 mm and the widths of the boxes are equal to the width of the unit cell. In Maxwell 2D, the solution method is electrostatic. The edges of the two boxes did not need to be explicitly defined because it remained as a natural surface. In Maxwell 2D, initially all the objects are surfaces that are predefined as natural boundaries, which means that the vector electric field is continuous across the surface. All outside edges of the metal boxes are defined as Neumann Boundaries, which means that the surface is continuous for tangential E field component and normal for D field component. The observed plot of the vector electric field is shown in Fig 2.11 for $w = 10$ mm and $a = 10$ mm. Electric field lines started from the positive electrode (on right side of the figure) and ended at the negative electrode (on the left side of the figure).

Table 2.1: Comparison between analytical solution and simulation results from Ansys Maxwell 2D for different w/a.

w (mm)	a (mm)	W/a	Analytical equation (2.34) $\epsilon_r = 2.2$ C/l (pF/m)	Ansoft Maxwell 2D $\epsilon_r = 2.2$ C/l (pF/m)	Error
1	1	1	21.86	25.45	14%
2	1	2	28.43	32.3	12%
5	1	5	38.31	42.21	9%
10	1	10	46.34	50.13	7%
20	1	20	54.64	58.58	6%
2	2	1	21.85	25.51	14%
5	5	1	21.85	25.67	15%
10	10	1	21.85	25.34	14%

A comparison between the analytical (2.31) and simulation results is summarized in Table 2.1. As apparent, the percentage of error in the analytical simplified model results compared to the simulation results decreases from 14% to 6% as $\frac{w}{a}$increases from 1 to 20. If both 'w' and 'a' are the same (for constant $\frac{w}{a}$=1) such as 1, 2, 5 and 10 mm the error is almost constant which is close to 14%. Therefore, Table 2.1 confirms that when $\frac{w}{a}$increases, the discrepancy between the analytical solution and the simulation result decreases. It is clear that larger electrode size and small separation are key to achieve higher capacitance and hence better measurement quality. Similarly, larger electrode size will allow strong field penetration depth. However, from a practical fabrication and implementation point of view these are not always desirable. Thus design optimization is

often necessary. Interestingly however, the simulation results always provide higher capacitance then the analytical thus the analytical results should be considered as conservative first order values. This means that the actual sensitivity should be slightly better.

CHAPTER 3

STATIC FIELD SENSING-MOISTURE SENSING IN CONCRETE USING INTERDIGITATED SENSORS

As mentioned, there has been a plethora of research activities on sensor design, development and system level integration to monitor the health of infrastructure, such as bridges, overpasses, airport runways etc. Measuring moisture inside concrete, particularly near the steel reinforcement is important because moisture is a precursor of corrosion [45].

Moisture measurement in materials has been investigated by researchers in the past. Xing *et al.* [46] developed a 2.4GHz integrated parallel-plate soil moisture sensor system. The sensor detects the phase shift caused by the changes in the dielectric constant of soil which is related to the soil moisture content. This sensor needs a number of components, such as a PLL (phase locked loop), VCO (voltage controlled oscillator), phase shifter, phase detector, microcontroller and power management circuitry on board to be fully functional. In [47], Saxena and Tayal described a parallel-plate capacitor as a moisture sensor. The sensor consists of a Weinbridge oscillator, a capacitance bridge, a differential amplifier, a band-pass filter, a rectifier circuit, and an analog meter. Ong *et al*. [48] proposed a 24 MHz embedded *LC* resonant sensor for moisture content measurement, which requires a large external loop and an impedance analyzer. Similarly, there are other examples of sensor that utilize an antenna or a resonator. Instead, an

interdigitated capacitor sensor should be preferred for concrete moisture content measurement because of its miniature size and conformal geometry. Justifiably, interdigitated sensors have been used in many applications in the past [49-52].

In this Chapter, the design and investigation of two interdigitated sensors are presented when used in concrete moisture content measurement.

3.1 SENSOR GEOMETRY AND DESIGN DETAILS

An interdigitated sensor is a coplanar structure consisting of multiple parallel fingers. The sensor can measure material dielectric constant by applying fringing electric fields into the material. The electrodes of the sensor must be in contact with the material under test. Fig. 3.1 shows the geometry of an interdigitated sensor [49]. Three types of electrodes are present, namely the driving electrode, the sensing electrode, and the guard electrode. A sinusoidal voltage V_D is applied to the driving electrode and the output voltage V_S is measured from the sensing electrode. Guard electrodes and a conducting backplane are used to shield the sensor from the influence of external fields [29]. Another important term is the field penetration depth, T. A detailed analysis of T is conducted and presented in Chapter 2 which showed that this parameter is a function of electrode width and spacing.

A popular method to find the dielectric constant of a material is the short-circuit current method, which is shown in Fig. 3.2. A low frequency voltage V_D is applied to the driving electrode while the sensing electrode is connected to a precision opamp (AD708). The opamp acts as an inverting amplifier where a known capacitor C_F is used for feedback.

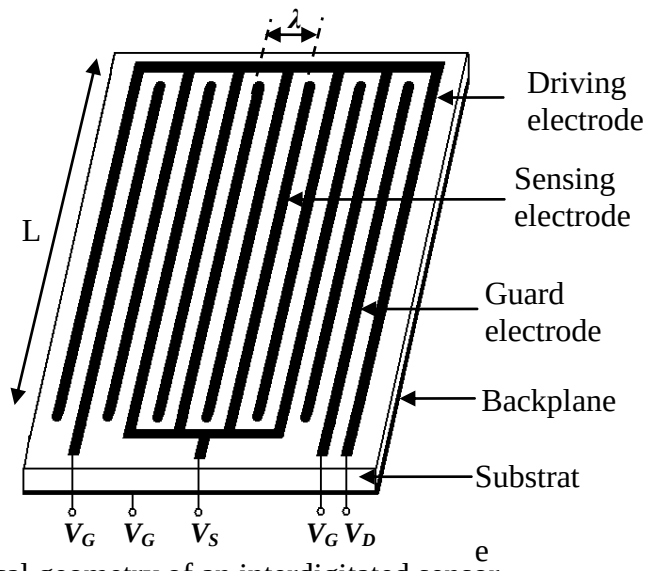

Figure 3.1. The typical geometry of an interdigitated sensor.

We used a simplified circuit model in Fig. 3(b) to calculate the capacitance between the driving and the sensing electrodes. The substrate has zero conductivity, so the current is due to the capacitive effect only. Also since the opamp is operating in the inverting mode, it is obvious that

$$C_{DS} = \frac{V_F}{V_D} C_F. \tag{3.1}$$

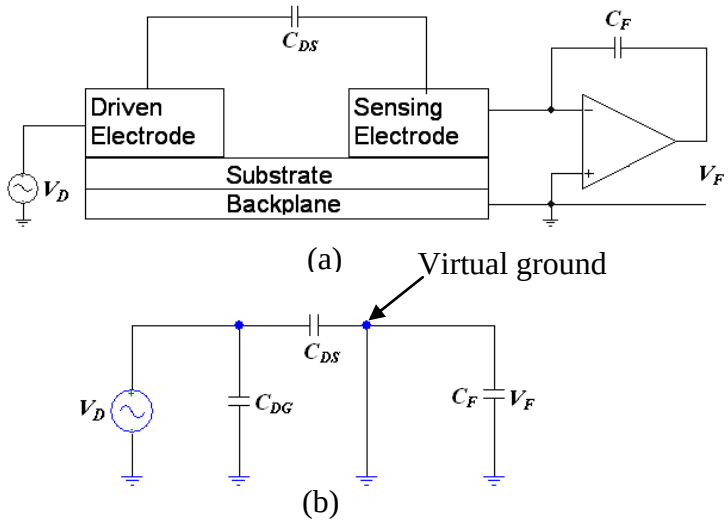

Figure 3.2. (a) Block diagram of sensor circuit and its (b) equivalent circuit.

3.2 EXPERIMENTAL SETUP

To detect the percentage of moisture in concrete two interdigitated sensors were designed and fabricated. One was a meander sensor and the other was a circular sensor. Two sensor configurations were chosen to create different field penetration depths. The meander sensor is simpler and has smaller field penetration depth than the circular sensor. For the same field penetration depth the circular sensor covers a larger surface area than the meander sensor. The electrode width, height, gap and spatial wavelength of the meander sensor were 1.125 mm, 17 μm, 1.125 mm, and 4.5 mm, respectively. Thus the field penetration depth T from Fig. 2.9 for the meander sensor is about 1.75 mm. For the circular sensor these dimensions were 1.5 mm, 17 μm, 2 mm and 7 mm, respectively. Hence the field penetration depth for the circular sensor is > 2 mm. The meander sensor was fabricated on a 10 mil thick Duroid 5880 ($\epsilon_r = 2.2$) substrate and the circular sensor was fabricated on a 31 mil thick Duroid 5880 substrate. Referring to Fig. 3.1, the meander sensor had 7 driving electrodes, 4 sensing electrodes and 2 guard electrodes. The length of each electrode was 20 mm. For the circular sensor (see Fig. 3.5), the inner diameter of the innermost sensing electrode was 6 mm. The circular sensor had 12 driving electrodes, 10 sensing electrodes and 2 guard electrodes. Both sensors were coated with very thin perylene coating to avoid short circuit with the concrete, especially in the wet condition. A 1 kHz, $10V$ (peak) sinusoidal signal was chosen for V_D. The amplitude of the signal was small enough to prevent the opamp from saturating. The feedback capacitor C_F was 100 pF.

Concrete block samples were prepared using concrete mix. The age of the samples was more than one year at the time of the measurement. The dimensions of the samples were 15 cm × 15 cm × 2 cm and 15 cm × 15 cm × 4 cm.

The wet basis for the moisture content in a material is defined as

$$M_w = \frac{m_w - m_d}{m_d} \times 100 \tag{3.6}$$

where m_w is the mass of the specimen with water and m_d is the mass of the specimen in dry condition. The moisture content of a material by volume M_v can be calculated as

$$M_v = \frac{\rho_d}{\rho_w} \times M_w \tag{3.7}$$

where ρ_d is the density of concrete in dry condition and ρ_w is the density of water.

For measurement, the sensor was placed between two concrete samples. First, the sensor output voltage V_F was measured for the samples in dry condition. Since V_D was known, the capacitance C_{DS} was found using (3.1). After completion of the measurement in dry condition the concrete samples were weighed in a scale to determine m_d. Then the samples were placed in a 13.5 liter water bucket and were completely submerged in water for two days.

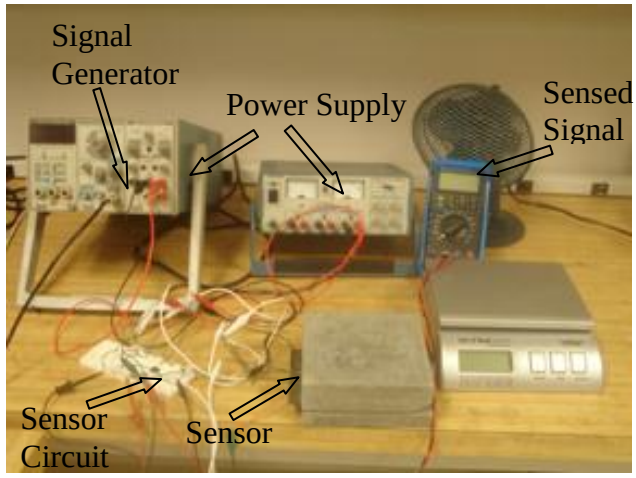

(a)

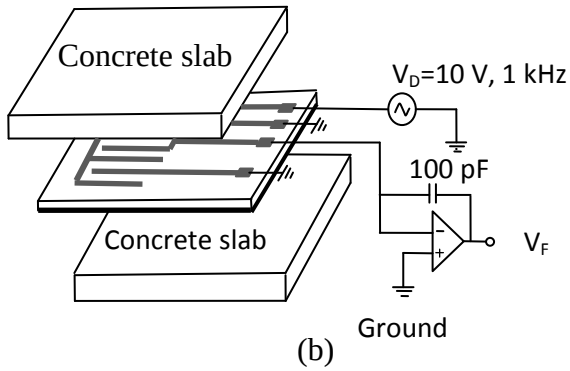

(b)

Figure 3.3. (a) Experimental setup to measure C_{DS} for concrete samples, (b) placement of the sensor in the samples.

Wet samples were taken out from the water bucket. Since excess water present on the concrete surface had the potentials for erroneous results (high V_F and high C_{DS}) due to the high permittivity of water the outer surfaces of the samples were wiped off using a dry cloth. The sensor was placed between the wet concrete samples. At regular periodic intervals, V_F was recorded and the weight of the concrete samples m_w was measured. For each reading, C_{DS} was found using (3.1) while the moisture content M_V was found using (3.6) and (3.7). Thus for each case a new M_V and its corresponding C_{DS} was found. Since the evaporation rate depended on the environment, the ambient temperature and the air

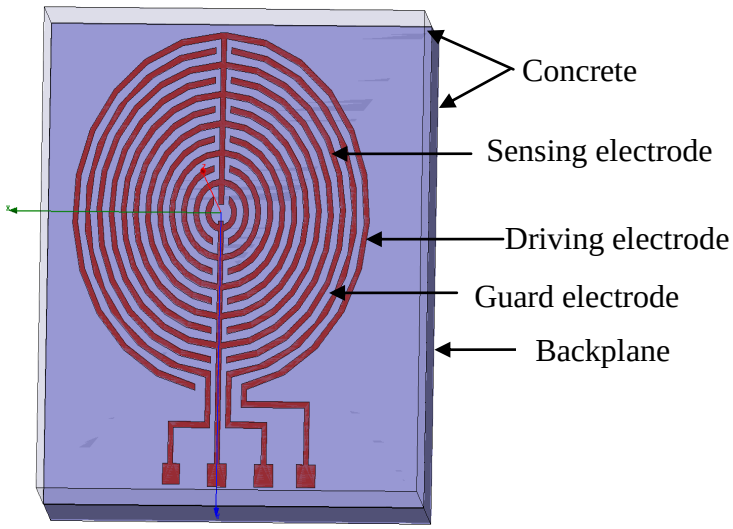

Figure 3.4. Ansoft Maxwell 3D model of full circular sensor.

flow, an external fan was used to make the evaporation process faster.

3.3 RESULTS

3.3.1 EXPERIMENTAL RESULTS

Measured C_{DS} versus M_V data for both the meander and the circular sensor are shown in Fig. 3.6. A linear regression analysis was also performed on the measured data. From Fig. 3.6(a), in dry condition C_{DS} =2.45 pF while for M_V =5.968, C_{DS} =5.548 pF. The presence of water in the wet concrete clearly resulted in the increase in C_{DS}(126.4% increase). The sensitivity of the meander sensor is 0.519 pF/percent change in moisture content. Fig. 3.6(a) also shows that the coefficient of determination r^2=0.9397 when $M_v < 6\%$. Measured C_{DS} versus M_V results for the circular sensor are shown in Fig. 3.6(b). Since the field penetration depth of the circular sensor is larger than that of the meander sensor the resulting linear regression curve in Fig. 3.6(b) is steeper than the curve in Fig. 3.6(a). The coefficient of determination r^2 =0.9858. In dry condition

C_{DS}=17.385 pF while with M_V =5.968, C_{DS} =49.934 pF (187% increase). The sensitivity of the circular sensor is 5.454 pF/percent change in moisture content.

3.3.2 COMPARISON BETWEEN EXPERIMENTAL AND SIMULATION RESULTS

Ansoft Maxwell 3D was used to simulate the sensor responses for both the meander and the circular sensors. Fig. 3.5 is an example of the simulation model which was used for the full circular sensor. In the simulation, we were not able to account for the moisture content directly. In [53], experimental data of relative permittivity and conductivity versus frequency for four different levels of moisture content in concrete (from Fig. 2 of [53]) are available. These data are valid for the frequency range of 10 MHz to 1 GHz. We extended their curves down to 1 kHz using curve fitting in Matlab. Then we developed linear relations between the relativity permittivity and conductivity with percentage of moisture content using curve fitting. The resulting relative permittivity and conductivity values were used in our Maxwell simulations. The relative permittivity (ε_r) and conductivity (σ) of the concrete samples that were used in our simulation and analytical equations (3.3)-(3.4) were: 4.4323, 0.000224; 6.0333, 0.0009; 7.177, 0.00215; 8.549, 0.00444; and 9.693, 0.007 for moisture contents of 0%, 1.816%, 3.1135%, 4.67% and 5.968%, respectively.

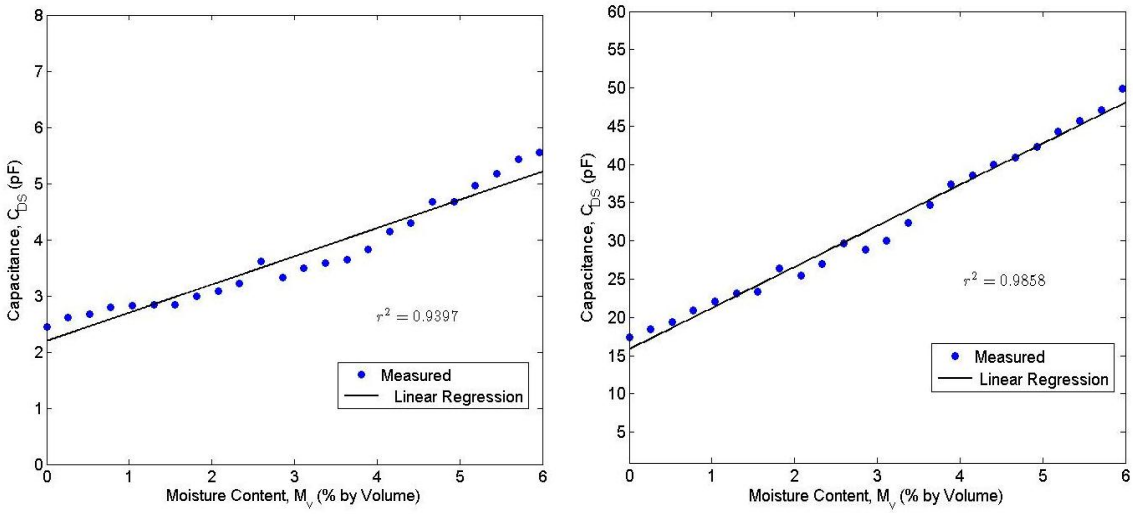

(a) (b)

Figure 3.5. Measured capacitance, C_{DS} versus moisture content, M_V for (a) the meander sensor and (b) the full circular sensor.

In Maxwell 3D the solution type was electrostatic. The driving electrodes were set to 10V and the other electrodes including the backplane were set to 0V. The default boundary condition, the Neumann homogeneous condition was used. The capacitances between the driving electrodes and the sensing electrodes were computed for the four different cases. Since the analytical equations (3.2) to (3.5) can only correctly describe the capacitance for the meander sensor, analytical results were obtained only for the meander sensor.

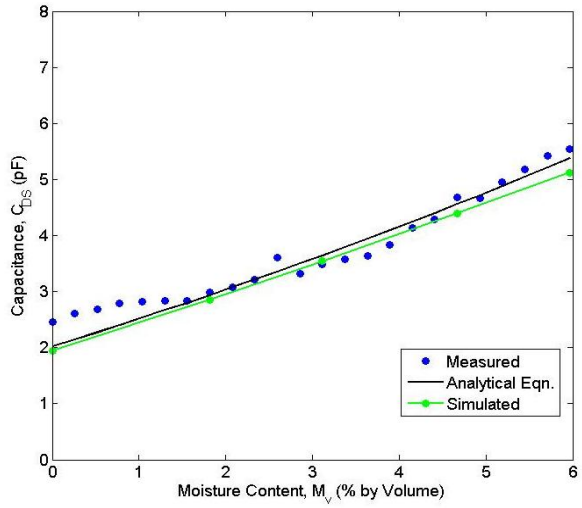

Figure 3.6. Comparison between the measured, analytical and simulated data for the meander sensor.

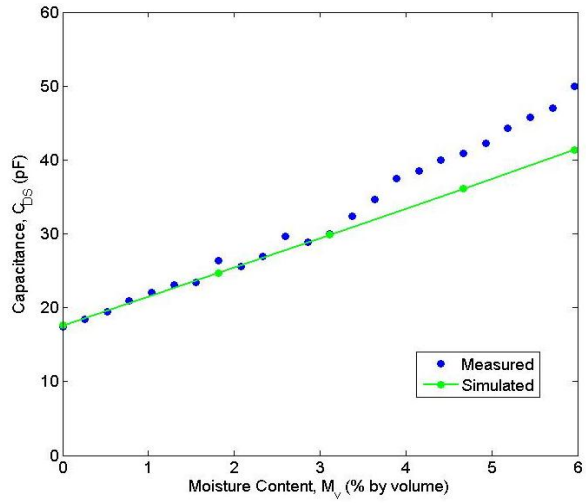

Figure 3.7. Comparison of measured and simulated capacitance for the full circular sensor.

Comparison between the experimental, simulation and analytical data for the meander sensor is shown in Fig. 3.7. As seen, in general the agreement between all three is quite good. Some deviation is observed at higher moisture content levels. Fig. 3.8 illustrates the comparison between the experimental and simulation results for the circular sensor. Again, agreement is excellent for low moisture content. The measured

results are 10% to 20% higher than the simulated results for moisture contents larger than 4%.

The measurement data clearly indicate that both types of sensors can detect and measure moisture in concrete. There is a distinctly linear relationship between the moisture content in the concrete and the measured interelectrode capacitance. Hence, the amount of moisture present can be easily predicted from the measured capacitance. The disagreement between the simulation and measurement data can be due to the following. First, as mentioned, in our Maxwell simulations the exact values of the relative permittivity and conductivity of concrete at 10 kHz and as function of moisture content was not available. We used curve fitting to extrapolate from the measured permittivity and conductivity data of concrete that was valid from 10 MHz to 1GHz. Since Maxwell does not use moisture content values directly accurate values of relative permittivity and conductivity are essential to obtain accurate simulation results. Second, perhaps during wiping off the concrete surface there was some standing water on the concrete surface. Although the outside concrete surfaces were wiped off with a dry cloth but the uneven surface might have allowed for some water to still remain on the surface.

CHAPTER 4

PROPAGATING WAVE SENSING- THE THEORY OF SURFACE WAVE PROPAGATION

In Chapters 2 and 3, the analysis, design and experimental results of proximity capacitive sensors are presented. The EM waveforms injected into the MUT generated static and localized fields which were perturbed when the properties of the MUT changed. There are many sensing applications where a propagating wave instead of a static field is needed. This is so because the location at which the measurement or diagnosis needs to be performed is not at the same location as the source. For example, consider Surface Acoustic Wave (SAW) sensing where sensors create SAW waveforms in composites or other aero structures [54, 55].Similar is the case for cable or wiring fault detection where propagating waves are used in conjunction with TDR, FDR or JTFDR to detect open, short or other faults [56-60]. One potential example is a propagating surface wave. The objective is to inject it at the conductor dielectric interface of an insulated unshielded cable and then use it further to detect cable faults such as open circuit and insulation damage. This Chapter presents the summary of the literature on surface wave theory. Section 4.1 gives a concise review of Sommerfeld's surface wave work. In Section 4.2 we summarize Georg Goubau's work and in Section 4.3 the more recent work done by Glenn Elmore is described. Finally we summarize the review with some concluding remarks.

4.1 SOMMERFELD'S WORK

Sommerfeld [61] and his student Zenneck [40] first theoretically investigated the phenomenon of wave propagation over imperfect conductors known as surface waves. Sommerfeld theoretically investigated the propagation of non-radiating waves on a metal wire with finite conductivity and circular cross section. He also found that this non radiating mode is transverse magnetic and the wave solution came from the Maxwell equations. For example, if the wave is propagating in the +z direction, the field components are expressed as follows in the cylindrical coordinate system (see Fig. 4.1).

The radial component of the electric field is

$$E_r = jA\frac{\gamma}{u'}Z_1(u'r)e^{j\omega t-\gamma z} \tag{4.1}$$

The longitudinal component of the electric field is

$$E_z = A\,Z_0(u'r)e^{j\omega t-\gamma z} \tag{4.2}$$

The magnetic field component in a plane transverse to the conductor is

$$H_\phi = jA\frac{k^2}{\omega\mu u'}Z_1(u'r)e^{j\omega t-\gamma z} \tag{4.3}$$

Here, z indicates the distance along the cable and r indicates the distance from the wire center, γ is the propagation constant of the guided wave which is equal to $(\alpha + j\beta)$. The free-space wave propagation constant k inside and outside the wire is defined as

Inside the conductor $$k_c = \sqrt{\omega\mu_c\sigma_c}\,e^{-j\frac{\pi}{4}} \tag{4.4}$$

Outside the wire $$k = \omega\sqrt{\epsilon\mu}$$

where $\mu =$ permeability, $\epsilon =$permittivity and $\sigma =$ conductivity and the subscript c indicates that the region is inside the wire. $u'$is the radial decay function defined by the following relations

$$u_c'^{\,2} = k_c^2 - \beta^2 \,, \qquad u'^2 = k^2 - \beta^2$$

Where $\beta = 2\pi/\lambda_g$, where λ_g= wavelength of the surface wave. Inside the wire, the function Z is replaced by the Bessel function J and outside the wire the function Z is replaced by the Hankel function of the first kind $H^{(1)}$.

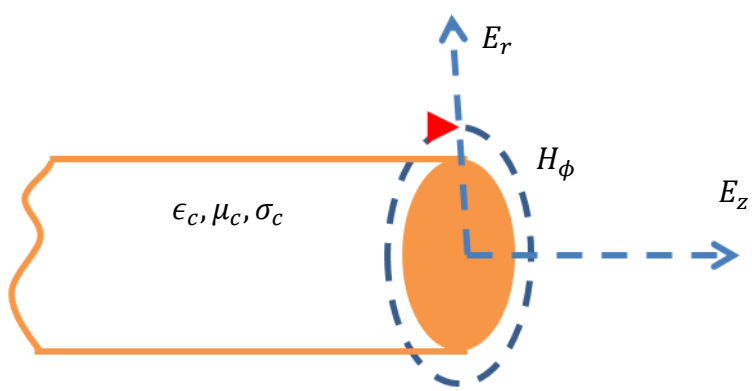

Figure 4.1.Graphical representation of Sommerfeld's wire/line with finite conductivity.

Suppose, a is the radius of the finite conductive wire. Then E_z and H_ϕ must be continuous at the surface $r = a,$ which is the boundary condition of this problem. Therefore

$$\frac{\mu u' H_0^1(u'r)}{k^2 H_1^1(u'r)} = \frac{\mu_c u_c' J_0(u_c' r)}{k_c^2 J_1(u_c' r)}$$

$$u_c'^2 - u^2 = k_c^2 - k^2 \tag{4.5}$$

From these above equations, other quantities such as attenuation, region of energy flow and other quantities can be calculated. For detailed analysis, please review [62]. Sommerfeld only considered the low frequency TM_{01} mode. Other higher order modes may exist on a single wire transmission line, however in practical case, because of high attenuation they can be easily disregarded for long distance wave propagation [62].

4.2 GEORG GOUBAU'S WORK

Sommerfeld's waves only exist for a conductor with finite conductivity. For Sommerfeld's waves, if the conductivity is very high, the extension of the field goes to infinity. Georg Goubau suggested that coating a metal wire with dielectric or periodic corrugation will reduce the radial extension of the electric field by increasing the surface reactance. And for these cases, the conductivity does not have much effect on the extension of the radiated field [41, 63, 64]. Fig. 4.2 shows a graphical representation of a cable which supports TM waves according to Goubau's principle. The field in the dielectric layer can be described by the Bessel function (J_0, J_1) and the Neumann function (N_0, N_1). Therefore, in (4.1)-(4.3) Z_0 and Z_1 can be replaced by

$$Z_0 = J_0 + bN_0, \qquad Z_1 = J_1 + bN_1$$

Using the boundary condition $E_z = 0$ he derived that for the radius of the wire a and radius of the outher surface of the dielectric coating a', the ratio E_z/H_ϕ becomes

$$\left(\frac{E_z}{H_\phi}\right)_{r=a'} = -j\sqrt{\mu_i/\epsilon_i}\,\frac{u_i}{k_i}\frac{J_0(u_i a')N_0(u_i a) - J_0(u_i a)N_0(u_i a')}{J_1(u_i a')N_0(u_i a) - J_0(u_i a)N_1(u_i a')}$$

where $u_i^2 = k_i^2 - \beta^2$; $k_i = \omega\sqrt{\epsilon_i \mu_i}$. The subscript i refers to the dielectric layer. The condition of wave propagation is that the phase velocity of the surface wave is slightly less than the velocity of the wave in free space. Consequently, Goubau also established that the dielectric layer should be thin compared to the wire radius and the combined wire plus dielectric radii should be smaller than the wavelength. The major contribution of Georg Goubau is that he experimentally demonstrated surface wave propagation [41, 63, 64].

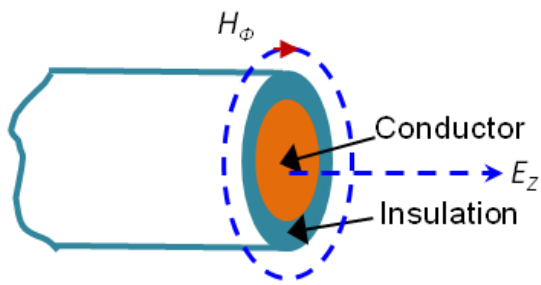

Figure 4.2.Graphical representation of a Goubau wire/line.

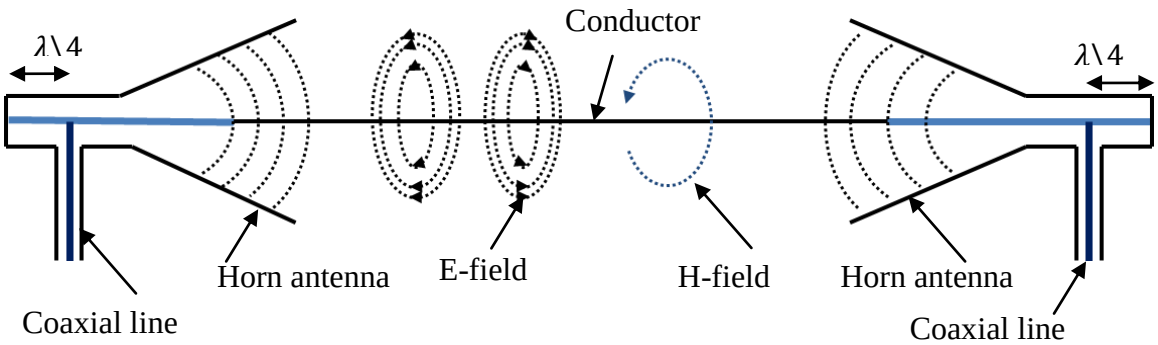

Figure 4.3.Launching surface waves on a direct connected wire and receiving them using horn antennas [41].

He designed conical shaped horn antennas as surface wave launchers and connected those to the wire as shown Fig. 4.3. The transmit horn was energized using a signal source as shown in Fig. 4.3. The opening of the horns was 33 cm and the measurement was done at 1600 MHz on a 0.2 cm diameter wire (#12 wire) with an enamel thickness of $5x10^{-3}$ cm ($\frac{\epsilon_i}{\epsilon} = 3;\ \tan\delta = 8 \times 10^{-3}$). The length of the wire was 120 ft and the calculated total loss was 2 dB. His objective was to design a high frequency low loss single conductor transmission line. The details of his experiments and analysis are summarized in [41].

4.3 ELMORE'S WORK

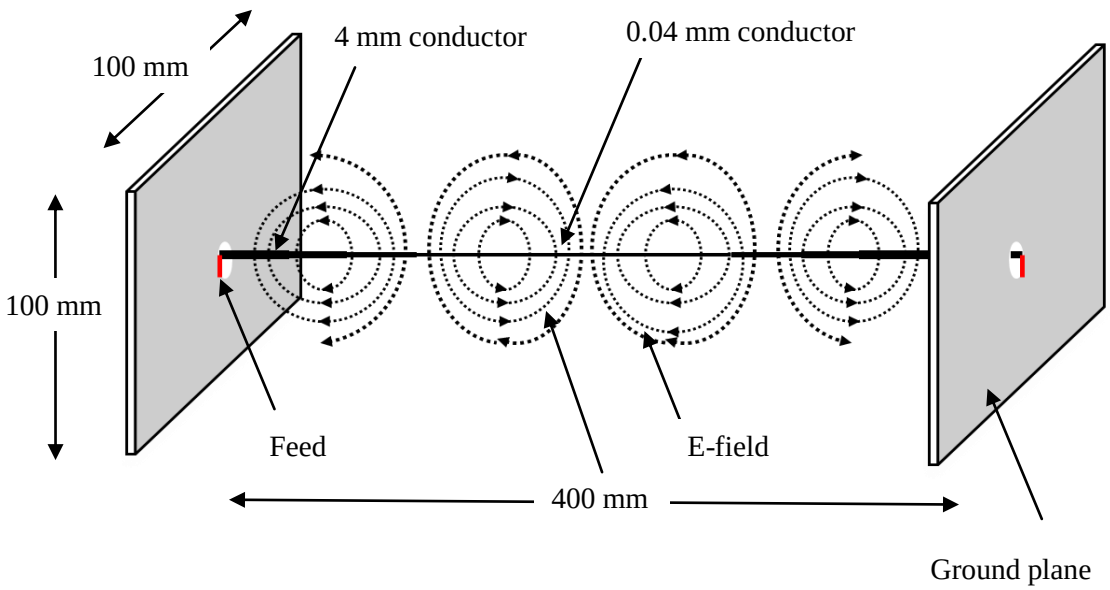

Figure 4.4. Glenn Elmore's TM wave surface wave simulation model

Elmore proposed the application of surface waves for possible Power Line Communication (PLC) [42, 65]. His simulation studies consisted of surface wave launch and propagation along the length of a wire as illustrated in Fig. 4.4. Port 1 was connected between a large ground plane and the wire and a propagating wave was excited. Port 2 represented the receiver where the signal was picked up between the large ground plane

and the wire. Thus both transmission and reception was achieved by physically connecting the source and the receiver to the actual transmission medium, the wire.

His experimental work is shown in Fig. 4.5 which shows a large slotted horn antenna attached to an overhead power line. Surface wave propagation was achieved at 2 GHz. Fig 4.6 shows the measured S_{21} response of a pair of launchers that were 18 m apart from each other and were placed on a #4 stranded copper power cable. The upper trace of Fig. 4.6 is the calculated GA_{max} presented by Elmore without considering the attenuation due to port mismatch. At 1900 MHz, the insertion loss is 7 dB and at a second resonance at 500 MHz, the insertaion loss is about 27 dB. He also showed that his designed conical horn launcher was able to transmit 100 MHz of data bandwidth at 2 GHz with a C/N limit of 30 dB. He suggested possible application of his system might be for "Smart Grid" data communciation for end users along with real time power management and billing.

Figure 4.5. Elmore designed slotted horn antenna directly connected with a bare aluminum power line cable reported in [65].

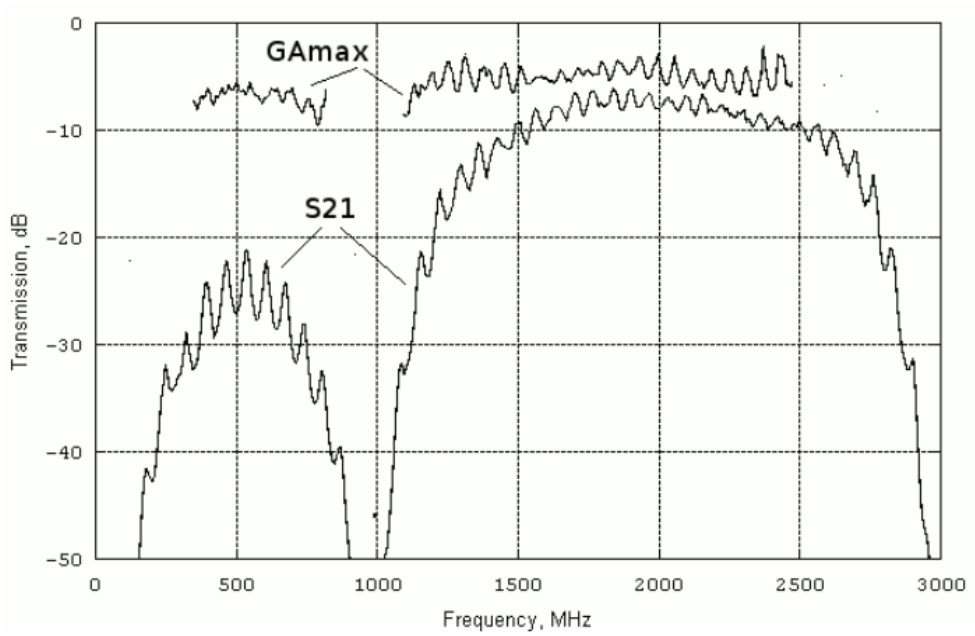

Figure 4.6.Elmore measurement results of GAmax and transmission performance S_{21} on a 18 m long and 4 mm diameter copper power line conductor [65].

The Goubau or Elmore type surface wave launch and propagation is intrusive because it requires the RF or microwave signal source and the receiver to be physically connected to the wire or conductor that will support the wave propagation. In practical application, a non-intrusive method of signal injection is greatly preferred. Secondly, the wave launchers reported in the literature are large multi-wavelength travelling wave type launchers that are not suitable for application in the VHF-UHF frequency range which is the frequency range we are interested to test them out for power cable fault detection and monitoring using both TDR and JTFDR.

CHAPTER 5

DESIGN AND APPLICATION OF SURFACE WAVE LAUNCHERSFOR NON-INTRUSIVE POWER LINE FAULT SENSING

Autonomous in-situ non-intrusive power line fault detection and monitoring is crucial to ensure the safety, security, and well-being of people, business, and infrastructure. Common causes of power cable failures can be as diverse as open circuit, short circuit, high impedance faults, tree (water tree and electrical tree) formation in the insulation [66-71], corona, and partial discharge [14, 30, 33-35, 37, 38]. Existing methods of cable diagnostics to detect these failures require loss or interruption of service while the system is being repaired. For example, consider the tanδ method of power cable diagnostics, which is used to determine the insulation degradation of a service aged power cable. The tanδ test is usually performed at a Very Low Frequency (VLF)-0.1Hz by de-energizing and isolating the cable [72]. When the measured tanδ exceeds a particular value set by the IEEE Standards [72], the cable is declared defective. Similarly in the offline partial discharge (PD) method of cable diagnostics, the reflection of PD pulses from the PD location of an offline cable is used along with Time Domain Reflectometry (TDR) [31, 73-75]. Although online PD has been reported [76], there the high frequency electromagnetic emissions due to PD are picked up by localized antenna coils, amplified, and then observed in a spectrum analyzer for further analysis. It is

apparent that existing cable diagnostic techniques are complicated, bulky and heavy and do not allow real-time monitoring.

This Chapter introduces a concept of non-intrusive real-time power cable fault monitoring using wireless sensors (Fig. 5.1). The key components of the sensor are identified as energy harvester, waveforms and algorithms, circuits and components, and surface wave launcher. In [77] we have already reported a miniature energy harvester that can harvest power from a power cable non-intrusively. In terms of waveforms and algorithms, we propose to use TDR and in terms of circuits and components, we propose to use either commercial off the shelf elements or develop them in the lab. The key contribution of this work is the design, development and application of a pair of subwavelength sized broadband surface wave launchers, a TDR pulse generator circuit and the validation that when these are used in conjunction with the other building blocks identified in Fig. 5.1 one can detect power cable faults.

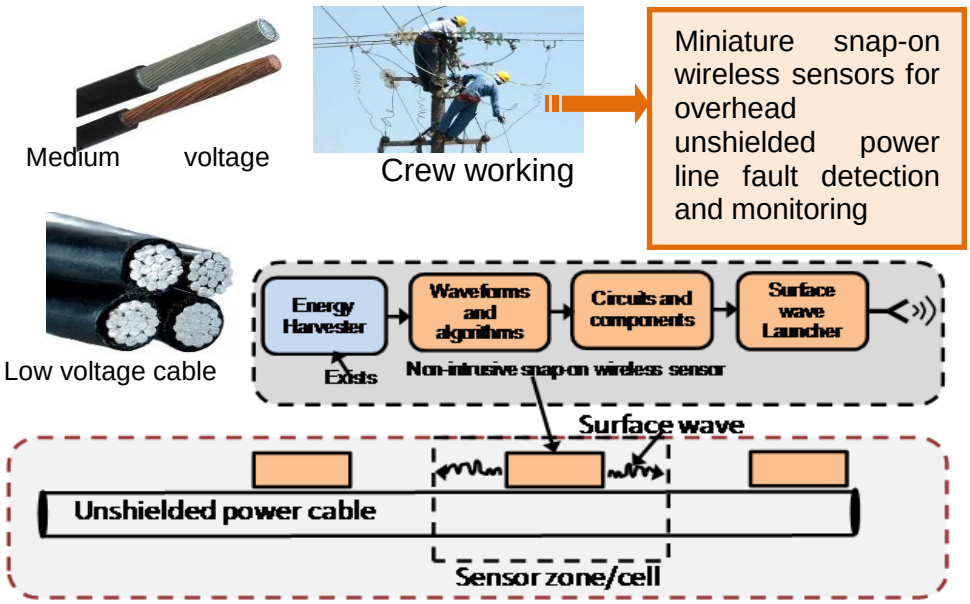

Figure 5.1. Examples of unshielded cables. Proposed non-intrusive wireless sensor block diagram. Schematic representation of sensor placement on cables.

Although studies of surface waves date back many years [40, 41, 63, 78] they have been recently revived to evaluate their potentials for data communication over power lines [65]. However, compared to the work described in [65] our research is fundamentally different since we propose to use surface waves as a sensing and diagnostic tool [15, 79], instead of its traditional application in communication. We propose to launch surface waves using distributed sensors (as shown in Fig. 5.1) and retrieve them using sensors to detect power cable faults. Once launched and during its travel if the wave experiences any fault that have a measurable impact on its propagation all or part of the wave is reflected. The reflected wave is then picked up by the wave launcher, and further processing then determines the location and extent of the damage.

In Section 5.1 the reflection and transmission properties of surface wave launchers are studied as function of frequency with launcher geometrical variables as the parameter. In Section 5.2, open circuit cable faults are detected using conformal surface wave (CSW) launchers and TDR. In Section 5.3, the design of a small pulse generator circuit is presented when operated in conjunction with a CSW launchers shows the efficacy of cable open circuit fault detection. This brings us one step closer to developing an actual sensing system without using large expensive pieces of equipment. In Section 5.4, TDR surface wave propagation velocity measurements are presented using surface wave launchers.

5.1 SURFACE WAVE LAUNCHERS AND THEIR TRANSMISSION PROPERTIES

5.1.1 WIRE AND WIDE MONOPOLE LAUNCHERS

As indicated, in this work the time domain reflectometry (TDR) technique is used along with a pair of surface wave launchers to detect power cable faults. An incident pulse travels down the length of a cable and then is reflected back from the fault location. By comparing the incident and reflected pulse waveforms we are able to detect and locate a fault. Typically in TDR, pulse durations are in the micro second range which requires that the surface wave launchers to be used should operate in the 50-500 MHz frequency range, have wide operating bandwidth and low loss. Since the non-intrusive sensors will be placed on power line cables the surface wave launchers also need to reside on the surface of the power cables. Previous surface wave launchers proposed by Goubau [41] and Elmore [65] are too large and are not of appropriate shape and weight to be accommodated on power cables. This led us to explore electrically small yet broadband non-travelling wave type antennas. These broadband antennas will work as surface wave launchers.

As a starting point we considered experimenting with monopole antennas. Examples of monopoles used are shown in Fig. 5.2. A pair of wire monopoles was developed first. Subsequently a pair of wide monopoles was also developed. The wire monopole pairs were designed for operation at 250 MHz in free-space. Each wire monopole was constructed from a 300 mm long wire and was excited using a 50 Ω SMA connector from the bottom of a 415 mm by 260 mm metal ground plane. A small opening was created at the center of the ground plane through which the inner conductor of the

SMA connector was inserted and connected to the wire monopole. The ground plane was soldered to the ground connection of the SMA connector.

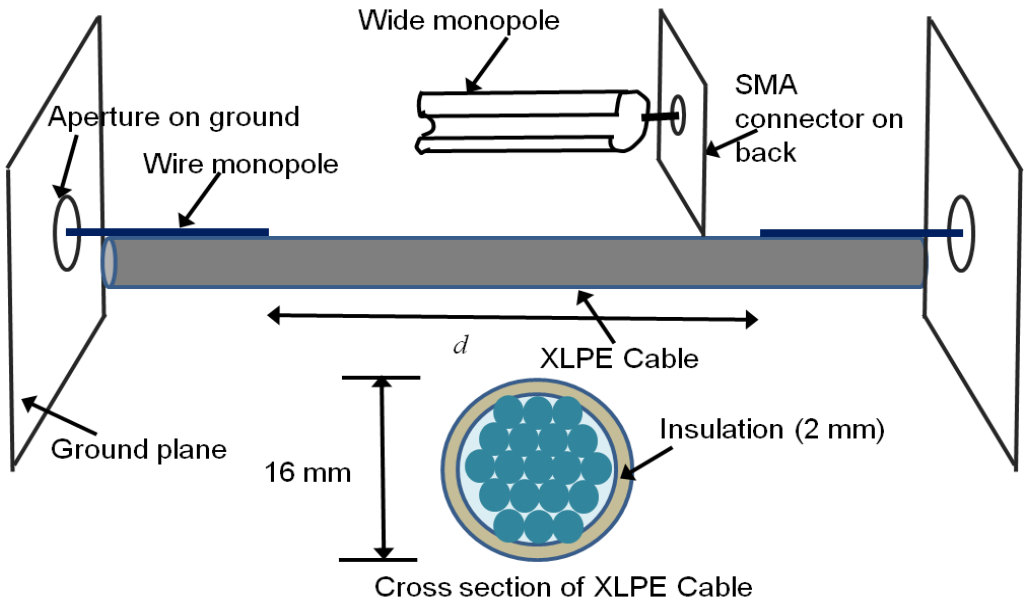

Figure 5.2. Experimental setup of monopole surface wave launchers on XLPE cable: cable length=2.14m.

To investigate the feasibility of surface wave propagation using monopole launchers unshielded XLPE power cables were procured and used. The diameter of the sample XLPE cables was 16 mm including the insulation. The insulation thickness was 2 mm. The diameter of the wide monopole was slightly larger than 16 mm. A narrow slit was cut in the wide monopole for easy wrapping on the power cable.

Since the primary objective of this work is to launch relatively narrow time duration (hence broadband) pulses along the power cable and probe the return pulse two aspects are critical, e.g. launcher's bandwidth (S_{11} and S_{21}) and overall signal transmission loss.

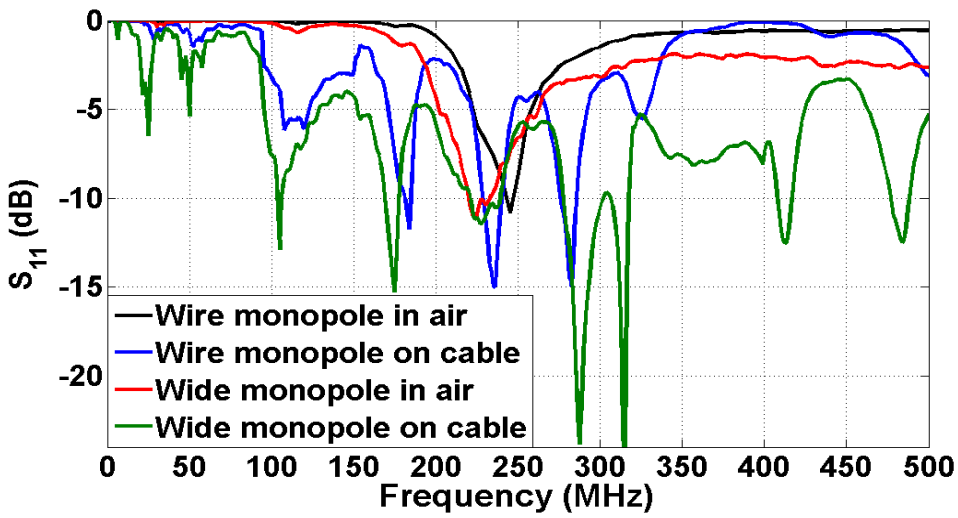

Figure 5.3. Measured S_{11} vs frequency of wire and wide monopole launchers in the presence and absence of a 2.14m long XLPE unshielded power cable

Thus to assess the bandwidth input S_{11} of the wire and wide monopoles were first measured in air without any XLPE power cable to confirm launcher operation at around 250 MHz. Next the same experiments were repeated when a pair of launchers was placed at two ends of a 2.14 m long power cable (Fig. 5.2). These results are shown in Fig. 5.3 for both the wire and wide monopoles and both in the presence and absence of the power cable. It was observed that when the monopoles were in air the bandwidth was narrow. When the monopoles were placed on the XLPE cable insulation operation showed clear improvement in bandwidth. This is in line with the hypotheses that surface waves are propagating along the length of the cable resulting in a forward traveling wave along the length of the cable, hence less reflection and wider S_{11} bandwidth. Although S_{11} magnitude of -10 dB or lower is beneficial that may not be achievable with these resonant monopole type launchers. Thus unlike traditional communication antennas here we will use a more relaxed S_{11} limit to define bandwidth. Assuming S_{11}<-5 dB the bandwidth of either launcher in air without the XLPE cables is very narrow. A clear potential for wide bandwidth is observed when the wire monopole is brought close to the power cable. The

bandwidth is 75-425 MHz when the wide monopole is brought close to the power cable.

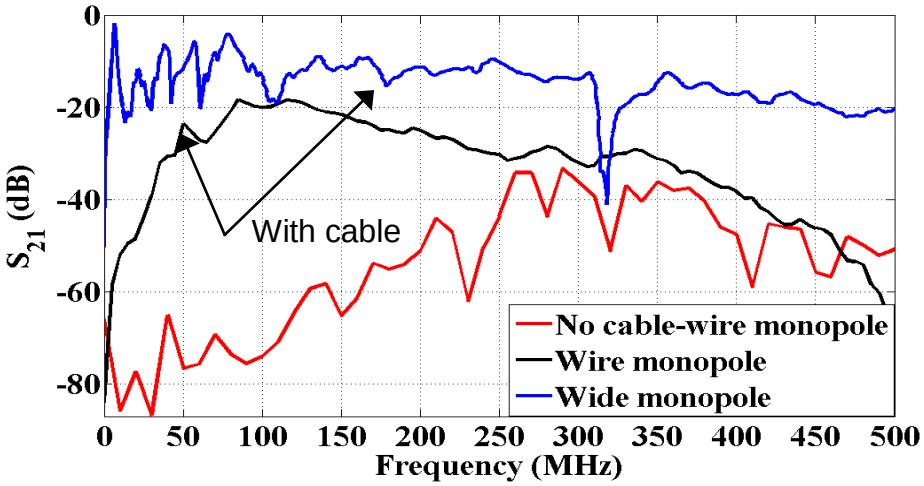

Figure 5.4. Measured transmission between monopoles with and without cable.

In Fig. 5.4 we show the measured S_{21}(dB) or transmission data between two launchers at a distance of 2.14m. The two ports of a network analyzer were connected to two identical monopole launchers. Measurement with and without the XLPE cable between two wire monopoles are shown (black and red traces respectively). Clearly without the presence of the XLPE cable transmission is very weak. Transmission loss is between 45-70 dB within the frequency range of 50-200 MHz. In contrast, transmission loss is between 20-30 dB within the frequency range of 50-350 MHz when the XLPE cable is present. When the same experiment was repeated with two wide monopoles transmission improved significantly (Fig. 5.4) both in terms of signal strength and bandwidth. Similar results were obtained with other lengths of cables.

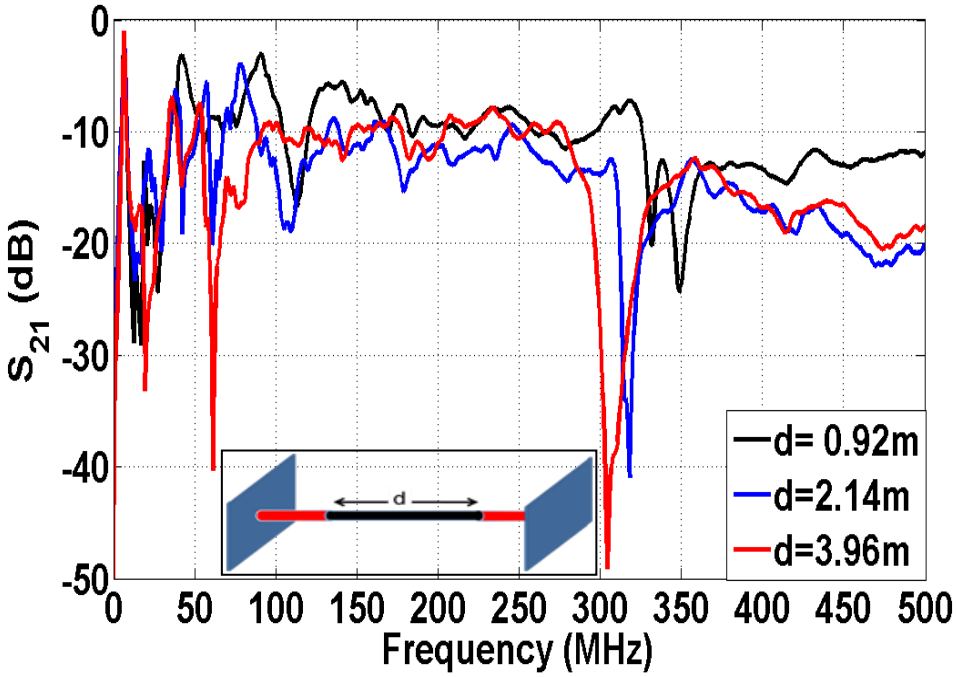

Figure 5.5. Transmission response of the wide monopoles.

Fig. 5.5 shows the measured transmission data between two wide monopole antennas when separated by different lengths of XLPE cables. The cable length varies from 0.92 m to 2.14 m to 3.96 m. As apparent, there is a transmission dip near 60 MHz. For a frequency range of almost 80-300 MHz transmission is nearly flat with frequency. Clearly shorter lengths will allow better transmission and ensure that there are no significant transmission dips between the individual sensor nodes. For example, for 0.92 m cable length the worst case transmission dip is about -25 dB. But for 2.14 m and 3.96 m cables the worst case transmission dips are -40 and -50 dB respectively.

Also note that the usable transmission bandwidth within a specific transmission loss decreases as the cable length between individual sensor nodes increases. This means if an ultra wideband pulse is to be transmitted the launcher has to be carefully designed

and developed and also sensor node density versus signal transmission loss has to be carefully evaluated.

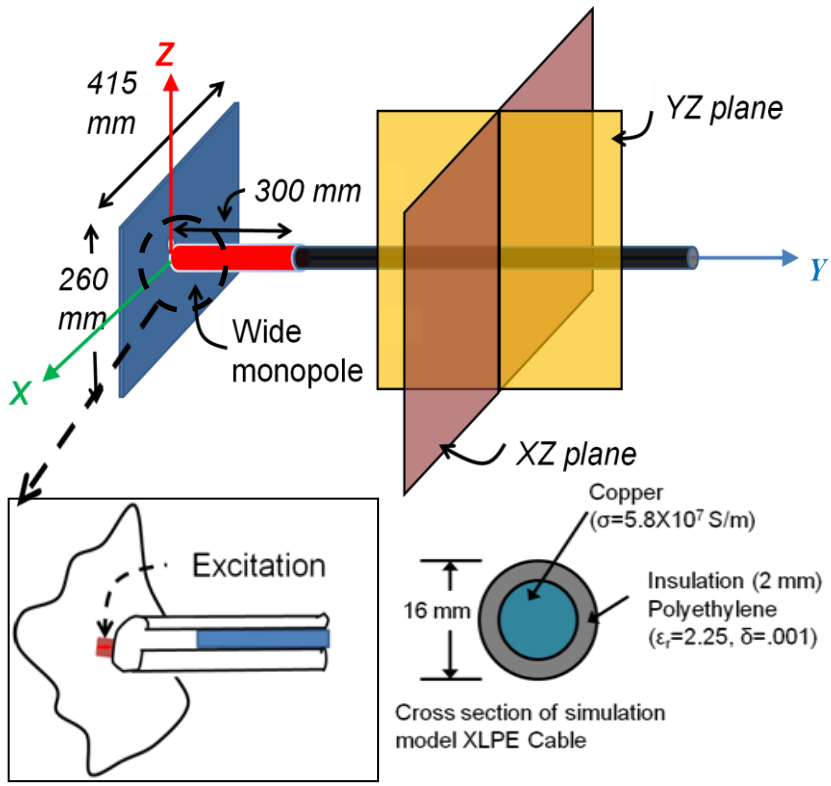

Figure 5.6. HFSS model to simulate electric and magnetic fields.

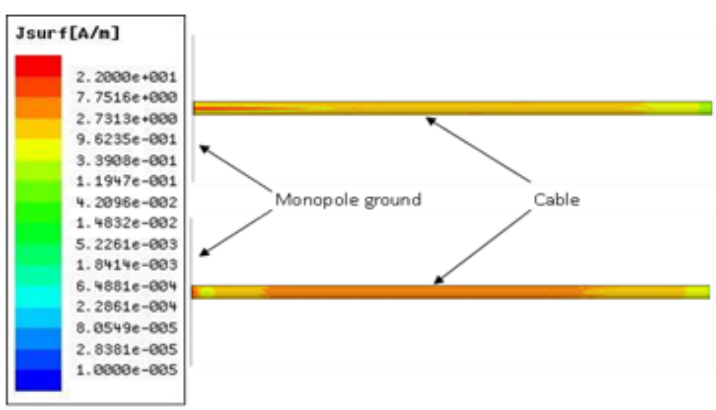

Figure 5.7. Comparison of simulated surface currents between the wire and wide monopoles in the presence of the XLPE cable [79].

Since the cable does not have any other separate conductor nearby to allow a potential difference the propagating mode is a non-TEM (transverse electromagnetic) mode. To confirm this observation simulation models consisting of both the wire and wide monopoles were developed using HFSS [80]. In each model an 800 mm long XLPE cable was excited using a monopole at one end. Thus in one model the launcher was a wire monopole while in another model the launcher was a wide monopole.

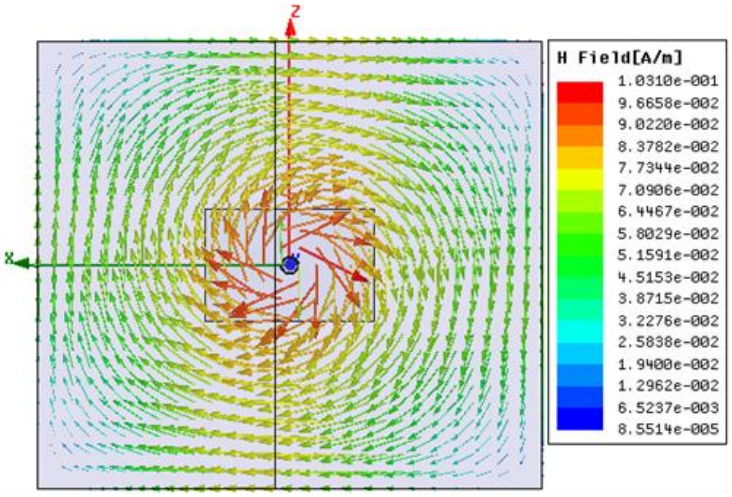

(a)

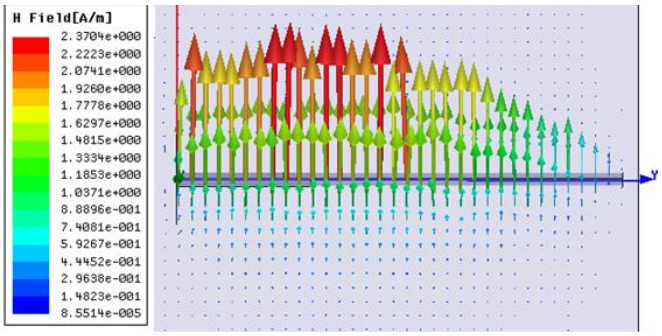

(b)

Figure 5.8. Computed H-field distribution along the cable (a) XZ plane and (b) YZ plane [79].

A schematic of the HFSS model consisting of the wide monopole is shown in Fig. 5.6. Simulated surface current distributions on the XLPE cable due to the wire and the wide

monopoles are shown in Fig. 5.7. The top shows the current distribution due to the wire monopole while the bottom shows the current due to the wide monopole. It is clear that the wide monopole can create a more uniform current on the conductor of the XLPE cable which is distributed over the entire length of the cable. This corroborates our earlier observations that the wide monopole is low loss and has a wider transmission bandwidth than the wire monopole.

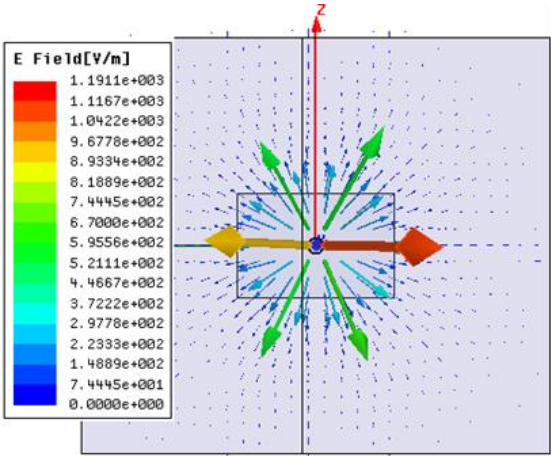

(a)

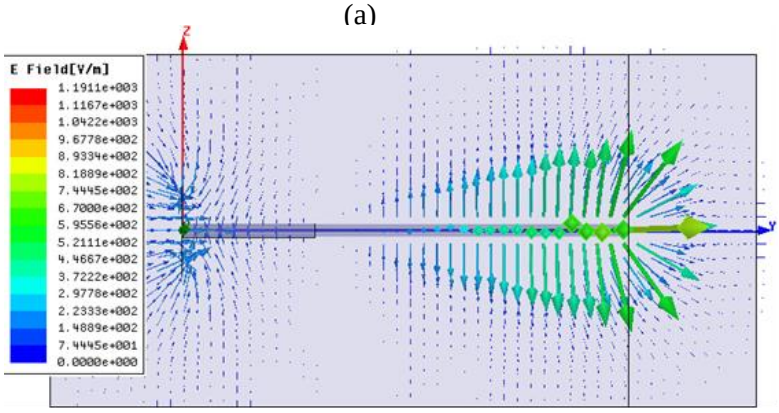

(b)

Figure 5.9. Electric field (E) distribution in (a) XZ, and (b) YZ plane [79].

Similarly simulated magnetic field distributions are shown in Figs. 5.9 and 5.10 for a wide monopole surface wave launcher. Fig. 5.8 shows the magnetic fields in the

XZ and YZ planes. Here XZ is the plane normal to the axis of the cable and YZ is the plane parallel to the axis of the cable as shown in Fig. 5.6. We observe that the H field has no longitudinal component; all field vectors are in the transverse direction to the cable's axis. Figs. 5.9(a) and (b) show the electric fields in the XZ and YZ planes.

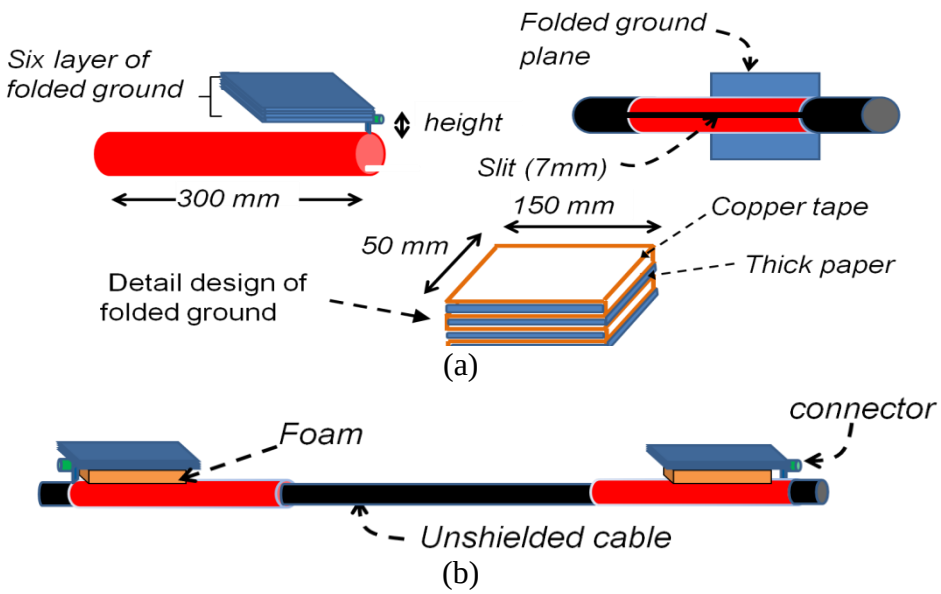

Figure 5.10. Proposed conformal surface wave launcher; (a) 3D view and bottom view, (b) installed on an unshielded power cable. The total ground plane dimension is 300 mm by 150 mm

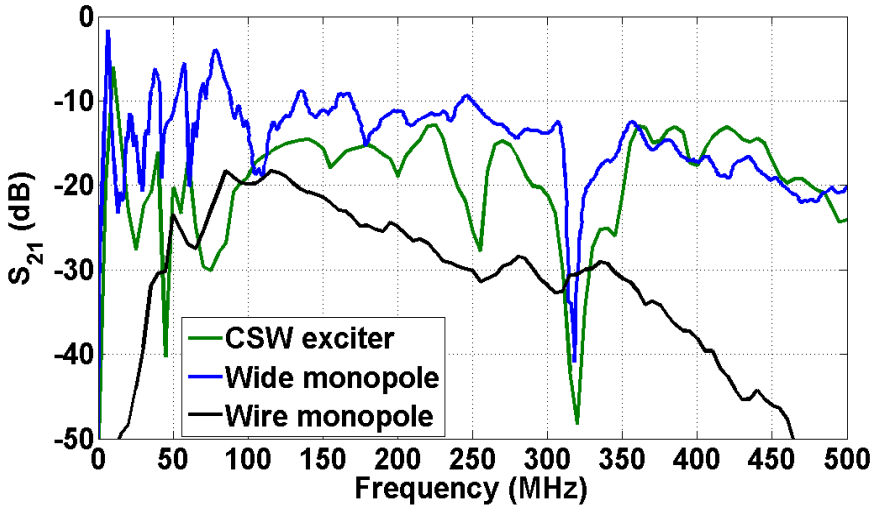

Figure 5.11. Transmission performance comparison for a pair of CSW launchers, wire monopole launchers and wide monopole launchers when placed on an XLPE cable of length 2.14 m.

Electric fields have both transverse and longitudinal components. Thus clearly the two monopole system on the cable supports TM mode surface wave propagation.

5.1.2 CONFORMAL SURFACE WAVE LAUNCHERS

The wire and wide monopole launchers designed and studied before are not conformal due to the metallic ground plane that is orthogonal to the power cable. This led us to consider developing a surface wave launcher which is conformal and can be placed on a plane parallel to the plane of a power cable. The primary idea was to use a ground plane that is not in the shape and size that was used for the wire and wide monopoles. Instead the idea of a folded ground plane was considered. Thus the new launcher named conformal surface wave (CSW) launcher consists of a wide monopole and a ground plane that is parallel to the power cable. In order to create more surface area for the ground plane the ground plane was folded multiple times. Between each fold a thin insulating layer was placed. This structure resembles an Inverted L Antenna (ILA). An ILA is a monopole antenna with lower radiation resistance, narrower bandwidth, and modified radiation pattern compared to a wire monopole antenna [81]. Without additional matching an ILA is not an efficient far field antenna [82]. However far field performance is not our concern as the surface wave launcher is not a far field device. The folded ground plane occupies much less space but has about the same area as that of the unfolded ground plane.

A comparison between the transmission between a pair of wire monopoles, wide monopoles, and CSW launchers when each pair was placed against a 2.14 m long XLPE cable are shown in Fig. 5.11. Clearly the wide and the CSW monopole pairs both perform better than the wire monopole pair. The usable bandwidth of the CSW monopole is

narrower than the wide monopole. The transmission loss of the CSW monopole is also higher than the wide monopole. Both of these clearly indicate the limitations of miniaturization. Although the folded ground plane seems to offer performance it is a worse alternative than the wide monopole with the orthogonal ground plane. Nevertheless, because of its small size and conformal nature it may be more amenable for actual use on a power cable. Undoubtedly best bandwidth and signal transmission can be obtained if travelling wave type surface wave launchers can be developed and used. They will be multiple wavelengths in size, heavy and may not be necessary for power system application. Thus future applications will dictate what type of bandwidths will be needed and what should be the density of the sensor nodes and then based on these data one may proceed to design and develop optimum size surface wave launchers.

Transmission performance was also measured by varying the separation between the CSW launchers when placed against an XLPE cable. The prototype CSW launcher had monopole length of 300 mm. The folded ground plane size was 300 mm by 150 mm. The ground plane was at a height of 5 mm from the monopole. Fig. 5.12 shows the transmission performance for separations of 0.92 m, 2.14 m and 3.96 m.

It is observed that transmission does not vary significantly with the change in separation. For all three cases, good transmission (transmission <−20 dB) was observed between 95 MHz to 200 MHz. However, the bandwidth found with the CSW launchers is narrower (105 MHz) than the bandwidth (280 MHz) found with the wide monopoles. Also the CSW launchers had a reduced sized ground plane 300 mm × 150 mm compared to the 415 mm × 260 mm ground plane for the wide monopole.

The transmission between a pair of CSW launchers when placed against a 2.14 m XLPE cable was also measured by varying the ground plane height. The ground plane height was varied as 1 mm, 5 mm, 10 mm and 20 mm. For ground plane heights of 5 mm, 10 mm and 20 mm there were no significant effect on the transmission (see Fig. 5.13). But transmission degraded significantly as the ground plane height was reduced to 1 mm. Experiments were also performed as function of ground plane sizes, e.g. 300 mm x 225 mm, 300 mm x 150 mm, 150 mm x 150 mm and 150 mm x 75 mm. Fig. 5.15 shows these results. For the 300 mm x 225 mm ground, the ¬20 dB transmission band extends from 85-265 MHz. For the 300 mm x 150 mm ground, there are two transmission bands, 90-200 MHz and 365-395 MHz. For the 150 mm x 150 mm ground there are also two transmission bands 90 to 115 MHz and 360-550 MHz. For The transmission bands for the 150 mm x 75 mm ground are from 105 to 130 MHz and from 380 to 525 MHz. Thus it is clear that increasing the ground plane size will increase the transmission bandwidth of the CSW launcher.

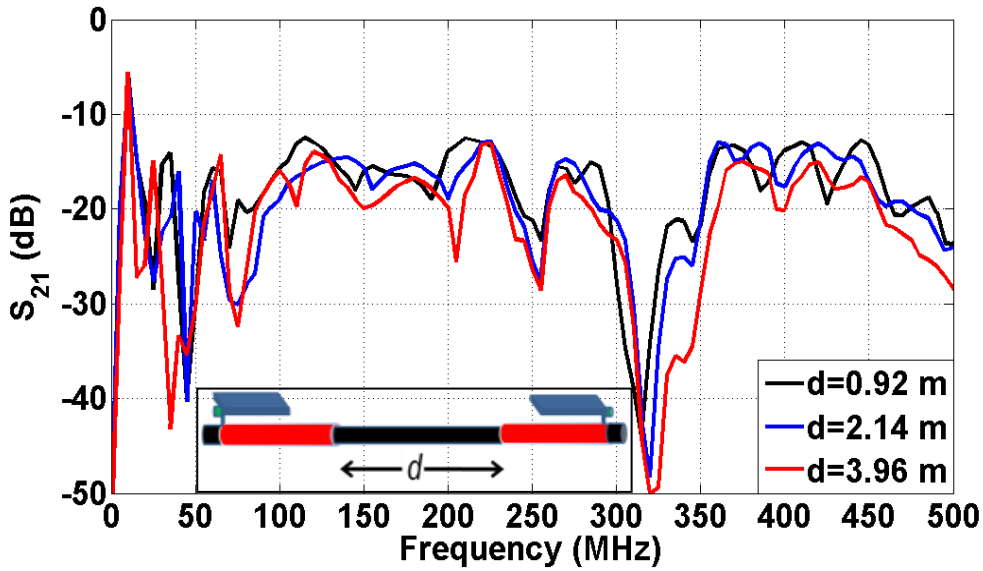

Figure 5.12. Transmission between a pair CSW launchers when placed against an XLPE power cable.

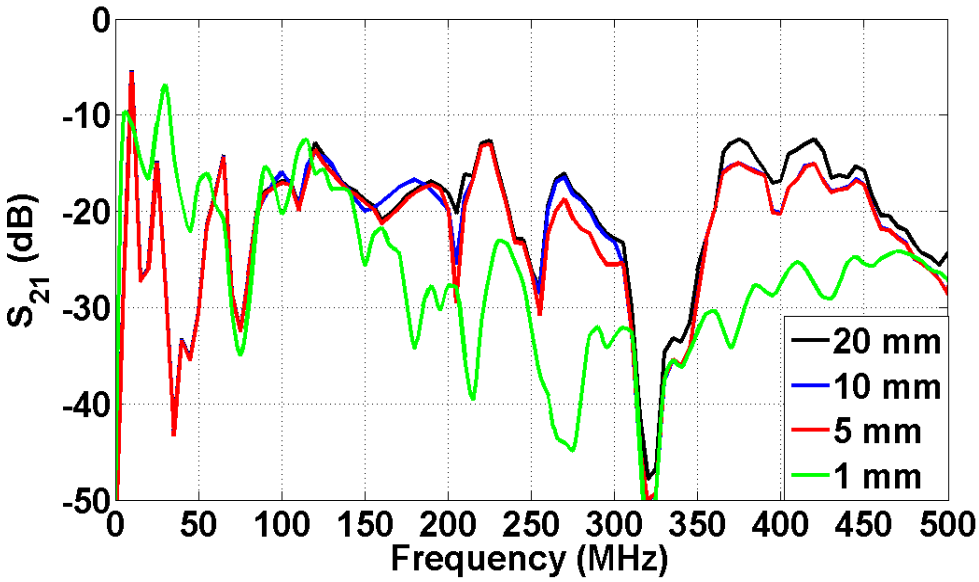

Figure 5.13. Effect of ground height on the transmission between a pair of CSW launchers [79].

5.2 TDR EXPERIMENTS USING CSW LAUNCHER AND VNA

Next we decided to conduct experiments to detect open circuit faults in power cables. Specific lengths of XLPE cables were used for this purpose. Based on our previous experiments a single CSW launcher was selected and placed at one end of an XLPE cable.

An open circuit fault was created at four arbitrary locations i.e., at 2.14 m, 4.61 m, 9.01 m and 15.14 m away from the CSW launcher.

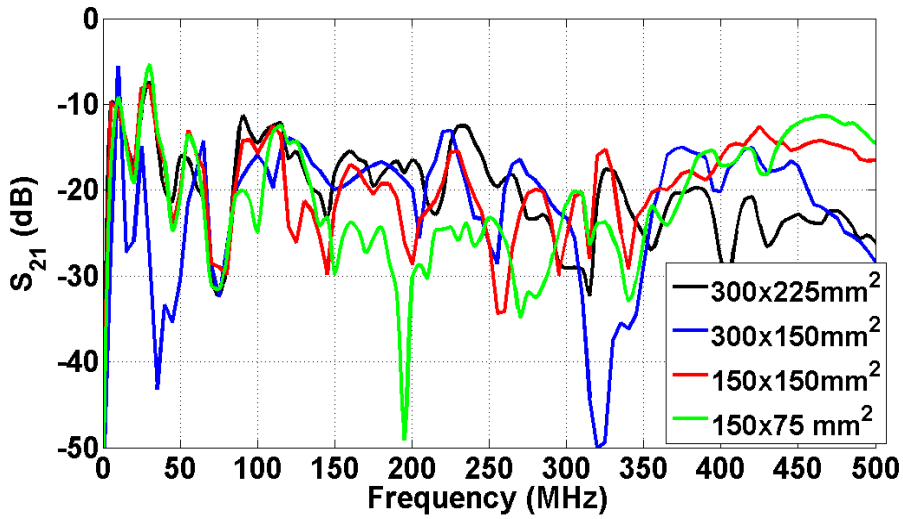

Figure 5.14. Effect of ground plane size on transmission for CSW launchers [79].

The CSW launcher was connected to a vector network analyzer (VNA). The VNA provided a step input signal to excite the CSW launcher. The step signal propagated along the power cable and was reflected back from the open fault and was returned to the VNA through the CSW launcher. Fig. 5.15 shows the reflection from the fault plotted against the length of the cable. The reflections were normalized with respect to the maximum value. Maximum reflection occurs from the open circuit fault. So the fault location can be found by locating the peak point of the reflection curve. The detected fault locations are marked as circles on the curves. The deviations of the detected fault locations from the actual fault locations are shown in Table 5.1. It was found that all the fault locations detected using this technique were within 8% of the actual fault locations.

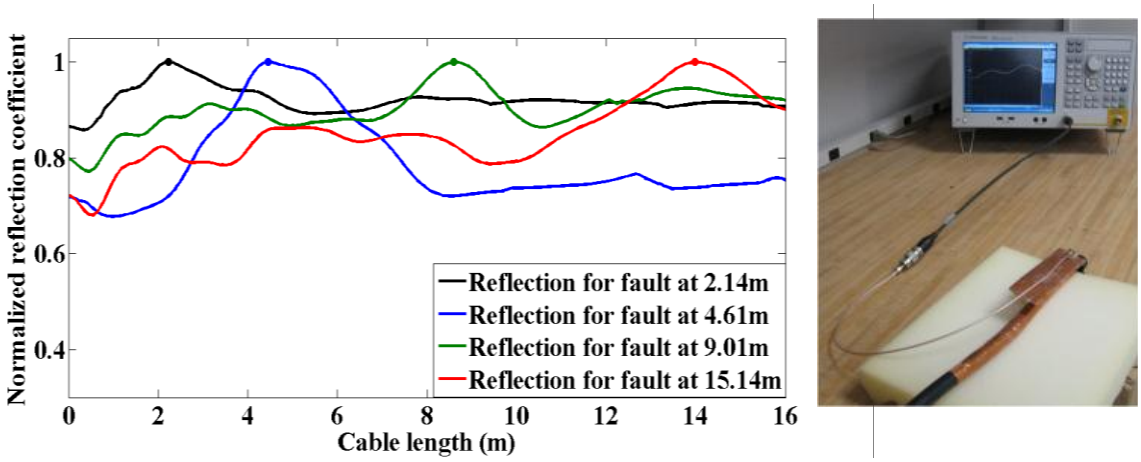

Figure 5.15. Results of TDR experiments using a single CSW launcher against four XLPE cables open circuited at the end [79].

The possible causes of difference of the measured locations from the actual fault locations include VNA DC value approximation, dispersion, and uncertainty in terms of the phase velocity of the electromagnetic waves. The VNA extrapolates the low frequency response, especially the DC value, from the higher frequency responses [83]. Dispersion causes various frequency components of a broadband signal to travel with different phase velocities and arrive at different times at the receiver [84] which causes signal distortion. Also we assumed that the dielectric constant of the insulation all along the cable and hence the phase velocity is constant which might not be the actual case. All of these factors could have contributed to the deviations.

Table 5.1:Location of open circuit measured using VNA And CSW Launcher

Actual cable length (m)	Measured cable length (m)	Error
2.14	2.23	4.2%
4.61	4.45	3.4%
9.01	8.596	4.6%
15.14	13.99	7.6%

5.3 CIRCUIT EXPERIMENT USING CSW LAUNCHERS

The ultimate goal of a non-intrusive wireless sensing system is to have small localized sensors with their on-board launching and processing capabilities. Thus it is important that the waveform to be used for fault detection be created using a small component that contains the necessary circuit. In TDR the essential waveform is a narrow pulse and thus developing and using a pulse generator circuit is important.

5.3.1 PULSE GENERATOR CIRCUIT

Rectangular pulse circuit is simple to construct than other kinds of pulses. A rectangular pulse of duration τ

$$p(t) = \begin{cases} x = 1;\ 0 < t < \tau \\ 0,\ \text{elsewhere} \end{cases} \tag{5.1}$$

The energy spectrum is

$$|P(f)|^2 = \left(\frac{\sin(\pi f \tau)}{\pi f}\right)^2 = T^2 \text{sinc}^2(f) \tag{5.2}$$

Ultra narrow pulses (i.e., 4 ns) is not easy to generate without complicated signal processing. Therefore, we exploited an existing design, proposed in a Linear Technology Corporation Technical Note [85]. We used LT1721 as a surface mount comparator and 4AHC08 as an And gate. To model and simulate the performance of the circuit we used LTSpice. As because all values of the surface mount resistors were not available, it was found that the pulse width was 4.5 ns. The simulated output waveform is shown in Fig. 5.16.

The measured output waveform of the pulse generator circuit is shown in Fig. 5.16. The photograph of circuit is shown as an inset in Fig. 5.17.

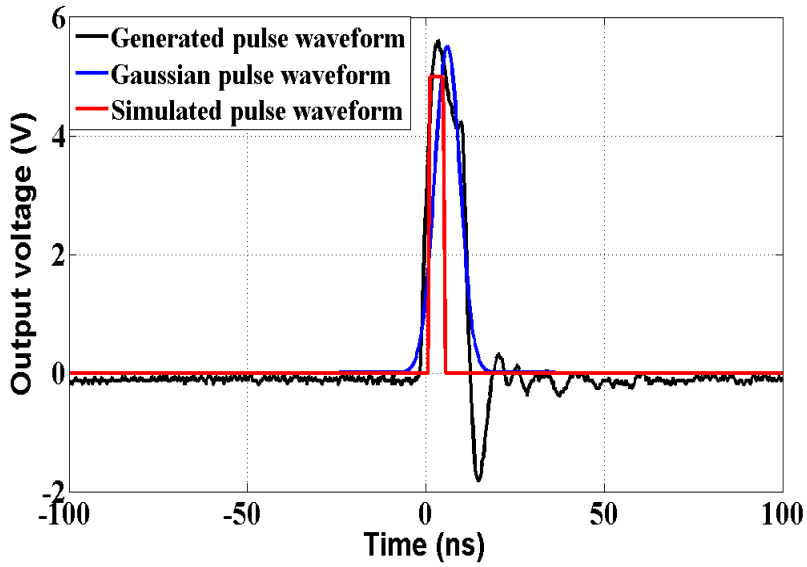

Figure 5.16. The comparison of the generated pulse with a Gaussian pulse.

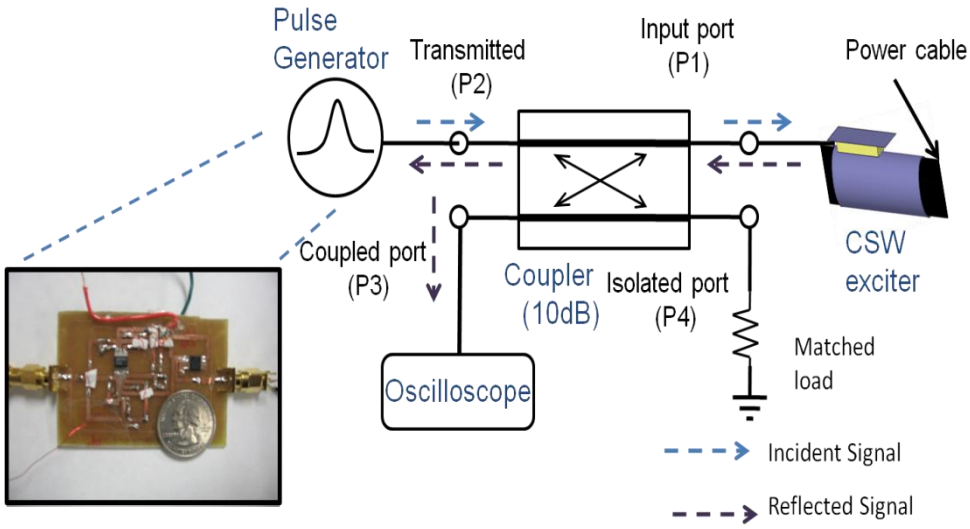

Figure 5.17. Schematic diagram of the experimental set-up to perform TDR open circuit fault detection in XLPE cables using the pulse generator circuit and the CSW launcher.

The output is similar to a Gaussian pulse than a rectangular pulse. This occurs due to the slew rate limitations of the components and the time spent between the on and off states. The Gaussian pulse can be expressed as

$$V_g(t) = V_0 \exp(-\frac{t^2}{2\,\sigma^2}) \tag{5.3}$$

where, V_0=5.5V, σ =2.5725e − 9s and the pulse width (full width at half maximum or FWHM) is 2.36σ =6.07e − 9s ≈ 6ns . The first ringing voltage is 1.75V which is 31% of the peak amplitude and the other ringing levels with regard to the peak amplitude is 5.42%.

5.3.2 EXPERIMENTS WITH CSW LAUNCHER AND PULSE GENERATOR CIRCUIT

To detect open circuit faults as before we used the output pulse of the pulse generating circuit as our source (reference) signal. The reference signal was then connected to the output of a surface mount 10 dB coupler (see Fig. 5.17) which after subsequently passing through the coupler's thru port was injected by the CSW launcher into the power cable under test. The open circuit present at the distal end of the power cable (towards the right end of the launcher in Fig. 5.17) resulted in a reflected pulse which was then picked up by the surface wave launcher which then passed to the coupled port of the coupler. This port of the coupler already had a part of the reference signal from before. The coupled port was connected to a digital oscilloscope. We used 600V unshielded XLPE cables of lengths 4.26 and 9.45 m. In Fig. 5.18 normalized amplitudes of the reflected signals vs time are shown for the two cables. Peaks near 0 ns represent the closest open circuit, beginning of cable and hence are not of interest for these tests.

Using the pulse generating circuit and the wave launcher we can easily detect the presence of the open circuit at 4.3 m distance. As the distance increases to 9.4m ambiguity arises because of signal attenuation. Table 5.2, shows the comparison of the actual length and the measured cable length, the highest percentage of error is 8.4% for 9.45 m without using any kind of filter or algorithm.

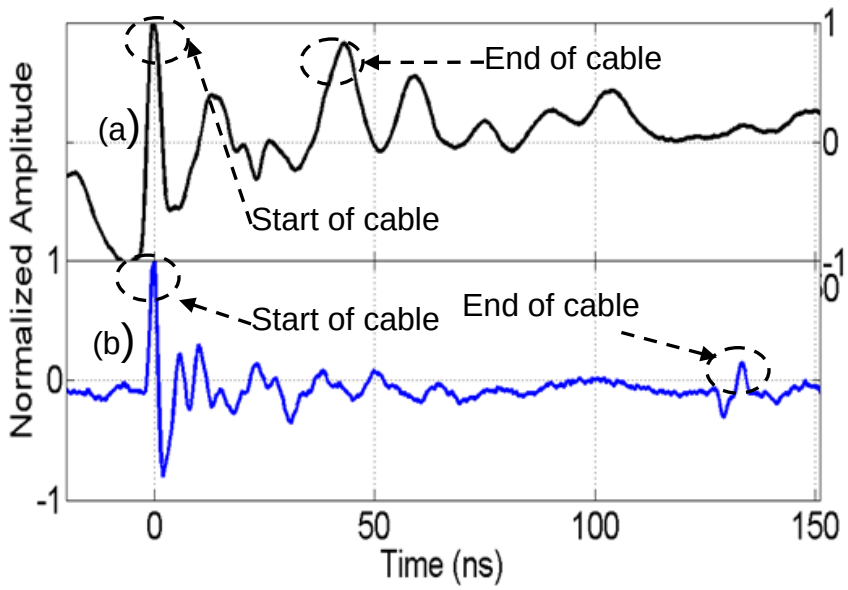

Figure 5.18. Normalized amplitude of the return signal for XLPE cable lengths of (a) 4.26 m (b) 9.45 m. Experimental results corresponding to the setup shown in Fig. 5.18.

Table 5.2: Location of open circuit measured using circuit and CSW launcher

Actual cable length (m)	Measured cable length (m)	Error
2.14	2.23	6.1%
4.26	4.32	1.4%
9.45	10.25	8.4%

5.4 SURFACE WAVE PROPAGATION VELOCITYMEASUREMENTS IN UNSHIELDED XLPE POWER CABLES

In this work we used wide monopole launchers mounted on 415 mm by 260 mm aluminum ground planes. Each wide monopole was fabricated using flexible copper tape forming a 16 mm diameter cylinder with a 2 mm slit. Each monopole launcher was then wrapped around various length unshielded power cables and excited using an incident 1V peak Gaussian pulse from a signal generator (Tektronix AWG 610). The incident signal was fed to a T-junction. Output1 of the T-junction was fed to the monopole launcher while Output2 of the T-junction was kept as a reference signal. The pulse waveform injected into the launcher propagated as a surface wave along the power cable and was reflected once it experienced an open circuit. Unshielded XLPE cables (16 mm diameter, 2 mm thick insulation) of length 6 ft, 14.58 ft and 22.92 ft were used. Each cable was hung from the ceiling using nylon ropes and cardboard tubes. Wood posts were also used at the end and middle to avoid interactions of the wave with the floor below. Photograph of the experimental setup is shown in Fig. 5.19. The return pulse waveforms for different lengths of cable and different input pulse widths are shown in Fig. 5.20. The velocity of surface wave can be calculated using the equation $V_p = \frac{2l}{t_d}$. Where l is the length of the cable segment and t_d is the time delay between reflected signal due to the surface wave exciter and the reflected signal from the open end of the corresponding cable segment. The field components of an un-attenuated surface wave on a metallic wire with circular cross section with finite conductivity can be expressed as [41]

The radial component of the electric field is

$$E_r = A\frac{\gamma}{u}H_1^{(1)}(jur)e^{j\omega t-\gamma z} \tag{5.4}$$

The longitudinal component of the electric field is

$$E_z = A\,H_0^{(1)}(jur)e^{j\omega t-\gamma z} \tag{5.5}$$

The magnetic field component in a plane transverse to the conductor is

$$H_\phi = A\,k^2/\omega\mu u H_1^{(1)}(jur)e^{j\omega t-\gamma z} \tag{5.6}$$

Here, z indicates the distance along the cable and r indicates the distance from the wire center. H_0andH_1 are Hankel functions of order 0 and 1, γ is the propagation constant which is equal to $(\alpha + j\beta)$ and u is the radial decay function defined by the equation

$$u^2 = \beta^2 - k^2 \tag{5.7}$$

$\beta = 2\pi/\lambda_g$, where λ_g= wavelength of the surface wave, $k = 2\pi/\lambda$; λ=free space wavelength. Let, a be the radius of the conductor and a' be the radius of the outer surface of the cable with insulation layer. Dielectric layer thickness is very small compared to the wavelength of the transmitted signal.

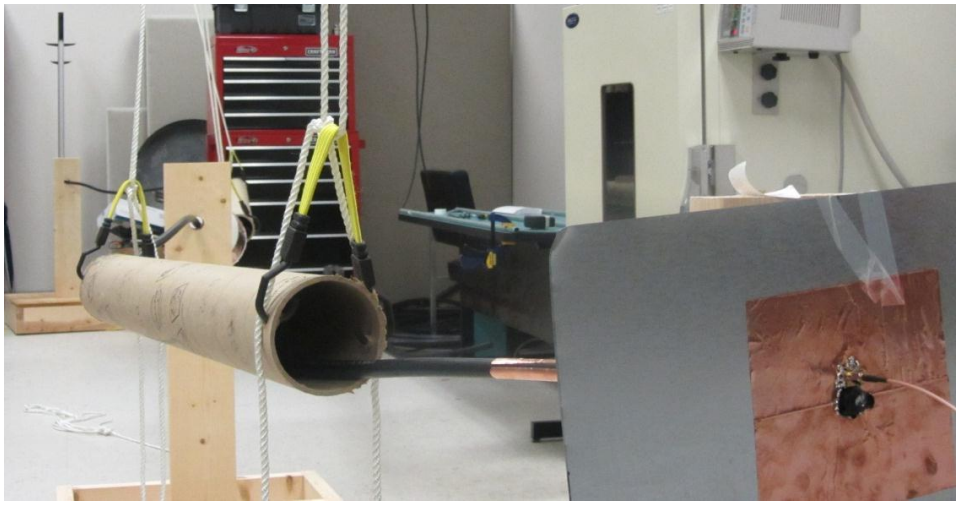

Figure 5.19. Experimental setup to determine the surface wave propagation velocity in an unshielded XLPE cable.

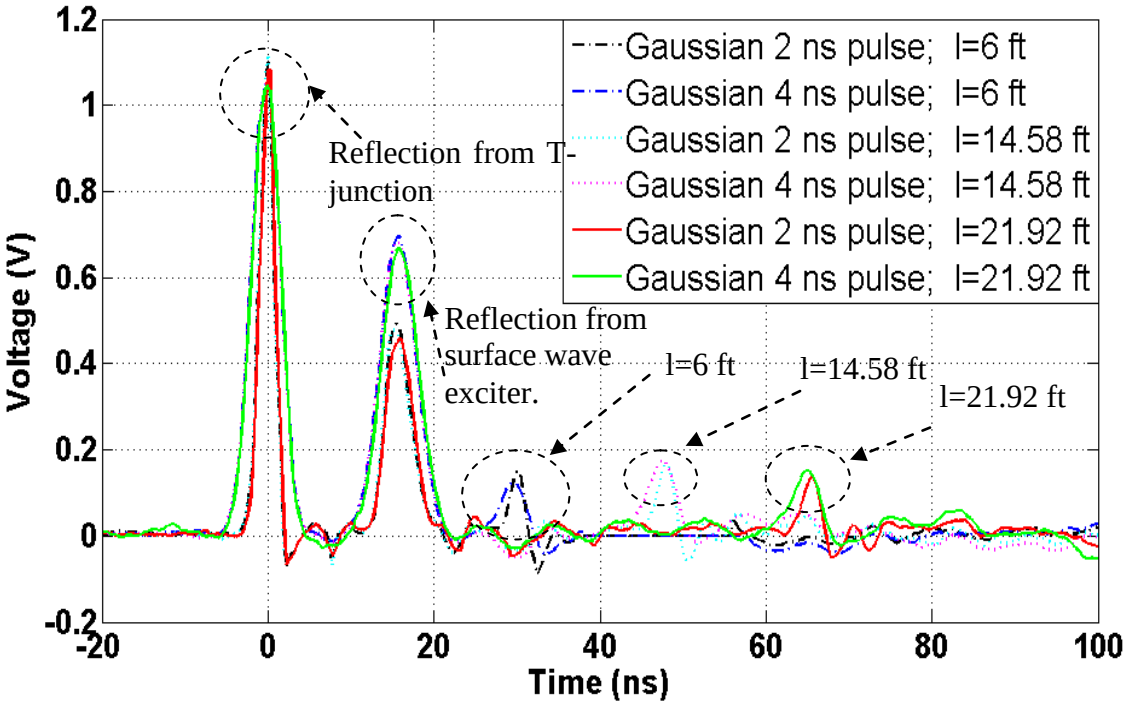

Figure 5.20: Return signal observed in the oscilloscope for different XLPE cable. lengths and different pulse widths.

Goubau showed that the transverse magnetic field is continuous across the wire boundary. Thus, equating the surface impedance on the dielectric coating and the surface impedance in air for a radius of a'someone can evaluate u from equation (5.8)

$$\left(\frac{a'}{a}\right)^2 \ln\frac{a'}{a} = \left(\frac{\epsilon_d}{\epsilon_d - \epsilon}\right)\left(\frac{\lambda}{a}\right)^2 \left\{-\left(\frac{ua'}{2\pi}\right)^2 \ln(0.89ua')\right\} \tag{5.8}$$

Then one can calculate the phase velocity of the surface wave for different frequencies. The calculated phase velocity is 2.976×10^8 m/s which is constant with respect to frequency.

The surface wave launch and propagation of broadband Gaussian pulses (2 ns and 4 ns durations) are investigated with the help of broadband cylindrical monopole launchers, a T-junction, and oscilloscope. Experimentally measured propagation velocities (about2.8×10^8 m/s)of surface waves on unshielded power cables are presented. This value is close to the free-space velocity of the wave. Experimentally measured velocities of the surface wave for the three different lengths of the cable are listed in Table 5.3.

Table 5.3: Measured velocity of surface wave

Cable Length (ft)	Time (ns)	Velocity (m/s)
6	14	2.7×10^8
14.58	32.25	2.779×10^8
21.92	49.75	2.8×10^8

A new concept to detect power cable faults is proposed where distributed self-sustaining sensor modules inject propagating surface waves on the power line conductors. Given that the surface waves are launched at frequencies much higher than power line frequencies the chances of interference are minimal. Several types of non travelling wave type yet broadband wave launchers were developed and tested with various lengths of XLPE cables. It was observed that with monopole type wave launchers a large ground plane orthogonal to the cable's axis is preferred from wave propagation point of view. But from a power system implementation point of view may not be a desirable choice. Thus a conformal surface wave launcher is also studied and designed. Using the conformal surface wave launcher open circuits faults were detected for various lengths of XLPE power cables. Initially tests were conducted using a VNA where TDR was employed. Subsequently a pulse generating circuit was developed and operated in conjunction with mixers and other circuit elements to detect open circuit faults. The proposed concept shows strong potential for implementation in the future. Given the depth and breadth of the problem outstanding issues that will need to be solved in future research include detecting other types of faults, e.g. insulation degradation, cable defects, defect resolution and the development of more sophisticated waveforms and algorithms. Furthermore, issues such as possible power line currents interfering with the sensor on-board electronics and the development of a true independent sensors node where the signal processing occurs on the sensor node are also important.

CHAPTER 6

A NEW METHOD TO ESTIMATE THE AVERAGE DIELECTRIC CONSTANTS OF AGED POWER CABLES

A new method to monitor and detect open circuit fault at power lines using non-intrusive using surface waves in conjunction with TDR was introduced in Chapter 5. As will be shown in the next Chapter, surface waves can also be used in conjunction with JTFDR to perform accelerated aging tests on cables. Aging invariably degrades cable insulation. Aged and degraded cables are one of the primary reasons for small scale blackouts and power interruptions. Along with expected or typical physical aging, the local environment where the cables operate contributes to the degradation of cable properties, accelerating the aging properties by means unanticipated by manufacturers' certification processes. In many cases, power cables suffer premature failures due to various kinds of local stresses, including electrical, thermal, mechanical, chemical etc. [17, 86-88]. In recent years, weather related events such as heat waves, high wind, storms and snowfall exacerbated the overall situation [87]. In the literature, methods have been proposed that utilize techniques, such as Time Domain Reflectometry (TDR) [16, 75, 89] Frequency Domain Reflectometry (FDR), and Joint Time-Frequency Domain Reflectometry (JTFDR) [32, 59] to detect hard faults (e.g. open circuit, short circuit, partial discharge) in cables.

However, in many cases cable sections that operate in particularly high stress environments (high heat, humidity etc.) may suffer gradual insulation degradation that occurs over a long period of time. This may also occur because of bending, vibration, shock, and injury due to being subjected to the weight of heavy objects either sitting on them or falling on them temporarily. Moisture or salt intrusion may exacerbate these situations even further. Examples may include underground power cables, instrumentation cables, aircraft cables, and heat stressed cables in nuclear power plants. At present, cable diagnostics focus on either (i) simulating the life of the cable and hence finding when they get damaged in a laboratory environment under the so called 'accelerated aging' environment or (ii) measuring real cable specimens from the field by decommissioning them from practical usage. Since the latter is disruptive and expensive the former is preferred. Accelerated aging, which is governed by the modified Arrhenius equation, can estimate the actual service aging of a cable at a certain operating temperature.

Accelerated aging, as represented in the following set of experiments, should be interpreted as a section of cable that has been experimentally aged in a laboratory to simulate its real operational age, which will be further reduced in the presence of high temperature, humidity or other stressors. In the past, accelerated aging tests on cables focused on issues such as Elongation at Break. More recently Wang *et al.*[32] proposed the application of the JTFDR technique to detect and to identify the location of a cable section that has undergone accelerated aging damage. A chirp signal with modulated Gaussian envelope was used to identify the aging locations in the cable specimens.

The fundamental principle of any of the reflectometry methods is that an incident waveform of proper amplitude and time-frequency signature if launched at one end of the cable will travel a distance and if it encounters an impedance discontinuity, a reflected waveform will result. By comparing the incident and reflected waveforms the location of the fault/defect is determined if the propagation velocity inside the cable is known. It is understandable that a cable section that undergoes accelerated aging will suffer insulation degradation which will manifest itself as a change in the impedance continuity and thus should be detectable as long as the discontinuity is measurable and that the reflected signal is distinguished from the noise due to the losses in the cable. Insulation damage corresponds to a change in the propagation constant, γ or more directly the dielectric constant of the material. If knowledge of the dielectric constant is available we can estimate from prior statistics the remaining life of a cable's insulation.

In this Chapter, a new mathematical formulation is presented that uses the experimental measurement data of accelerated aging of cable sections to estimate the average dielectric constants of such cable sections. The manufacturer or user may decide that if the dielectric constant decreases or increases by this percentage points they will discontinue the use of the cable or replace the cable with a new one.

This Chapter is organized as follows: in Section 6.1, the mathematical formulation that governs the dielectric constant estimation method is described. In Section 6.2, a brief description of the experimental data reported in [32] and used in this work is given. Third and finally, in Section 6.3 the results of the dielectric constant estimation are presented and discussed.

6.1 MATHEMATICAL FORMULATIONTO ESTIMATE THE DIELECTRIC CONSTANT OF AN AGED CABLE

The mathematical formulation developed below is based on the experimental setup shown in Fig. 6.1(a). A sample measured waveform in an oscilloscope screen is depicted in Fig. 6.1(b). Consider a cable with a section that has gone through the process of accelerated aging. In Fig. 6.1(a) the 'aged' shaded section is marked using dashed lines. The propagation constant of the baseline normal cable is γ with $\gamma = \alpha + j\beta$ where α (Np/m) is the attenuation constant and β (rad/m) is the phase constant. The length of the aged section is l_2, and its propagation constant is $\gamma_1 = \alpha_1 + j\beta_1$.

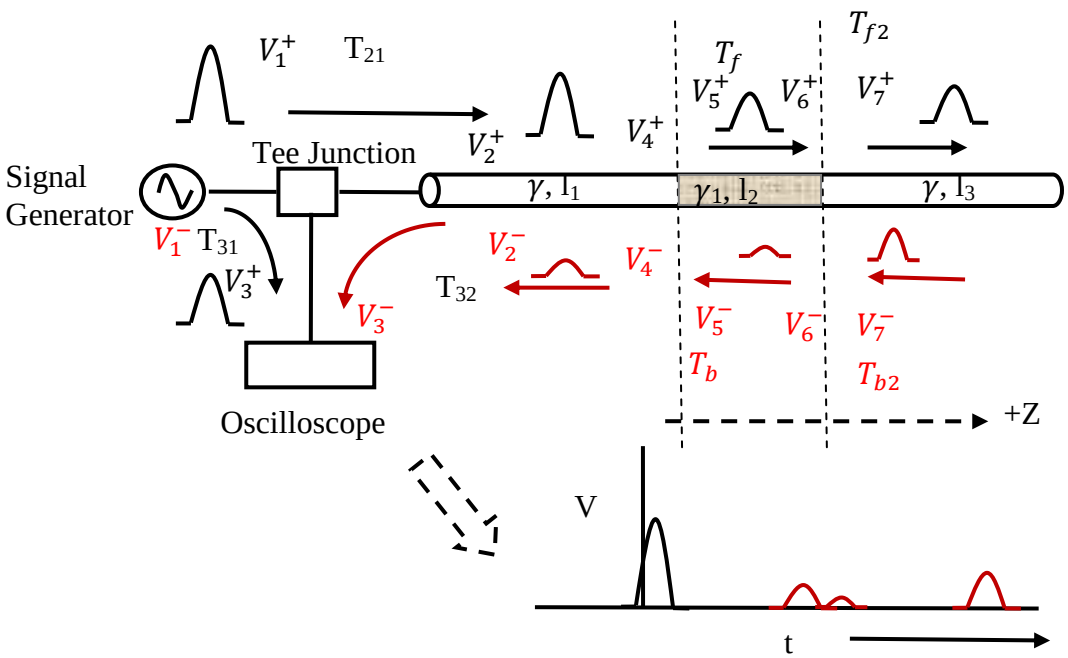

Figure 6.1. Experimental setup and definitions of terms.

At each junction or interface all quantities are labeled using different index numbers for clarity. Throughout the analysis the '+' sign indicates quantities related to forward traveling waves propagating in the '+z' direction while the '-' sign indicates quantities related to reverse traveling waves propagating in the '-z' direction. The first interface is

the junction between the signal generator and the 'T' junction. Considering the incident voltage generated by the signal generator to be V_1^+ the T-junction divides this incident voltage into a forward wave that travels towards the end of the test cable while a portion of V_1^+ travels to the other port of the T-junction connected to a measuring digital oscilloscope. At each junction there are corresponding reflected voltage waveforms with the '-' superscript. Below are the equations for the different waveforms.

$$V_2^+ = T_{21}V_1^+ \tag{6.1}$$

$$V_3^+ = T_{31}V_1^+ \tag{6.2}$$

$$V_3^+ = (T_{31}/T_{21})V_2^+ \tag{6.3}$$

$$V_4^+ = V_2^+ e^{-\gamma l_1} \tag{6.4}$$

$$V_5^+ = V_4^+ T_f = V_2^+ \left(1 + \Gamma_f\right) e^{-\gamma l_1} \tag{6.5}$$

$$V_6^+ = V_5^+ e^{-\gamma_1 l_2} \tag{6.6}$$

$$V_7^+ = V_6^+ T_{f2} = V_5^+ \left(1 + \Gamma_{f2}\right) e^{-\gamma_1 l_2} \tag{6.7}$$

From relations (6.3), (6.5) and (6.7) we can write,

$$V_7^+ = (T_{21}/T_{31})\left(1 + \Gamma_f\right)\left(1 + \Gamma_{f2}\right) V_3^+ e^{-(\gamma l_1 + \gamma_1 l_2)} \tag{6.8}$$

where T_{21} is the transmission coefficient of the 'T' junction corresponding to ports 1 and 2. T_f and $T_{f2}$are the transmission coefficients at the respective interfaces as shown in

Fig. 6.1. $\Gamma_f$and Γ_{f2} are the corresponding reflection coefficients at the appropriate interfaces. Similarly, reverse reflected signals are

$$V_6^- = T_{b2}V_7^- \tag{6.9}$$

$$V_6^- = (1 + \Gamma_{b2})V_7^- = \left(1 - \Gamma_{f2}\right)V_7^- \tag{6.10}$$

$$V_5^- = V_6^- e^{-\gamma_1 l_2} \tag{6.11}$$

$$V_4^- = T_b V_5^- = \left(1 - \Gamma_f\right)V_5^- \tag{6.12}$$

$$V_2^- = V_4^- e^{-\gamma l_1} \tag{6.13}$$

$$V_3^- = T_{32}V_2^- \tag{6.14}$$

Using relations (6.10) to (6.13) and substituting them in (6.14), it is easy to show that (6.14) becomes

$$V_3^- = T_{32}\left(1 - \Gamma_f\right)\left(1 - \Gamma_{f2}\right)V_7^- e^{-\gamma_1 l_2 - \gamma l_1} \tag{6.15}$$

whereT_b and $T_{b2}$are the transmission coefficients and Γ_{b2} and Γ_b are the corresponding reflection coefficients.

Considering an ideal open circuit at the other end

$$e^{-\gamma 2 l_3} = \frac{V_7^-}{V_7^+} \tag{6.16}$$

Using (6.8), (6.15), and (6.16) gives

$$e^{-\gamma 2 l_3} = \frac{T_{31} V_3^-}{T_{21} T_{32} \left(1 - \left|\Gamma_{f2}\right|^2\right)\left(1 - \left|\Gamma_f\right|^2\right) V_3^+ e^{-2(\gamma l_1 + \gamma_1 l_2)}} \tag{6.17}$$

Considering the 'T'-junction to be perfectly matched we can write $T_{21} = T_{31} = T_{32} = T$. Thus

$$e^{-\gamma 2 l_3} = \frac{1}{T\left(1 - \left|\Gamma_{f2}\right|^2\right)\left(1 - \left|\Gamma_f\right|^2\right) e^{-2(\gamma l_1 + \gamma_1 l_2)}} \frac{V_3^-}{V_3^+} \tag{6.18}$$

Rearranging (18) gives,

$$\frac{V_3^-}{V_3^+} = T\left(1 - \left|\Gamma_{f2}\right|^2\right)\left(1 - \left|\Gamma_f\right|^2\right) e^{-2\gamma(l_1 + l_3) - 2\gamma_1 l_2} \tag{6.19}$$

whose frequency response is

$$H(\omega) = \frac{FFT(V_3^-)}{FFT(V_3^+)} \tag{6.20}$$

Equation (6.19) contains amplitude and phase terms in the right hand side. We will only need the phase term to estimate the dielectric constant of the aged cable section.

In Fig. 6.1 the waveform at the oscilloscope consists of the injected and the reflected waveforms. By far, the predominant reflection arises from the open end but

there are other reflections from any impedance discontinuity (e.g. accelerated aging section).

Here are the main points:

1. Let $V_{RTa}(t)$be the waveform to be measured by the oscilloscope that consists of both the injected and the reflected waveforms. This waveform along with the injected waveform,$V_{INa}(t)$ are sampled at 8GS/s and return the discrete signal $V_{RT}[n]$ and $V_{IN}[n]$ where n represents the sample number.
2. Cross-correlation $X_{RTIN}(m)$ between $V_{RT}[n]$ and $V_{IN}[n]$ the injected waveform (see Fig. 6.2) is performed. The variable m corresponds to the "lag" or number of samples between signals and can then be scaled properly by the relation $t_p = \frac{m}{F_s}[s]$ or $d_p = \frac{m}{F_s} \cdot \frac{1}{2} v_p[m]$. The lag or t_p index value of the highest two peaks of the cross-correlation are selected to determine the time positions of the injected waveform location and the reflected waveform location t_1 and t_2 (or $d_1$and d_2) respectively.
3. Using a discrete rectangular time window at t_1 and a scaling of the sampled time as $t' = \frac{n}{F_s}$ the incident waveform $V_3^+[t'] = V_{RT}[t']V_r[t' - t_1]$ is separated from the $V_{RT}[t']$ where $V_r[t'] = V_0 rect[\frac{t'}{\sigma}]$ and σ is the width of the rectangular time window which depends on the time duration of the injected waveform and for this case V_0 is equal to 1.

4. Similarly the reflected waveform from the end of the cable is also separated from $V_{RT}(t)$ using a rectangular time window at t_2 ($V_3[t'] = V_{RT}[t']V_R[t' - t_2]$)($V_3^- = V_{RT}(t)V_r(t - t_2)$).
5. Let $v_3^+(\omega)$ and $v_3^-(\omega)$ be the corresponding Fourier transforms of $V_3^+$and V_3^- by FFT algorithm with selection of Nfrequency bins for appropriate resolution ofω.
6. The phase $\theta(\omega)$ is obtained by subtracting the phase of $v_3^-(\omega)$ from $v_3^+(\omega)$

$$\theta(\omega) = \angle v_3^-(\omega) - \angle v_3^+(\omega) \tag{6.21}$$

This phase $\theta(\omega)$is related to the phase constant, β of the normal cable as well as the phase constant, $\beta_l$of the aged section of the cable. However, the β and β_l are related to the relative dielectric constants of the respective cable sections, e.g. 'normal' or 'aged.' For the normal cable section, $\theta(\omega)$ should be equal to $-\beta L + \phi$, where L is the total length of the cable and ϕ results from the T junction and other interfaces. For the proposed implementation shown in Fig. 6.1, we can write $\theta(\omega)$ equal to $-\beta(l_1 + l_2 + l_3) + \phi$.

As experimental signals, both amplitude and phase are affected by noise sources. So the experimental phases at all frequencies may not be equal. Another problem is that the actual phase change may differ from the measured phase change by $\pm 2n\pi$ where n is an integer.

To solve this problem we unwrapped the phase and used the Least Square Method to find the best linear fit for the phase response. Note that β is related to the average

dielectric constant by $\beta L = \frac{2\pi f\sqrt{(\epsilon_r)}}{c}(l_1 + l_2 + l_3)$. We can obtain the average dielectric constant $\epsilon_r$for a good cable from the slope of the fitted curve.

Again, for an 'aged' cable section of length l_2 with phase constant of β_1 following steps 1 to 6, $\theta(\omega)$ equals to $-\beta(l_1 + l_3) - \beta_1 l_2 + \phi_1$. Thus, $\beta_{\text{aged}} L = \frac{2\pi f\sqrt{(\epsilon_r)}}{c}(l_1 + l_3) + \frac{2\pi f\sqrt{(\epsilon_{r1})}}{c} l_2$. For a predefined 'aged' section, we can calculate the average dielectric constant $\epsilon_{r1}$for the 'aged' section using the value of the dielectric constant $\epsilon_r$for a normal cable. In summary, the phase response of a cable with an 'aged' section is

$$\angle H_b(\omega) = -\beta(l_1 + l_3) - \beta_1 l_2 + \phi_1 \tag{6.22}$$

and the phase response of a normal cable is

$$\angle H_g(\omega) = -\beta(l_1 + l_2 + l_3) + \phi_2 \tag{6.23}$$

Therefore,

$$\angle H_b(\omega) - \angle H_g(\omega) = -(\beta_1 - \beta) l_2 + (\phi_1 - \phi_2) \tag{6.24}$$

We can rewrite the above equation as

$$\angle H_b(\omega) - \angle H_g(\omega) = -2\pi f\left(\sqrt{\epsilon_{r1}} - \sqrt{\epsilon_r}\right) l_2/c + (\phi_1 - \phi_2) \tag{6.25}$$

Thus using the above equations, and having the length,l_2, of the 'aged' section, we can calculate the average relative dielectric constant, ε_{r1} of the 'aged' section.

6.2 EXPERIMENTAL METHODOLOGY

To use and validate the above mathematical formulation we used the experimental accelerated aging data reported in [32]. The measurements reported there relate the peak cross-correlation with the aging time and was previously compared to elongation at break (EAB). The experimental setup used in [32] is illustrated in Fig. 6.2 and described below.

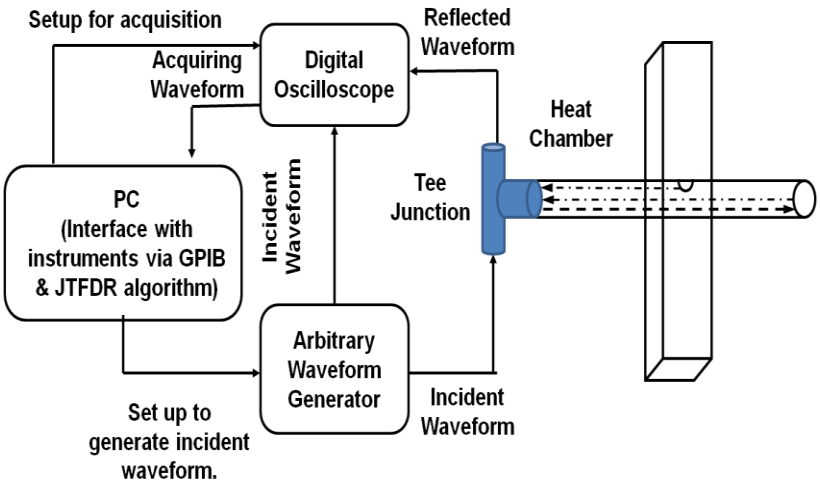

Figure 6.2. The experimental setup used in the accelerated aging tests reported in [70].

The setup consists of a Tektronics AWG 610 signal generator, an Agilent Infiniium 5474 digital oscilloscope, a T-junction power divider, and a desktop PC for measurement control and data acquisition. To conduct the accelerated aging tests a section of the cable specimen was placed inside a heat chamber. A Joint Time-Frequency Domain Reflectometry (JTFDR) waveform was used consisting of a linear chirp signal enveloped by a time-frequency optimized Gaussian pulse. The center frequency of the waveform was 100 MHz, with time duration of 40ns.The accelerated aging tests reported in [10], were performed on an XLPE insulated cable and an Ethylene Propylene Rubber (EPR) insulated cable. In both cases, the cables were 10 m long. The 1m long aging hot

spots were located along the length of the cable at 5 meters from the measuring end. XLPE insulated cable sections were heated in the heat chamber at 140^0 C for 32 hours to simulate an aging condition of 120 years of service life at 50^0 C. The test temperature was determined using the modified Arrhenius equation [90]

$$\frac{t_s}{t_a} = e^{[\frac{E_a}{B}(\frac{1}{T_s}-\frac{1}{T_a})]}$$

whereT_S is the service temperature K,

T_a is the accelerated aging temperature K,

$t_s$is the aging time in hours at service temperature,

$t_a$is the aging time in hours at acceleration temperature,

E_a is the activation energy of the insulation material (1.33eV for XLPE),

B is the Boltzmann's constant=1.38 X 10^{-23}J/K= 8.617 X 10^{-5}eV/K.

Thus, it follows that the accelerated aging temperature can be derived as$T_a = \left[\frac{1}{T_s} - \frac{B}{E_a}\ln(t_s/t_a)\right]^{-1}$.EPR insulated cable specimens were heated for 48 hours at 160°C, to simulate 120 years of service aging at 50^0 C. The activation energies for the XLPE and EPR insulation materials were 1.33 and 1.1 eV (125.4 and 106.1 kJ/mol), respectively [91].

6.3 PROPOSED ANALYSIS AND RESULTS

6.3.1 ACCELERATED AGING

Here we analyze the experimental data reported in [10] on the basis of the mathematical formulation we presented earlier and estimate the dielectric constants of the cable sections that had undergone accelerated aging. A uniform insulation dielectric constant was assumed throughout the aged section of the cable. The XLPE insulated cable had a dielectric constant of 2.3 [92]. Nevertheless, other literature suggests a range of values for the dielectric constant between 2.3 and 6 (see Table 6.1 and [93]). The EPR insulated cable had a dielectric constant between 2.5 to 3.5 (see Table 6.1 and [93]).

Fig. 6.3(a) shows a sample response observed at the oscilloscope for a thermally aged, degraded section of cable. The first dominant part of the waveform represents the injected input waveform. As the incident waveform propagates down the cable and is reflected back to the measurement point, the last dominant part of the waveform represents the reflection from the open end. The middle non-dominant part of the waveform represents the thermally aged section.

Following steps 2 to 4 in Section 6.2, we can separate the injected and reflected waveforms (Figs 6.3(b)-6.3(c)). Here we used a rectangular time window function with 70ns duration. Then according to steps 5 and 6, the phase components at different frequencies were extracted using FFT. The final experimental phase response obtained, using (6.22), is plotted in Fig. 6.4. The least square curve fitted response is also shown.

This response is taken within a particular frequency bandwidth 50 MHz to 200 MHz.

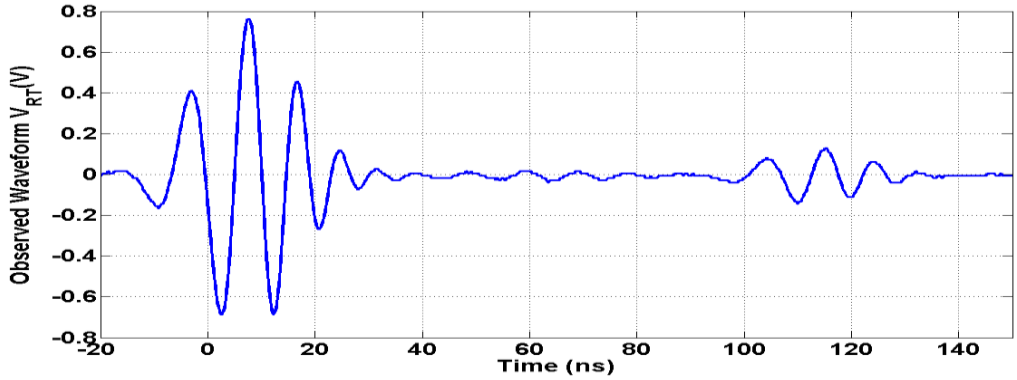

(a)

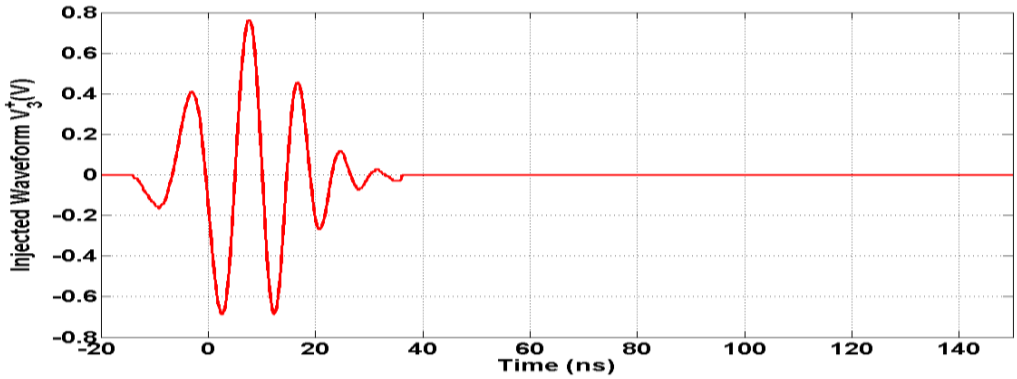

(b)

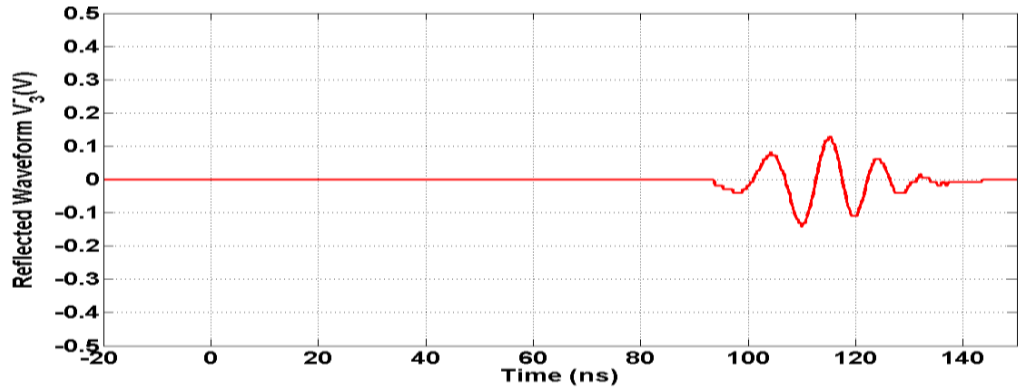

(c)

Figure 6.3 (a). Total signal (V_{RT}) observed at oscilloscope. 6.3(b) Truncated signal corresponding to injected signal (V_3^+) using rectangular time window at t_1. 6.3(c) Truncated signal corresponding to reflected signal from the end (V_3^-) using rectangular time window at t_2.

From the information of the slope difference between a normal and aged cable sections we can calculate the relative dielectric constant of the aged cable section using (6.22) to (6.25). Fig. 6.5 shows the average dielectric constant of the aged cable section (length 1 m) as function of the accelerated aging hour for the XLPE insulated cable. Before aging, the dielectric constant of a normal cable is 2.55.It is clear from Fig. 6.5 that for this cable accelerated aging decreases the dielectric constant. For 32 hours of heating at 140°C which is modeled to be equivalent to 120 years of service aging at 50°C, the dielectric constant decreases to 1.67. This is a 34.5% reduction.

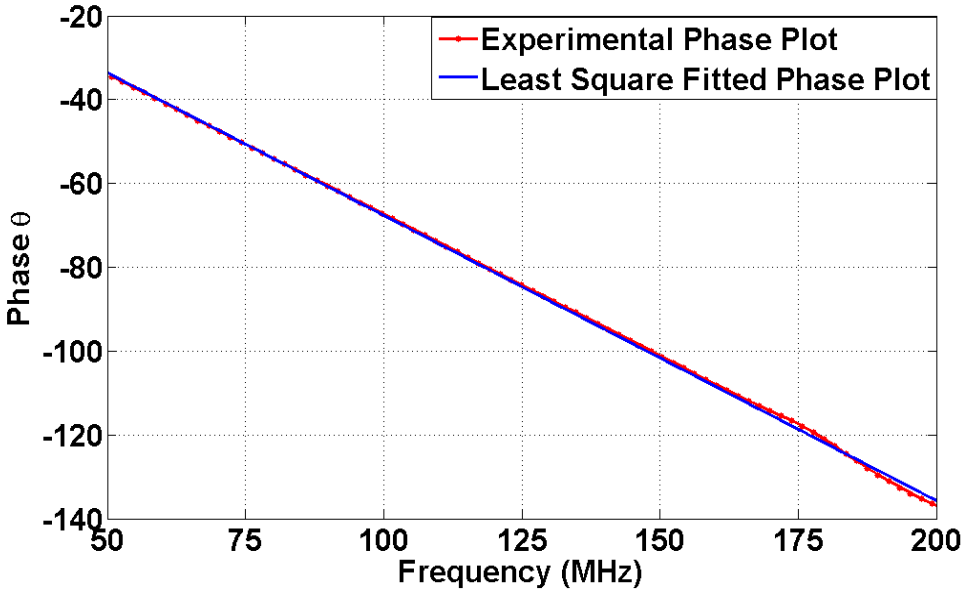

Figure 6.4. Experimental phase plot with least square error fitted phase plot.

Fig. 6.6 shows the average dielectric constant of the aged cable section (length 1 m) as a function of the accelerated aging hour for the EPR insulated cable. Before aging the dielectric constant of a normal cable is 3.09.It is clear from Fig. 6.6 that for this cable also accelerated aging decreases the dielectric constant. However, the decrease is not as

fast as that which occurs for XLPE. For 48 hours of heating at 160°C which is equivalent to 120 years of service aging at 50°C, the dielectric constant of the EPR cable decreases to 2.77. This is only a 10.4% reduction.

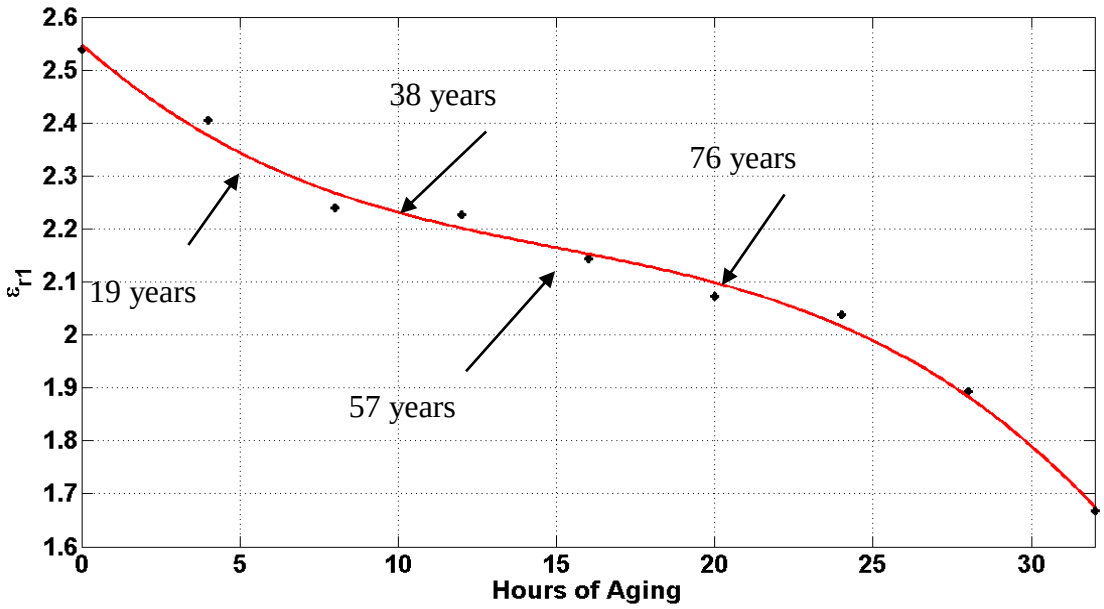

Figure 6.5. Average dielectric constant, ε_{r1} determined using the proposed method for XLPE insulated aged cable section. XLPE insulation with aged section length = 1 m.

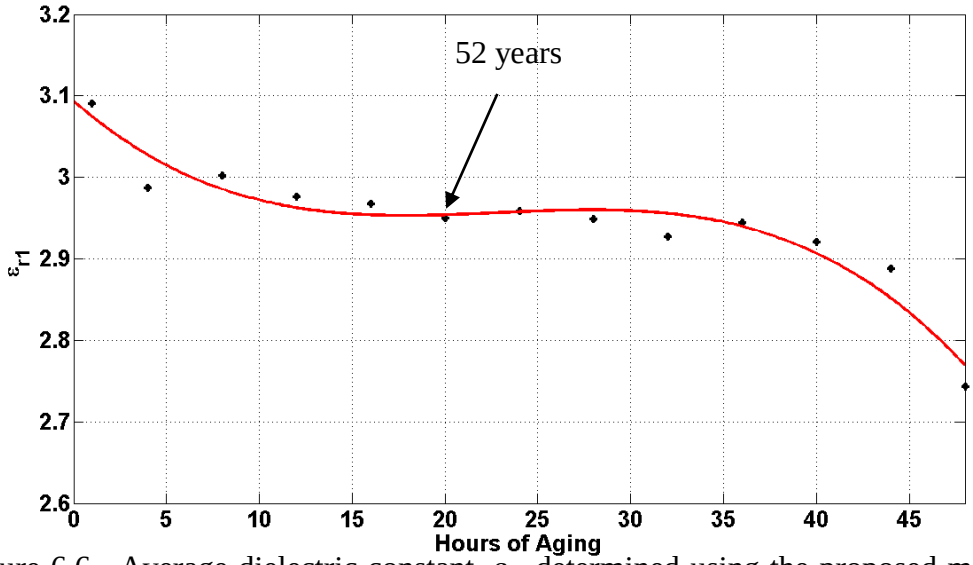

Figure 6.6. Average dielectric constant, ε_{r1} determined using the proposed method for EPR insulated cable section. EPR insulation with aged section = 1 m.

Table 6.1: Comparison of relative permittivity

Cable Type	Dielectric Constant	Dielectric Constant measured using our proposed method
Cross-Linked Polyethylene (XLPE)	2.3 [92], 2.3-6.0 [93]	2.55
Ethylene Propylene Rubber (EPR)	2.5-3.5 [93]	3.09

6.3.2 ARTIFICIAL WATER INTRUSION IN CABLE

It is clear that using our proposed method the dielectric constant of an 'aged' cable section can be determined by extracting the phase information of a normal and an aged cable and then comparing them. This can be done from the data set obtained from prior TDR or JTFDR measurements. However, the natural question will be - is this method then also capable of finding an increase in the material dielectric constant due to other commonly induced faults in real-world cable systems? Real-world viability of this metric is further tested by simulating water intrusion.

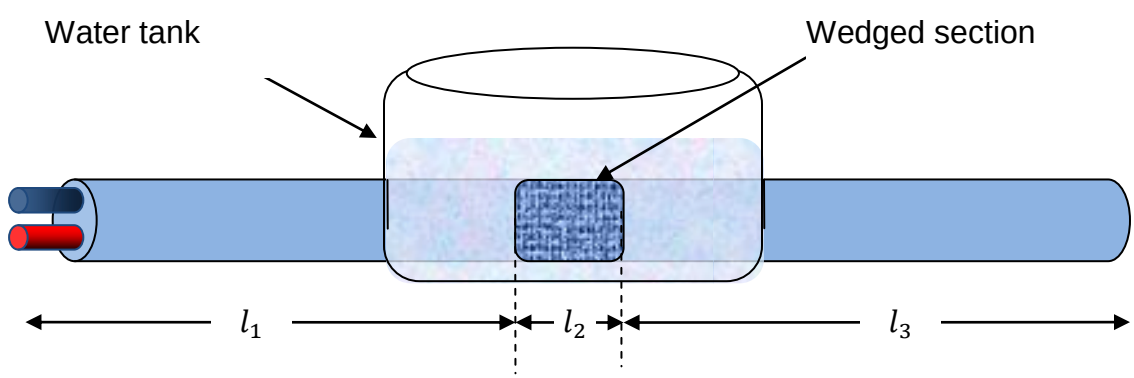

Figure 6.7. The experimental setup used for artificial water intrusion in XLPE cable. The wedged section is 2.5 cm long.

To investigate the real-life phenomenon of water intrusion, about half of the insulation along the circumference of a 2.5 cm long section was removed and thus a recessed wedge was created. This recessed wedge was located 5.78 m from the end of a 10 m long XLPE insulated cable sample.

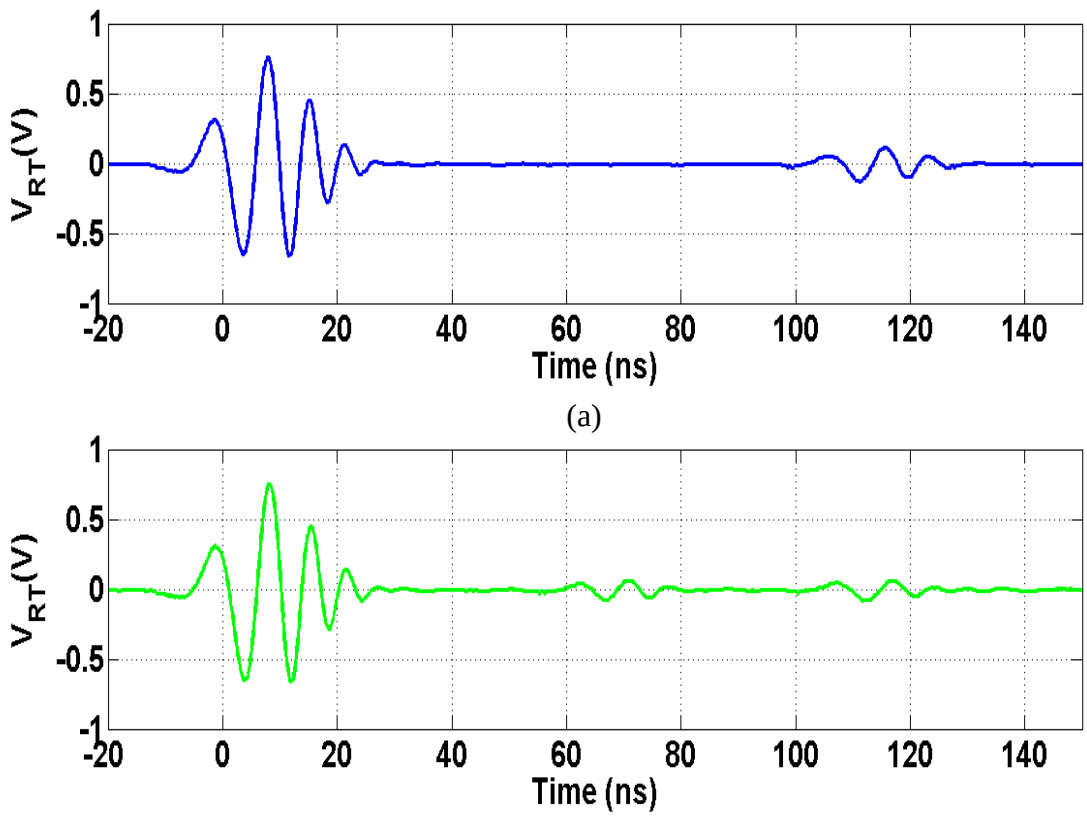

Figure 6.8 (a).Total waveform (V_{RT}) of the cable under test before water is introduced in the wedge.
(b) Total waveform (V_{RT}) of the cable under test after water is introduced in the wedge.

Then water was placed in the 2.5 cm long wedge section (see Fig. 6.7). Fig. 6.8(a) shows the total return signal at the oscilloscope before water was introduced into the wedge while Fig. 6.8(b) shows the total return signal after water was introduced. As indicated in Fig. 6.8(b) the water intrusion causes the additional reflections labeled in the

Figure. Following steps 2 to 6 and using (6.22) to (6.25), we determined that the average dielectric constant of the wedge section was 20.7, far higher than the dielectric constant of XLPE yet lower than that of water (about 80). This is because water is present only in a small volume of the 2.5 cm long cable and is also being averaged.

A mathematical formulation to estimate the average dielectric constants of cable sections that have undergone accelerated aging tests is proposed. Although only experimental results for the cases considering *accelerated aging* are presented, the proposed method is also suitable for cables that have undergone real-life aging. Under the proposed scheme the experimental results obtained from reflectometry measurements are used to estimate the average dielectric constant of the material under consideration. By comparing the phase responses of an aged cable and a normal cable the average dielectric constant is predicted. The experimental data obtained for two types of cables XLPE and EPR show that the dielectric constant decreases with accelerated aging (34.5% decrease for XLPE insulated cable and 10.4% decrease for EPR insulated cable for 120 years of real time operating age under a temperature of 50^0C). Through our experiments, we found support for the statement, "EPR has good high temperature performance. Although soft, it deforms less at high temperature than XLPE and maintains its insulation strength well at high temperature" [94].

On the other hand, when a small section of a cable was intentionally damaged by removing part of the conductor and insulation and the resulting wedge was submerged in water the measured average dielectric constant increased significantly (20.7 compared to 2.3). Therefore, the proposed method can estimate both an increase and decrease in the dielectric constant of the material of a cable section that has undergone natural aging or

accidental disruption in its dielectric properties because of damage and subsequent intrusion of foreign high dielectric constant materials. Limitations of the proposed approach include (1) the assumption of a uniform aged section, (2) a single-aged section being considered, and (3) a relatively long section of cable under good condition is required to apply the windowing method in the time domain.

CHAPTER 7

NON-INTRUSIVE ACCELERATED AGING EXPERIMENTS WITH SURFACE WAVE LAUNCHER

In this Chapter, we combine the two key concepts presented in the previous Chapters; surface wave launcher for non-intrusive cable fault detection (Chapter 5) and JTFDR assisted accelerated aging test and dielectric constant estimation (Chapter 6). One important objective of this dissertation is to develop a non-intrusive cable diagnostic technique for soft faults or incipient faults, such as insulation degradation. In this Chapter, we demonstrate the application of the surface wave launcher and JTFDR technique in accelerated aging related insulation damage detection in XPPE cables.

The Chapter is organized as follows. Section 7.2 describes the experimental procedures and the test setup. Section 7.3describes a brief comparison between direct (intrusive) and non-intrusive measurements. Section 7.4 presents the experimental outcomes and analyzes the results. Finally Section 7.5 summarizes the findings of these experiments.

7.1 EXPERIMENTAL SETUP FOR JTFDR WITH WIDE MONOPOLE LAUNCHERS

Fig. 7.1 shows the experimental setup using which the JTFDR technique is applied with the help of surface wave launchers in order to detect aging related cable insulation degradation. The arbitrary waveform generator generates a predefined Gaussian chirp incident signal when instructed by a Matlab program. The program defines the optimized center frequency, bandwidth and time duration for the signal. The incident signal propagates along the unshielded cable. Prior to that it travels through a T-junction and a coaxial instrumentation cable. The Gaussian chirp signal when emitted from one port of the T-junction is injected into the surface of a cable which then generates a propagating surface wave at the conductor-dielectric interface of the unshielded test cable. The other port of the T-junction is directly connected to a digital oscilloscope in order to view the incident waveform. When the propagating surface wave finds an impedance discontinuity due to accelerated aging it returns a reflected waveform. The incident and reflected waveforms are both acquired in the oscilloscope. Next, time-frequency cross-correlations are performed and used to determine the location of the aging related insulation degradation. To minimize external interference, the test cables were hung from the ceiling using nylon ropes and cardboard tubes. Wooden posts were also placed to secure the cables at the start, in the middle and at the end.

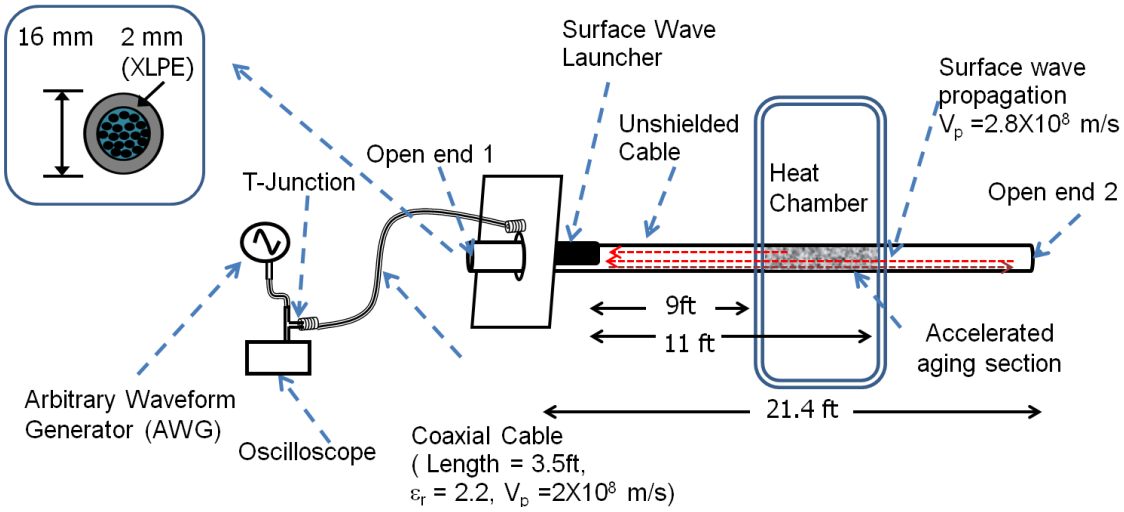

Figure 7.1. Non-intrusive accelerated aging test system functional diagram.

Figure 7.2. Photograph of non-intrusive accelerated aging test.

Fig. 7.2 shows a photograph of the non-intrusive accelerated aging related insulation degradation test. The unshielded cable used for this experiment is the same one

used in Chapter 5 (commercially available). The cable was 22.9 ft long. We used a wide monopole launcher for these experiments which was described in Chapter 5 Section 5.1. A cylindrical shaped wide monopole launcher was fabricated using flexible copper tape with 16 mm diameter and 2 mm slit. The monopole was placed on a rectangular aluminum ground plane measuring 415 mm by 260 mm. The ground plane had a 18 mm diameter hole at its center so that the test cable can pass through. The wide monopole surface wave launcher was placed 6 inch from the one open end of the test cable. An additional 50 Ω 3.5 ft coaxial instrumental cable was used to make the connection between the T-junction and the surface wave launcher. A small section of the test cable was then placed inside a controlled heat chamber as illustrated in Fig. 7.1. However, the metal walls of the heat chamber presented new challenges for our surface wave measurements; they were blocking the reflected waves from the aging locations. To circumvent this problem the following steps were followed:

- Before aging, the input and reflected waveforms from the test cable were acquired and processed in Matlab for time-frequency cross-correlation and future comparison.
- Then the intended section of the test cable was put into the heat chamber and heated at a predefined temperature for a 2 hour interval.
- Then the test cable was carefully taken out from the heat chamber, hung properly, and the reflected waveform was acquired.
- Finally a time frequency cross-correlation was performed in Matlab to analyze and understand the measurement.

7.2 REFLECTOMETRY COMPARISON: DIRECT AND NON-INTRUSIVE MEASUREMENTS

In this Section, we compare the difference between the direct contact and non-intrusive waveforms in terms of their power spectra. This comparison is more qualitative than quantitative since the former was applied to shielded coaxial cable while the latter is applied to unshielded cable. One key difference between the two approaches is that for the former the propagating wave is a Transverse Electro Magnetic (TEM) wave that is found in 2-conductor transmission lines and in free-space. Such waves are non-dispersive and their phase constants and wave numbers are essentially the same. While the non-intrusive method launches a propagating surface wave of the TM (Transverse Magnetic) type for which dispersion is a reality.

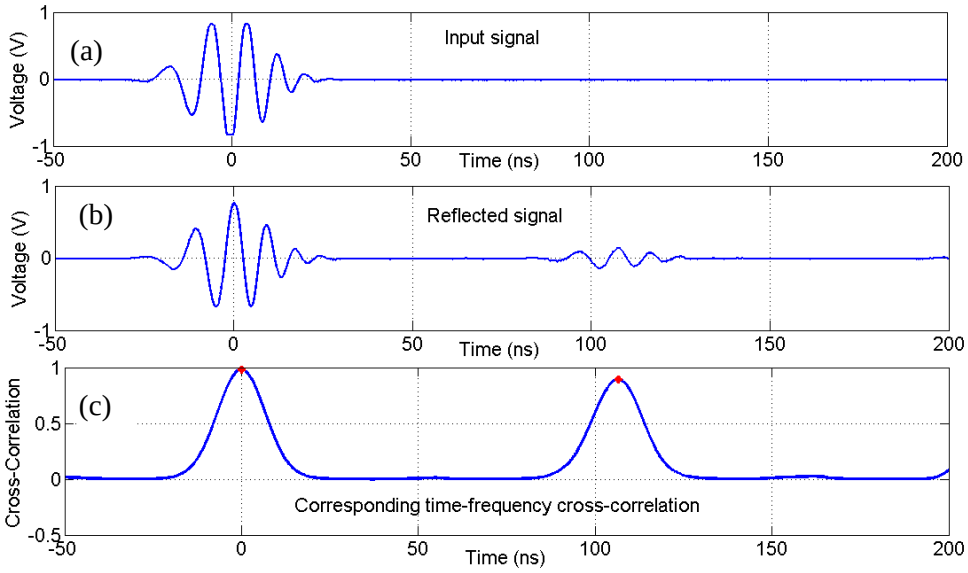

Figure 7.3. Direct contact method of JTFDR fault detection. Coaxial 10 m long shielded XLPE power cable; 100 MHz center frequency of input waveform a) Input signal b) Output signal c) corresponding time-frequency cross-correlated signal.

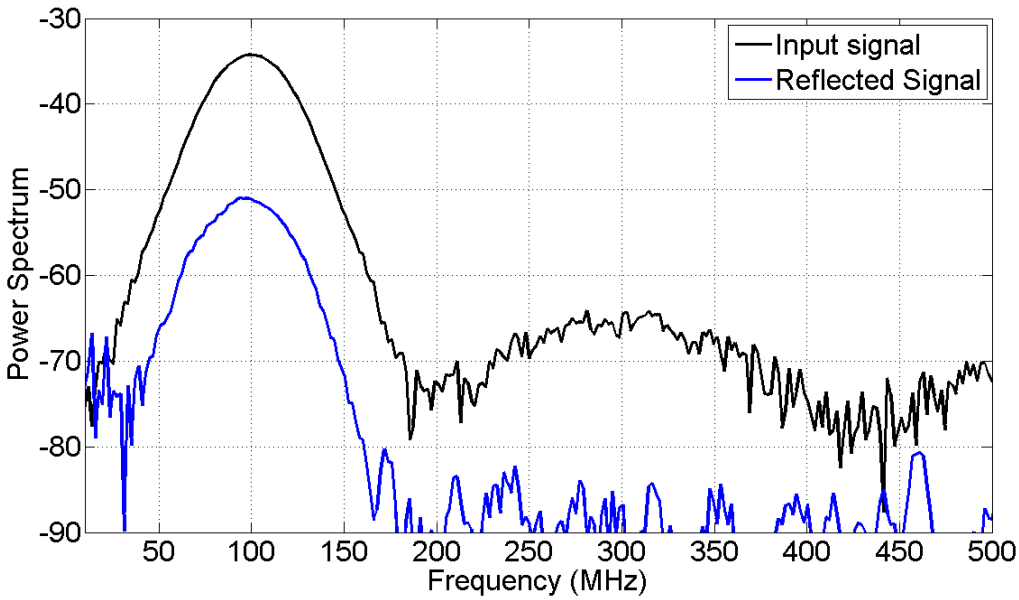

Figure 7.4. Power spectra comparison between input and reflected signal of Fig. 7.3.

Fig. 7.3 plots the direct contact input signal, reflected signal and their corresponding time-frequency cross-correlations for a 10 m long shielded XLPE cable. The injected signal used here was a 100 MHz Gaussian chirp signal with 100 MHz bandwidth and 30ns time duration. The power spectra versus frequency of the input signal and the reflection from the open end are plotted in Fig. 7.4. The 6- dB bandwidth of the input signal is 55 MHz (72 MHz to 127 MHz) and the 6- dB bandwidth of the reflected signal (from the open end) is 59 MHz (66 to 125 MHz). At 100 MHz, the difference between the two spectra is 17 dB.

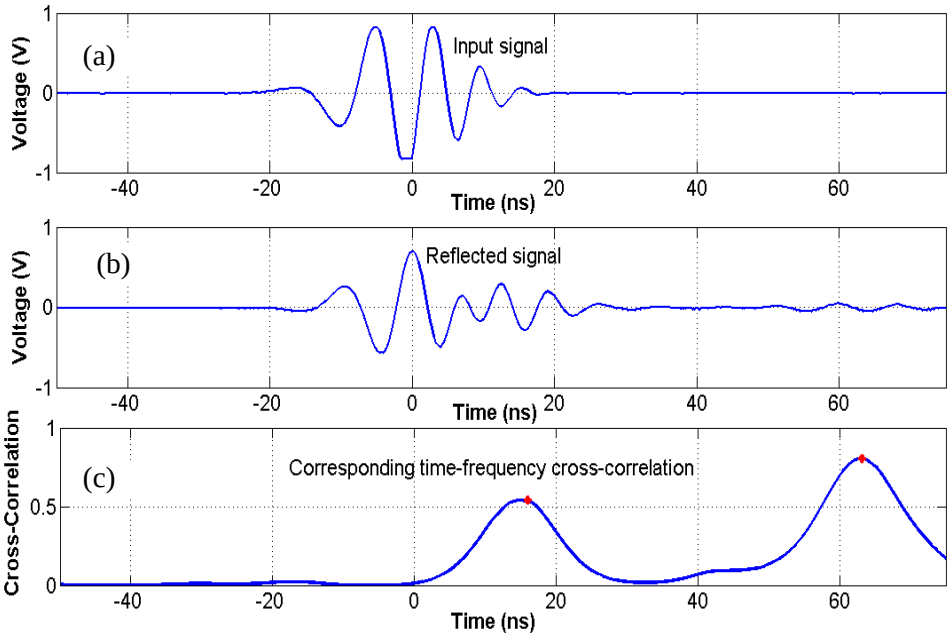

Figure 7.5. Non-Intrusive JTFDR waveforms for a 22.4 ft (6.83 m) unshielded XLPE insulated power cable along with 3.5ft coaxial instrumental cable using120 MHz JTFDR signal a) Input signal, b) reflected signal, and c) corresponding time-frequency cross-correlated signal.

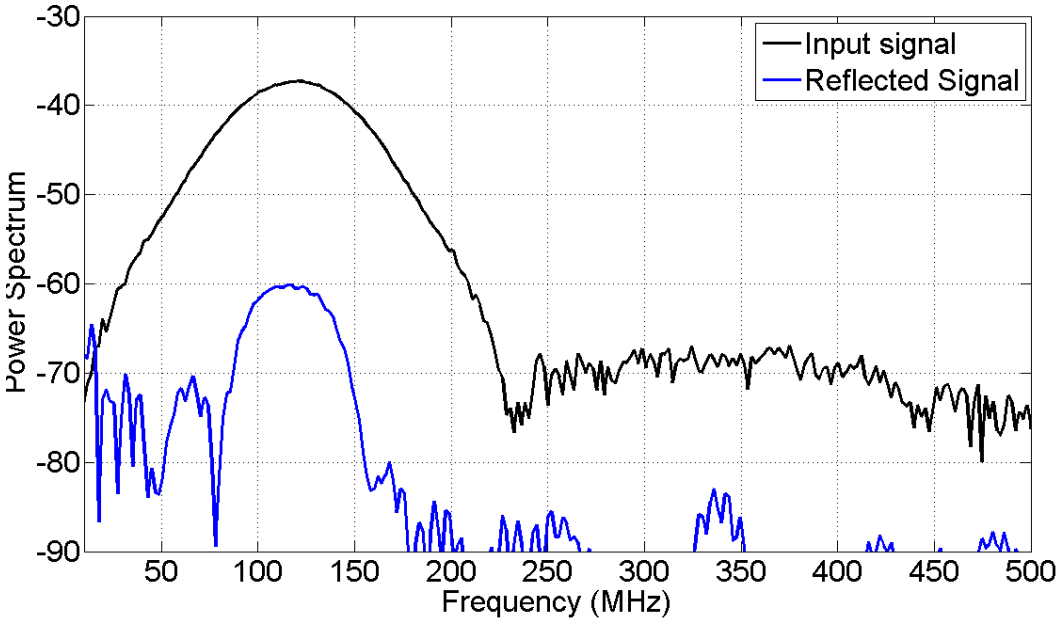

Figure 7.6. Power spectra comparison between the input and reflected signals of Fig. 7.5.

Fig. 7.5 plots the input signal, reflected signal and the corresponding time-frequency cross-correlation for a 22.4 ft (6.83 m) long unshielded XLPE insulated power cable with a 3.5ft coaxial instrumentation cable. The injected signal used here was a 120 MHz Gaussian chirp signal with a 100 MHz bandwidth and 30ns time duration. The power spectra versus frequency of the input signal and the reflection from the open end are plotted in Fig. 7.6. The 6- dB bandwidth of the input signal is 82 MHz (78 MHz to 160 MHz) and 6- dB bandwidth of the reflected signal (from the open end) is 53 MHz (89 to 142 MHz). At 120 MHz, the difference between the two spectra is 23 dB. It is apparent that the non-intrusive method of detection has about 6 dB more attenuation at the center frequency. At some frequency range such as 70-89 MHz and 150 to 170 MHz the differences are high. These represents that the signals at those frequency ranges reflect back at the insertion port of the surface wave launcher and create distorted reflected waveform. This also results in distorted cross-correlation traces. However, while choosing the center frequency and the bandwidth of the JTFDR signal (for surface wave type insulation degradation detection for unshielded cables), we have to consider two major points, if the center frequency is too low, the location resolution will be poor. On the other hand, if the center frequency is too high the resulting attenuation will also be limiting the range.

7.3 ACCELERATED AGING TESTS RESULTS

The test cable used was unshielded XLPE. As noted before in Chapter 5 the activation energy of XLPE is 1.33eV [91, 95]. The test cable was placed according to the illustration shown in Figs. 7.1 and 7.2 and heated in the heat chamber at 140^0C (413K)

for 8, 10, and 12 hours to simulate a service aging of 30, 38, and 46 years at an operating temperature of 50^0C (323K).

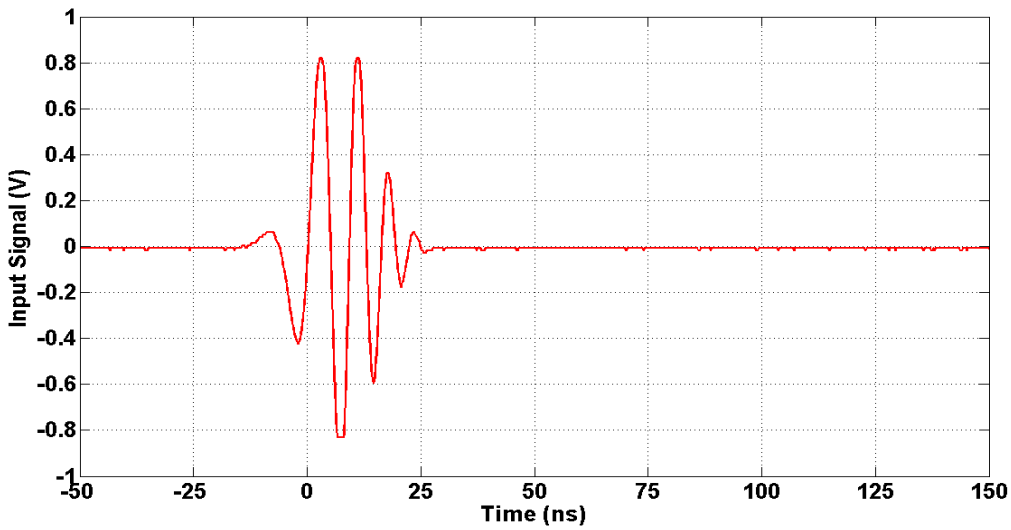

(a)

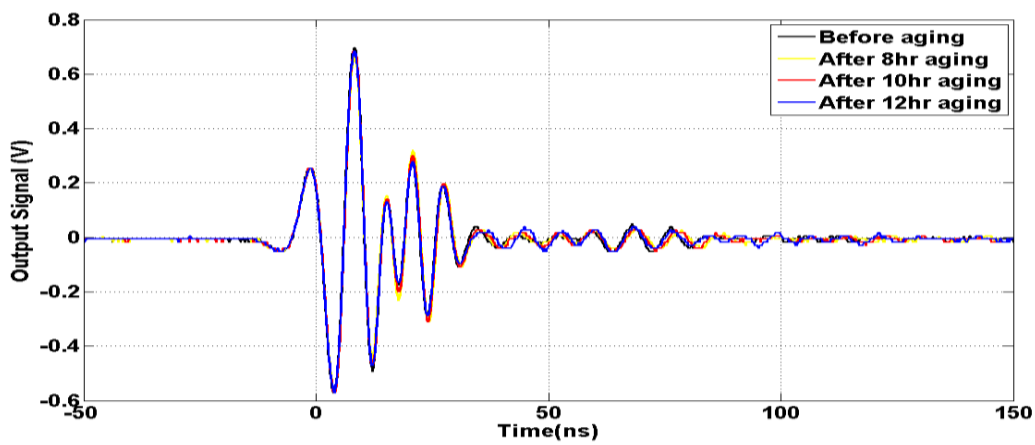

(b)

Figure 7.7. a) The first reference input signal generated from AWG ($f_r = 120\ MHz, BW = 100MHz, t_D = 30\ ns$).
b) Return reflected signals for the unshielded cable at different aging periods.

Two sets of experiments were carried out considering two different reference signals. The first JTFDR reference signal had a center frequency of 120 MHz, bandwidth of 100 MHz and time duration of 30 ns. This reference signal is shown in Fig. 7.7 (a). The second JTFDR reference signal had a center frequency of 150MHz, bandwidth of

100 MHz and time duration of 30 ns. The injected second reference signal is shown in Fig. 7.9 (a).

The return reflected signal waveforms are plotted in Fig. 7.7 (b). In this plot the yellow, red, and blue traces represent the return reflected signals at 8 hrs, 10 hrs and 12 hrs of aging at 140°C which corresponds to about 30 years, 38 years, 46 years of simulated service life at 50°C service temperature, respectively. Corresponding plots of the time-frequency cross-correlation functions are shown in Fig. 7.8. In Fig. 7.8, the resultant cross-correlations show peaks at the beginning which corresponds to the initial input waveforms. The resultant cross-correlations also show peaks at the end of the cable which correspond to the reflection from the open cable ends. The cross-correlations peaks that can be seen in between those two correspond to the reflection from apparent insulation degradation due to the accelerated aging inside the heat chamber. The phase velocity of the wave used to determine the location of the accelerated aging related insulation degradation was is 2.8×10^{8} m/s which was reported in Chapter 5 Section 5.4.

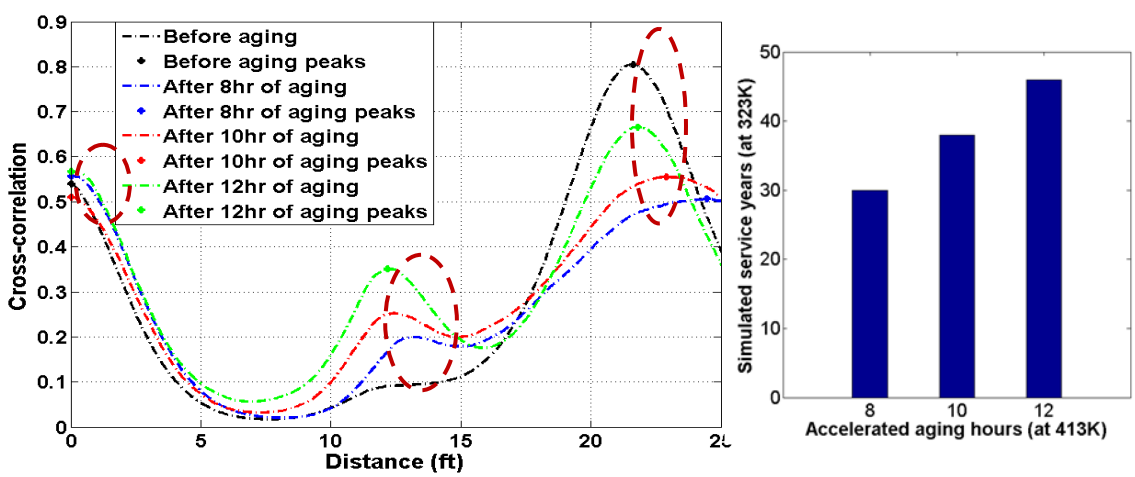

Figure 7.8. Cross correlations at different aging periods for the first reference signal ($f_r = 120\ MHz, BW = 100MHz, t_D = 30\ ns$).

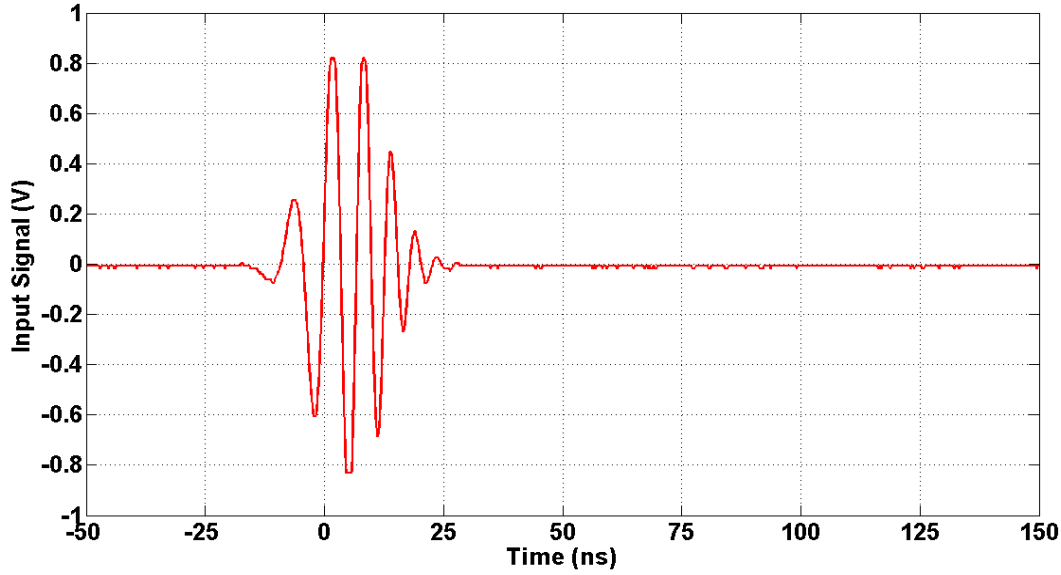

(a)

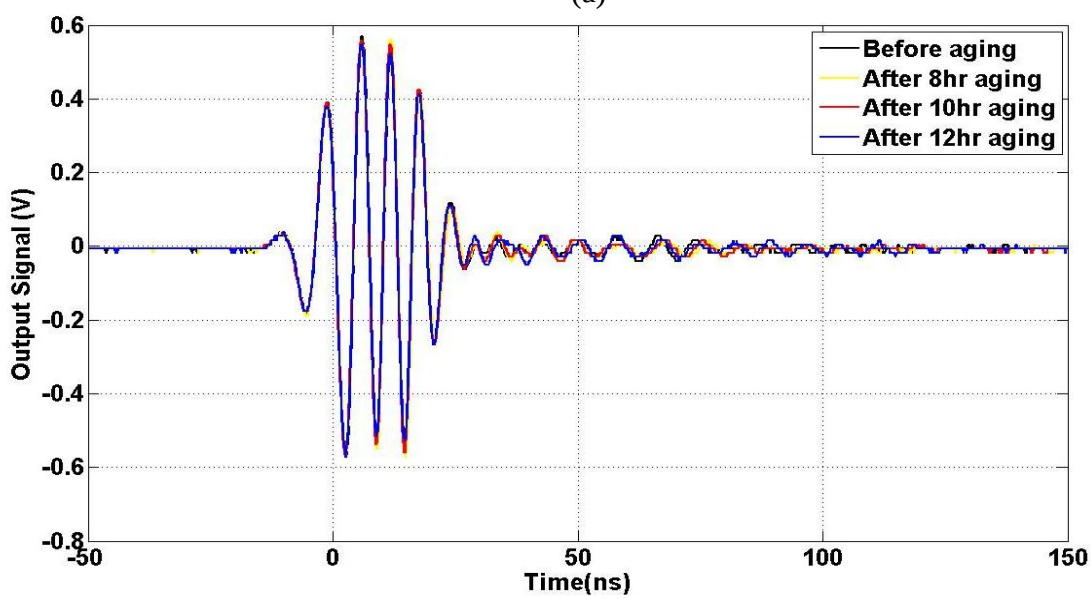

(b)

Figure 7.9. a) The second reference input signal generated from AWG ($f_r = 150\ MHz, BW = 100MHz, t_D = 30\ ns$). b) Return reflected signals for the unshielded cable at different aging periods.

Since the relative dielectric constant of the 3.5ft long instrumentation coaxial cable that precedes the test XLPE cable is 2.2 the phase velocity of the wave in the instrumentation cable is 2×10^8 m/s. The propagation delay introduced by the

instrumentation cable with a phase velocity of 2×10^8 m/s is equivalent to the propagation delay introduced by a hypothetical 2.5 ft long cable with phase velocity 2.8×10^8 m/s. This allows the aging related hot spot location determination with only one phase velocity, 2.8×10^8 m/s. Based on these observations according to Fig. 7.8(a)the aging hot spots should be located between the 11.5 ft. and 13.5 ft. mark of the test cable from its start. As seen in Fig. 7.8 the hot spot locations corresponding to the first reference signal occur at length markers 12.5, 12.3, and 11.8 ft. respectively. The shift in the location of the time-frequency cross-correlation with time indicates further degradation in the insulation. Note that more accurate pin-pointing will require the use of the actual phase velocity as function of the aging related degradation.

Similarly, for the second reference signal (with a center frequency of 150MHz, bandwidth 100MHz and time duration of 30 ns), the return reflected signal waveforms are plotted in Fig. 7.9(b). The black trace represents the reflected output signal before aging. In this plot, the yellow, red, and blue traces represent the return reflected signals at 8hrs, 10 hrs and 12 hrs of aging at 140°C which corresponds to 30 years, 38 years, 46 years of simulated service life at 50°C service temperature, respectively. Corresponding plots of the time-frequency cross-correlation functions are shown in Fig.7.10. The black, blue, red, and green traces indicate the before aging, 8 hrs, 10 hrs and 12 hrs of aging, respectively. The hot spots corresponding to the second reference signal occur at lengths 12.3, 13.8, and 14.8 ft. respectively.

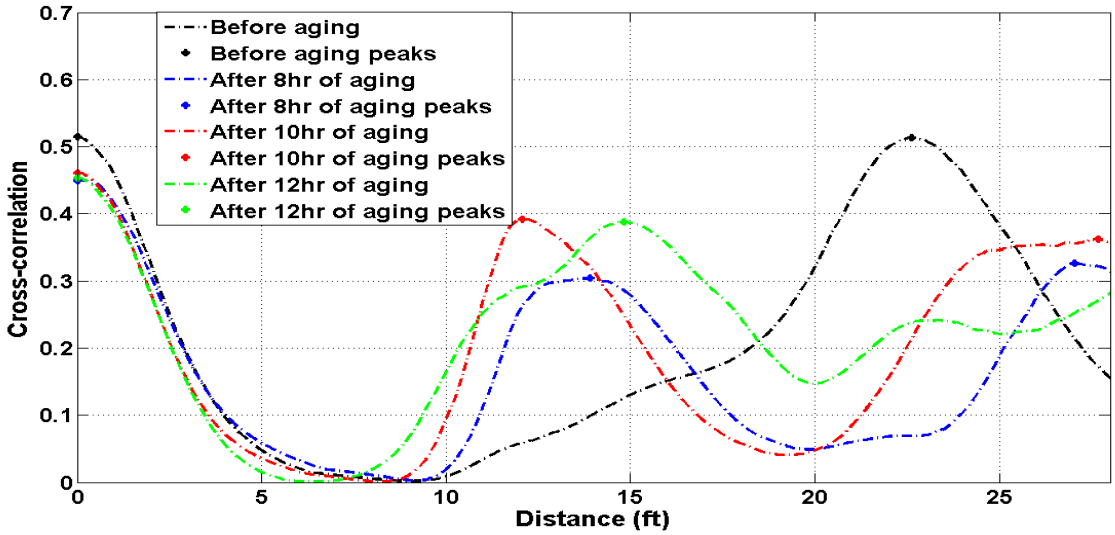

Figure 7.10. Cross correlations at different aging periods for second reference signal ($f_r = 150\ MHz, BW = 100MHz, t_D = 30\ ns$).

Since the hot spot insulation degrades with increase of aging hour, the dielectric constant of the insulation of the hot spot decreases which will lead to increasing the phase velocity at a particular frequency. The flatness of the time-frequency cross-correlated curves also increases the error of calculation aging related fault location.

A non-intrusive method of aging related insulation degradation in unshielded power cables is presented that utilizes our previously proposed surface wave method of cable diagnostics along with a suitable JTFDR waveform. The power spectra of the incident and reflected signals show the general bounds of such waveforms. We also mention the limitation of the proposed approach in terms of the surface wave being a TM type wave allowing dispersion. Assuming dispersion will cause the phase velocity to differ greatly only when the operating frequency band is multi-decade or so the proposed approach results in effective in determining aging related hot spots. These results are

significant for the future development of sensors that will be able to detect other soft defects due to water treeing, partial discharge etc.

CHAPTER 8

CONCLUSION AND FUTURE WORKS

The focus of this dissertation is on the applications of electromagnetic principles in the design and development of proximity wireless sensors. The contributions of this dissertation are summarized below. The trajectory for possible future research in this area is highlighted in Section 8.2.

8.1 CONTRIBUTIONS

The first major contribution of this dissertation falls under the low frequency (kHz) near-field static electric field sensing area. To this end, the fundamentals of interdigitated sensing are formulated and the design space is defined which clearly show the relationship between the electrode sizes and their spacing in determining the field penetration depth and the inter-electrode capacitance in the Material Under Test (MUT). It was shown that for large electrode width to separation ratios the results obtained from our analytical solutions approached the results from Finite Element Electromagnetic (EM) field solvers. The proposed analysis can be used for the quick analysis and design of proximity interdigitated sensors. Followed by the theoretical findings, the design, fabrication and experimental study of two types of sensors, e.g. a meander and a circular sensor are presented. The performances of the meander and the circular sensor were compared for embedded concrete moisture content measurement. The sensitivity of the meander sensor was 0.519 pF/percent change in moisture content while the sensitivity of

the circular sensor was 5.454 pF/ percent change in moisture content. The higher sensitivity for the latter was obtained because of its larger electrode width, spacing, and overall size. The proposed sensors deployed at different critical locations of concrete structures such as bridges and buildings could be significant for next generation autonomous civil infrastructure health monitoring systems.

The second major contribution of this dissertation is the investigation, design, and development of the concept of non-intrusive surface wave launch and propagation for cable or wiring fault detection. Multi-wavelength direct-contact transducers have been proposed for surface wave launch and propagation for communication and radar but not in sensing. Moreover, such large direct contact transducer operate in the RF/microwave frequency bands and are not suitable for cable or wiring health monitoring. In this work, sub wavelength dimension non-intrusive wave launchers are designed which can launch TDR or JTFDR type broadband surface wave waveforms in the VHF-UHF bands (100-300 MHz). The dependency of the transmission response versus frequency on launcher geometrical configuration and dimensions were studied experimentally. Greater than 3:1 transmission bandwidth (100-300 MHz) is obtained with cylindrical launcher on square orthogonal ground planes with CSW launchers this bandwidth reduces to slightly more than an octave (100-240 MHz), adequate for JTFDR applications. Open circuit faults were detected using surface waves and TDR on two cables (4.26 m and 9.45 m long XLPE cable- conductor diameter 14 mm, insulation thickness, 2 mm). The TDR pulse was created using an onboard pulse generating circuit that can be easily integrated with a sensor platform.

The third major contribution of this dissertation is the development of a new mathematical method that can be used to determine the changes in the dielectric constant of the insulating material of a cable from the measured responses from accelerated aging experiments. The phase transfer functions obtained from the FFT of measured magnitude and phase responses contain the value of the dielectric constant of the insulation material. By comparing the experimental JTFDR waveform signatures form a new and an aged cable of the same type, it is demonstrated that the change in the average dielectric constant of the insulation material can be estimated. The experimental data obtained for two types of cables, XLPE and EPR show that the dielectric constant decreases with accelerated aging (34.5% decrease for XLPE insulated cable and 10.4% decrease for EPR insulated cable for 120 years of real time operating age under a temperature of 50^0C).

The final contribution of this dissertation is the design, development and application of a JTFDR surface wave sensing method to determine the locations of aging related insulation damage detection in power cables. The comparative power spectral responses of conducted and non-intrusive surface wave JTFDR waveforms clearly show the resulting bandwidth reduction in the latter primarily because of the reflective nature of the coupling. Nonetheless, meaningful aging related damage detection can be achieved using surface wave JTFDR. It was demonstrated that with the help of a non-intrusive wave launcher and a 120 MHz Gaussian chirp waveform the location of aging related insulation damages can be detected. Experiments conducted based on the modified Arrhenius equation show the cross-correlation peaks at subsequent aging intervals as the cable was aged inside a heat chamber.

8.2 FUTURE WORKS

Starting from the electrostatic method of dielectric constant change measurement using conformal interdigitated proximity sensors we developed the non-intrusive surface wave based TDR and JTFDR method of cable diagnostics that utilizes waveforms launched in the VHF and UHF frequency range. The application of electromagnetic principles in sensing and diagnostics shows clear potentials for many future applications that are yet to be identified. Some potential future works are described below.

The key challenges of the proximity interdigitated sensing method are the following

- Limited surface area coverage – the sensor must be in the place where the moisture is being measured. Large area sensor arrays can be designed and their responses can be identified within a multiplexed system.
- Field penetration depth – for small electrode widths the field penetration depth is generally small and thus a smooth surface and direct contact is essential. The effect of the air-gap or surface unevenness need to be characterized in order to define the bounds.
- Sensor sensitivity – sensor sensitivity is largely dependent on sensor electrode width and overall sensor size. Application specific further research is needed to identify and design classes of sensors with the highest sensitivity.
- Geometrical limitation – not all materials prefer a planar sensor. For example, soil moisture sensing or the permittivity measurement of tissue may require small diameter cylindrical sensors.

The key challenges of the non-intrusive surface wave launch and propagation for cable or wiring fault detection are the following

- Operating frequency, bandwidth - Operating frequency and bandwidth are highly interdependent with fault type and fault resolution. From reflectometry concepts, a shorter duration waveform is preferable to detect defects of smaller size. However, shorter pulses carry lesser energy which does not propagate longer distance. Similarly, tradeoff between attenuation and spatial resolution is a challenge at higher center frequencies. Operating frequency and bandwidth also dictate the surface wave launcher size and design constraints. Furthermore, launcher size and design are also limited by the surface area available on the power cable. Fault specific future research should be done for the best performance.
- Environmental condition - The surface wave launcher with circuit and system performance may be subject to interruption by high voltage high power environment. Moreover, the performance of the sensing system may also change due to high humidity, weather, corrosive environment, continuous cable vibration due to wind and birds or other animal presence on the cable. Dust, dirt or ice accumulation at winter also may alter the system performance. Some of the sensors may gather wrong information for certain amount of time depending on the condition. New methods and models should be developed to compensate for these issues.
- System Reliability, Robustness- Power cable is one of the main components of a power distribution system. To build an efficient fault monitoring, diagnostic and

protection system novel online monitoring sensors should also be developed for transformers, motors, and circuit breakers. In many cases one fault causes cascading effects, leading to other failures and ending up with a catastrophic system failure. New methods and techniques need to be developed that can predict such events and strategies need to be developed so that they do not occur.

BIBLIOGRAPHY

[1] "Available: http://en.wikipedia.org/wiki/Strain_gauge. "

[2] "Available: http://en.wikipedia.org/wiki/Accelerometer."

[3] "Available: http://www.extech.com/instruments/categories.asp?catid=8."

[4] "Available: http://ds.informatik.rwth-aachen.de/teaching/ss06/labsn06."

[5] M. J. Whelan, M. V. Gangone, and K. D. Janoyan, "Highway bridge assessment using an adaptive real-time wireless sensor network," *IEEESensors Journal, ,* vol. 9, no. 11, pp. 1405-1413, 2009.

[6] Y. Wang, J. P. Lynch, and K. H. Law, "A wireless structural health monitoring system with multithreaded sensing devices: design and validation," *Structure and Infrastructure Engineering,* vol. 3, no. 2, pp. 103-120, 2007.

[7] J. T. Bernhard, K. Hietpas, E. George, D. Kuchma, and H. Reiss, "An interdisciplinary effort to develop a wireless embedded sensor system to monitor and assess the corrosion in the tendons of pre-stressed concrete girders," *Proceeding 2003 IEEE Topical Conference on Wireless Communication Technology, Honolulu, Hawaii, Oct. 2003, pp. 241-243.*

[8] X. Jin, and M. Ali, "Embedded antennas in dry and saturated concrete for application in wireless sensors," *Progress In Electromagnetics Research,* vol. 102, pp. 197-211, 2010.

[9] X. Jin, *Embedded Antennas in Concrete for Application in Wireless Sensors*, Ph.D. Dissertation, University of South Carolina, 2010.

[10] X. Jin, and M. Ali, "Reflection and Transmission Properties of Embedded Dipoles and PIFAs Inside Concrete at 915 MHz," *IEEE Antennas and Propagation Society International Symposium*, Charleston, SC, June 2009.

[11] K. M. Z. Shams, *Novel Embedded Antennas and Engineered Materials for Wireless Communications and Sensing*, Ph.D. Dissertation, University of South Carolina, Sept. 2007.

[12] K. M. Z. Shams, M. Ali, and A. M. Miah, "Characteristics of an Embedded Microstrip PatchAntenna for Wireless Infrastructure Health Monitoring,'' *IEEE Antennas and Propagation Society International Symposium Digest*, Albuquerque, NM, July 2006.

[13] M. Kaya, P. Sahay, and C. Wang, "Reproducibly Reversible Fiber Loop Ringdown Water Sensor Embedded in Concrete and grout for water monitoring," *Sensors and Actuators B: Chemical*, vol. 176, pp. 803-810, 2013.

[14] T. Hoshino, K. Kato, N. Hayakawa, and H. Okubo, "A Novel Technique for Detecting Electromagnetic Wave Caused by Partial Discharge in GIS,'' *IEEE Transactions on Power Delivery*, vol. 16, no. 4, pp. 1–7, Oct. 2001.

[15] M. N. Alam, R. H. Bhuiyan, R. Dougal, and M. Ali, "Novel Surface Wave Exciters for Power Line Fault Detection and Communications,'' *IEEE Antennas and Propagation Society International Symposium*, Spokane, WA, July 2011.

[16] M. Alam, R. Bhuiyan, R. Dougal and M. Ali, "Design and Application of Surface Wave Sensors for Non-Intrusive Power Line Fault Detection," *IEEE Sensors Journal*, vol. 13, no.1, pp. 339-347, Jan. 2013.

[17] B. A. Jones, "Modeling and detection of external signals from small apertures in wire shields," *IEEE Antennas and Propagation Society International Symposium,* Chicago, IL, 2012.

[18] G. Hashmi, M. Lehtonen, and M. Nordman, "Calibration of on-line partial discharge measuring system using Rogowski coil in covered-conductor overhead distribution networks," *IET Science, Measurement & Technology,* vol. 5, no. 1, pp. 5-13, 2011.

[19] G. M. Hashmi, *Partial discharge detection for condition monitoring of covered-conductor overhead distribution networks using Rogowski coil,* PhD dissertation, Helsinki University of Technology (TKK), Finland , 2008.

[20] M. Ali, R.H. Bhuiyan, R. Dougal, and M. N. Alam, *Non-Intrusive Cable Fault Detection and Methods,* US Patent Application Number: 20120133373, 2011.

[21] M. N. Alam**,** R. H. Bhuiyan, R. Dougal, and M. Ali, "In-Situ Surface Wave Launchers for Power Line Fault Detection,'' *IEEE Antennas and Propagation Society International Symposium*, Chicago, IL, July 2012.

[22] E. Nyfors, and P. Vainikainen, "*Industrial microwave sensors*," *The Artech House Microwave Library, 1989.*

[23] R. Pallas-Areny, J. G. Webster, and R. Areny, "*Sensors and signal conditioning*," Wiley New York, 2001.

[24] N. Bowler, M. R. Kessler, L. Li, P. R. Hondred, and T. Chen, *Electromagnetic Nondestructive Evaluation of Wire Insulation and Models of Insulation Material Properties*, NASA Technical Report, 2012. "Available: http://ntrs.nasa.gov/search.jsp?R=20120002028."

[25] T. Chen, and N. Bowler, "Analysis of a capacitive sensor for the evaluation of circular cylinders with a conductive core," *Measurement Science and Technology*, vol. 23, no. 4, pp. 045102, 2012.

[26] T. Chen, N. Bowler, and J. R. Bowler, "Analysis of arc-electrode capacitive sensors for characterization of dielectric cylindrical rods," *IEEE Transactions on Instrumentation and Measurement*, vol. 61, no. 1, pp. 233-240, 2012.

[27] A. Mohd Syaifudin, S. C. Mukhopadhyay, P.-L. Yu, M. J. Haji-Sheikh, C. H. Chuang, J. D. Vanderford, and Y. W. Huang, "Measurements and performance evaluation of novel interdigital sensors for different chemicals related to food poisoning," *IEEE Sensors Journal*, vol. 11, no. 11, pp. 2957-2965, 2011.

[28] A. V. Mamishev, "Interdigital dielectrometry sensor design and parameter estimation algorithms for non-destructive materials evaluation," Ph.D. dissertation, Department of Electrical Engineering & Computer Science, Massachusetts Institute of Technology, Cambridge, 1999.

[29] A. V. Mamishev, K. Sundara-Rajan, F. Yang *et al.*, "Interdigital Sensors and Transducers," *Proceedings of the IEEE*, vol. 92, no. 5, pp. 808-845, 2004.

[30] G. J. Paoletti, and A. Golubev, "Partial Discharge Theory and Technologies Related to Medium-Voltage Electrical Equipment," *IEEE Transactions on Industry Applications*, vol. 37, no. 1, pp. 90-103, 2001.

[31] D. Coats, M. N. Alam, Q. Deng, M. Ali, and Y. J. Shin, "Joint Time-Frequency Optimized Reference for Surface Wave Reflectometry-Based Insulation Health Assessment," in Information Science, Signal Processing and their Applications (ISSPA), 2012 11th International Conference on, 2012, pp. 1135-1140.

[32] W. Jingjiang, P. E. C. Stone, D. Coatsand Y. J. Shin, "Health Monitoring of Power Cable via Joint Time-Frequency Domain Reflectometry," *IEEE Transactions on Instrumentation and Measurement* , vol. 60, no. 3, pp. 1047-1053, 2011.

[33] H. Imagawa, K. Emoto, H. Murase, H.Koyama, R. Tsuge, S. Maruyama, and T. Sakakibara, "PD signal propagation characteristics in GIS and its location system by frequency components comparison," *IEEE Transactions on Power Delivery*, vol. 16, pp. 564–570, Oct. 2001.

[34] S. Potivejkul, P. Kerdonfag, S. Jamnian, and V. Kinnares, "Design of a low voltage cable fault detector," *IEEE Power Engineering Society Winter Meeting*, vol. 1, pp. 724 – 729, Jan. 2000

[35] A. Cavallini, G. C. Montanari, A. Contin, and F. Pulletti, "A new approach to the diagnosis of solid insulation systems based on PD signal inference," *IEEE Electrical Insulation Magazine*, vol. 19, issue 2, pp. 23-30, Mar.-Apr. 2003.

[36] J. Wang, P. C. Stone, Y. J. Shin, and R. Dougal, "Diagnostics and Prognostics of XLPE and EPR Cables via Joint Time-Frequency Domain Reflectometry," *IET Signal Processing, Special Issue on Time-Frequency Approach to Radar Detection, Imaging, and Classification*, Vol. 4, No. 4, pp. 395-405.

[37] A. Bargigia, W. Koltunowicz, and A. Pigini, “Detection of partial dischargein gas insulated substations,” *IEEE Transactions on Power Delivery*, vol.7, pp. 1239–1246, July 1992.

[38] T. Hoshino, K. Nojima, and M. Hanai, “Real-Time PD Identification in Diagnosis of GIS Using Symmetric and Asymmetric UHF Sensors,’’ *IEEE Transactions on Power Delivery*, vol. 19, no. 3, pp. 1072–1077, July. 2004.

[39] A. Sommerfeld, “Transmission of electrodynamic waves along a cylindrical conductor,” *Annalen der Physik und Chemie*, vol. 67, pp. 233–290, 1899.

[40] J. Zenneck, “On the propagation of plane electromagnetic waves along a planar conductor surface and its relationship to wireless telegraphy,” *Annalen der Physik*, series 4, vol. 23, pp. 848–866, 1907.

[41] G. Goubau, “Surface waves and their application to transmission lines,” *Journal of Applied Physics*, vol. 21, pp. 1119–1128, 1950.

[42] G. Elmore, “Introduction to the Propagating Wave on a Single Conductor,” *Corridor Systems Inc*, 2009. "Available: http://www.corridor.biz/FullArticle.pdf "

[43] S. Ramo, J. R. Whinnery, and T. Van Duzer, *Fields and waves in communication electronics*, Wiley, 2007

[44] R. H. Bhuiyan, *Comprehensive Examination Ph.D. dissertation*, Department of Electrical Engineering, University of South Carolina, 2011.

[45] C. Maierhofer, “Nondestructive evaluation of concrete infrastructure with ground penetrating radar,” *J. Mater. Civil Eng.*, vol. 15, no. 3, pp. 287–297, May/Jun. 2003.

[46] H. Xing, J. Li, R. Liu, E. Oshinski, and R. Rogers, "2.4GHz On-Board Parallel Plate Soil Moisture Sensor System," *Sensors Industry Conf.*., pp. 35-38, Houston, TX, Feb. 2005.

[47] S. C. Saxena and G. M. Tayal "Capacitive Moisture Meter," *IEEE Trans. Industrial Electron. Control Instru.*, vol. IECI-28, no. 1, pp. 37-39, Feb. 1981.

[48] J. B. Ong, Z. You, J. Mills-Beale, E. L. Tan, B. D. Pereles, and K. G. Ong "A Wireless, Passive Embedded Sensor for Real-Time Monitoring of Water Content," *IEEE Sensors Journal*, vol. 8, no. 12, pp. 2053-2058, Dec. 2008.

[49] R. H. Bhuiyan, R. A. Dougal, and M. Ali, "Proximity coupled interdigitated sensors to detect insulation damage in power system cables," *IEEE Sensors Journal*, vol. 7, no. 12, pp. 1589-1596, Dec. 2007.

[50] H.E. Endres and S. Drost, "Optimization of the geometry of gas-sensitive interdigital capacitors," *Sensors and Actuators B: Chemical*, vol. 4, pp. 95-98, May 1991.

[51] A. Leidl, R. Hartinger, M. Roth, and H.E. Endres, "A new SO_2 sensor system with SAW and IDC elements," *Sensors and Actuators B: Chemical*, vol. B34, no. 2, pp. 339–342, 1996.

[52] B. Jiang and A. Mamishev, "Robotic Monitoring of Power Systems," *IEEE Transactions on Power Delivery*, vol. 19, no. 3, July 2004.

[53] M. N. Soutsos, J. H. Bungey, S.G. Millard, M. R. Shaw, and A. Patterson, "Dielectric properties of concrete and their influence on radar testing," in *NDT &E International*, vol. 34, pp. 419-425, 2001.

[54] B. A. Auld, *Acoustic fields and waves in solids*, Wiley, New York, 1973.

[55] S. Diaz Valdes, and C. Soutis, “Health monitoring of composites using Lamb waves generated by piezoelectric devices,” *Plastics, Rubber and Composites*, vol. 29, no. 9, pp. 475-481, 2000.

[56] C. Furse, Y. Chung, R. Dangol *et al.*, “Frequency-domain reflectometry for on-board testing of aging aircraft wiring,” *IEEE Transactions on Electromagnetic Compatibility*, vol. 45, no. 2, pp. 306-315, 2003.

[57] S. Wu, C. Furse, and C. Lo, “Noncontact probes for wire Fault location with reflectometry,’’ *IEEE Sensors Journal*, vol. 6, no. 6, pp. 1716-1721, Dec. 2006.

[58] M. N. Alam, R. H. Bhuiyan, R. Dougal, M. Ali, “Surface Wave Propagation Measurements in Unshielded XLPE Power Cables,’’ *IEEE Antennas and Propagation Society International Symposium*, Orlando, FL, July 2013.

[59] Y. J. Shin, E. J. Powers, T. S. Choe, C. Y. Hong, E. S. Song, J. G. Yook, and J. B. Park, “Application of time-frequency domain reflectometry for detection and localization of a fault on a coaxial cable,” *IEEE Transactions on Instrumentation and Measurement*, vol. 54, no. 6, pp. 2493-2500, 2005.

[60] E. Song, Y. J. Shin, J. Wang, P. Crapse, T. Choe, J. Park, and J. Yook, “Multiple Faults Detection and Localization via Time-Frequency Domain Reflectometry in a Coaxial Cables,” *IEEE Transactions on Electromagnetic Compatibility*, Vol. 51, No. 1, pp. 131-138, February, 2009.

[61] A. Sommerfeld, "Uber die Ausbreitung der Wellen in der dratlosen Telegraphie (On the propagation of waves in the wireless telelegraphy)," *Annalen der Physik*, pp., 665–736, 1909.

[62] M. King, and J. Wiltse, "Surface-wave propagation on coated or uncoated metal wires at millimeter wavelengths," *IRE Transactions on Antennas and Propagation* , vol. 10, no. 3, pp. 246-254, 1962.

[63] G. Goubau, "Surface wave transmission line," *US patent* 2685068, July 1954.

[64] G. Goubau, "Single-conductor surface-wave transmission lines," *Proceedings of the IRE,* vol. 39, pp. 619-624, 1951.

[65] G. E. Elmore, "System and apparatus for transmitting a surface wave over a single conductor," *US patent* 7567154B2, July 2009.

[66] E. F. Steennis and F. H. Kreuger, "Water treeing in polyethylene cables," *IEEE Transactions on Electrical Insulation*, vol. 25, no. 5, pp. 989-1028, Oct. 1990.

[67] C. Goodwin, *Tan delta / dissipation factor as an effective tool in determining the insulation condition of power cables using the BAUR PHG VLF system*, ICC Educational Program Spring 2001

[68] A. A. Al-Arainy, A. A. Ahaideb, M I. Qureshi, and N.H. Malik, "Statistical Evaluation of Water Tree Lengths in XLPE Cables at Different Temperatures," *IEEE Transactions on Dielectrics and Electrical Insulation*, vol. 11, no. 6, pp. 995-1006, Dec. 2004.

[69] M. Shuvalov, M. Mavrin, V. Ovsienko, and A. Romashkin, "Analysis of Water Trees in Power Cable Polymeric Insulation," *Journal of Applied Polymer Science.*, vol. 88, pp. 1543–1549, 2003.

[70] http://usgovinfo.about.com/od/consumerawareness/a/poweroutcosts.htm.

[71] F. Roos and S. Lindahl, "Distribution system component failure ratesand repair times–an overview," Lund University report, 2004.

[72] William A. Thue, *Electrical Power Cable Engineering*, Second edition, Marcel Dekker,Inc., NY, 2003.

[73] M. Hartebrodt and K. Kabitzsch, "Fault detection in field buses with time domain reflectometry," in *7th AFRICON Conference in Africa*, vol. 1, pp. 391 – 396, Sep. 2004.

[74] J. G. Webster, *Wiley Encyclopedia of Electrical and Electronics Engineering*, Wiley-Interscience, 1999.

[75] P. Smith, C. Furse, and J. Gunther, "Analysis of Spread Spectrum Time Domain Reflectometry for Wire Fault Location," *IEEE Sensor Journal*, vol. 5, no. 6, pp. 1469- 1478, Dec. 2005.

[76] N. Ahmed and N. Srinivas, "On-line partial discharge detection in cables," *IEEE Transactions on Dielectrics and Electrical Insulation* , vol. 5, no. 2, pp. 181-188, Apr. 1998.

[77] R.H. Bhuiyan, R. Dougal, and M. Ali, "A Miniature Energy Harvesting Device for Wireless Sensors in Electric Power Systems,'' *IEEE Sensors Journal*, vol. 10, pp. 1249-1258, July 2010.

[78] A. Sommerfeld, "Propagation of waves in wireless telegraphy," *Annalen der Physik*, vol. 28, no. 3, pp. 665-736, 1909.

[79] R. Bhuiyan, *Proximity Coupled Non-Intrusive Wireless Sensors for Monitoring and Diagnostics*, Ph.D. Dissertation, University of South Carolina, 2010.

[80] Ansys HFSS- http://www.ansoft.com/products/hf/hfss/

[81] K. Fujimoto, *Mobile antenna systems handbook.* Artech House Publishers, 2001

[82] M. Ali, *Analyses of Self Resonant Bent Antennas*, Ph.D. Dissertation, University of Victoria, 1997.

[83] "Agilent time domain analysis using a network analyzer," *Application note*.

[84] D. M. Pozar, *Microwave engineering*: Wiley India Pvt. Ltd., 2007

[85] J. Williams, “Simple nanosecond-width pulse generator provides high performance,” EDN Magazine, Design Ideas, 2004.

[86] G. Mazzanti, “Analysis of the combined effects of load cycling, thermal transients, and electro thermal stress on life expectancy of high-voltage ac cables,” *IEEE Transactions on Power Delivery*, vol. 22, no. 4, pp. 2000–2009,Oct. 2007.

[87] R.J. Campbell, *Weather-Related Power Outages and Electric System Resiliency*. Washington D.C.. UNT Digital Library. http://digital.library.unt.edu/ark:/67531/metadc122249/. Accessed March 3, 2013.

[88] K. Anderson, D. Furey, and K. Omar, *Frayed Wires: U.S. Transmission System Shows Its Age*, Fitch Ratings, October 25, 2006. http://www.pjm.com/~/media/documents/reports/strategic-responses/ appendices/appendix12-fitch-transmission.ashx Accessed March 3, 2013.

[89] P. Tsai, L. Chet, C. C. You, and C. Furse, “Mixed-signal reflectometer for location of faults on aging wiring,” *IEEE Sensors Journal*, vol. 5, no. 6, pp. 1479–1482, Dec. 2005..

[90] S. B. Dalal and R. S. Gorur, “Aging of distribution cables in service and its simulation in the laboratory,” *IEEE Transactions on Dielectrics and Electrical Insulation*, vol. 12,no. 1, pp. 139–146, Feb. 2005.

[91] D. Rogovin, and R. Lofaro. *Evaluation of the Broadband Impedance Spectroscopy Prognostic/diagnostic Technique for Electric Cables Used in Nuclear Power Plants*. Division of Fuel, Engineering, and Radiological Research, Office of Nuclear Regulatory Research, US Nuclear Regulatory Commission, 2006.

[92] G. Mugala, *High Frequency Characteristics of Medium Voltage XLPE Power Cables*,PhD. Dissertation, KTH Royal Institue of Technology, Stockholm, Sweden, Nov. 2005.

[93] W.H. Kersting, *Distribution System Modeling and Analysis*, Third Edition, CRC Press, 2012.

[94] T. A. Short, *Electric power distribution equipment and systems*. CRC press, 2006.

[95] M. N. Alam, D. Coats, Y. J. Shin, and M. Ali, "A new method to estimate the average dielectric constants of aged power cables," *Journal of Electromagnetic Waves and Applications*, vol. 28, no. 7, pp. 777-789, 2014.